RF MEMS-Based Frequency Dependent Power Limiters

by

Desireh Shojaei-Asanjan

A thesis
presented to the University of Waterloo
in fulfillment of the
thesis requirement for the degree of
Doctor of Philosophy
in
Electrical and Computer Engineering

Waterloo, Ontario, Canada, 2018

Examining Committee Membership

The following served on the Examining Committee for this thesis. The decision of the Examining Committee is by majority vote.

External Examiner	Serge A. Charlebois Professor, Department of Information and Electrical Engineering, University of Sherbrooke
Supervisor(s)	Raafat R. Mansour Professor, Department of Electrical and Computer Engineering, University of Waterloo
Internal Member	Safieddin (Ali) Safavi-Naeini Professor, Department of Electrical and Computer Engineering, University of Waterloo
Internal Member	Slim Boumaiza Professor, Department of Electrical and Computer Engineering, University of Waterloo
Internal-external Member	Mustafa Yavuz Professor, Department of Mechanical and Mechatronics Engineering, University of Waterloo

AUTHOR'S DECLARATION

I hereby declare that I am the sole author of this thesis. This is a true copy of the thesis, including any required final revisions, as accepted by my examiners.

I understand that my thesis may be made electronically available to the public.

Abstract

Microwave power limiters are passive devices that are widely used to protect receivers from large interfering signals. Conventional radio frequency (RF) power limiters attenuate both desired and undesired signals in the entire frequency band. The need for frequency-dependent power limiters (FDPLs) arises in cases where the system dynamic range is frequency-dependent and the threshold level is dependent on the frequency band. RF micro-electro-mechanical systems (RF MEMS) switches self-actuate under high RF power and are well-known for their linearity and very low insertion loss. A FDPL can benefit from all the advantages of RF MEMS switches, particularly the linearity.

In this study, a novel approach to FDPLs is proposed. RF MEMS switches are integrated with bandpass filters to form a power limiter where the output RF power is limited to specific levels that can vary with the frequency band. Both non-planar and planar versions of FDPLs are presented using circulators and hybrids, and RF MEMS-based power limiters are analyzed theoretically and experimentally for one frequency band. The limiter attenuates the high power signal only within the bandwidth of the integrated filter. The design of the proposed power limiter is expanded to achieve power limiting for various frequency bands. The flatness of the threshold level can be set to the desired value by controlling the return loss of the filters used in the FDPL circuit. Measured results for an FDPL circuit are presented, demonstrating that the limiting power level can be controlled by adjusting the dc bias of the MEMS switches.

The commercially available electrostatically actuated switches OMRON and Radant are employed for the realization of the FDPL. Additionally, tunable FDPL circuits are fabricated and measured, demonstrating the feasibility of realizing adaptive frequency-dependent power limiters. In order to improve the controllability of the proposed MEMS-based FDPL circuits, both electrostatically-actuated and thermally-actuated switches are investigated theoretically and experimentally for use in power limiter applications. It is concluded that MEMS thermally-actuated switches provide better controllability of the self-actuation RF power level through adjustment of the bias voltage to the thermal actuator.

Additionally, a novel concept for realizing an RF power limiter for protecting superconductor digital receivers is proposed. A lumped-element niobium-based filter is used as a protection circuit. It consists of lumped-element resonators formed using spiral inductors and metal-insulator-metal capacitors integrated on a multilayer niobium process. The circuit operates as a bandpass filter at low power levels, allowing RF signals to pass, and as a reflector at high power levels. The lumped-element filter circuit is studied in detail to explain the performance of the filter at high power levels. It is concluded that some of the lumped-element inductors switch from being inductors when operating at low power levels to being capacitors when operating at high power levels. When the lumped-element inductors switch to capacitors, the filter circuit that consists of L-C resonators switches to a circuit that consists of capacitors, causing the input power to be reflected back. Both theoretical and experimental results are presented to verify this phenomenon. In addition to applications in power limiters, the concept can be employed to realize transmit/receive (T/R) switches in order to isolate the transmit circuit from the receive circuit.

Acknowledgements

First and foremost, I would like to thank my supervisor, Professor Raafat Mansour for his great guidance and kind support throughout my graduate studies. I learned so many life lessons other than technical and professional expertise from him.

My deepest gratitude goes to all the members of my family, for the wonderful support they all provided; specially my husband, Dr. Saleh Moonesan, my mother, Dr. Parisa Derakhshan Moghaddam, my father, Behrouz Shojaei-Asanjan, my brother, Khashayar Shojaei-Asanjan, my mother in law, Shamsi Mahve-Bidokhti, and my father in law, Mohammad-Taghi Moonesan and my sister and brother in laws Mahya and Ali for their endless love and support.

I like to thank my committee members, Professor Ali Safavi-Naieni and Professor Slim Boumaiza. I also like to thank Professor Mustafa Yavuz for accepting to replace Professor Martin in my committee.

My sincere thanks to my external examiner, Professor Serge Charlebois for reading my thesis and providing helpful feedback.

I would also like to thank all my friends in CIRFE laboratory at the University of Waterloo and all those who contributed to my learning experience. I like to specially thank Dr. Mostafa Azizi for all his help during my graduate studies years. I would also like to thank Dr. Sara Attar and Navjot Khaira for their support.

Finally, my thanks go to all my dear friends who have enriched my life, specially Limo, Payam, Sanam, Hadi, Nazli, Mina, Aidin, Bahar, Hossein, Rezvan and Ali who helped me overcome the difficult times and made this journey enjoyable.

Dedication

To my dear husband and parents

Table of Contents

List of Figures

List of Tables

List of Abbreviations

FDPL	Frequency Dependent Power limiter
MEMS	Micro Electro Mechanical System
HTS	High Temperature Superconductor
LTS	Low Temperature Superconductor
ADC	Analogue to Digital Converter
SME	Superconductor Micro Electronics
CPW	Coplanar Waveguide
SEM	Scanning Electron Microscope

1. Introduction

1.1 Motivations

Microwave power limiters are passive devices that are widely used to protect receivers from very large interfering signals. Limiters are usually placed before low noise amplifiers (LNAs), because they are sensitive to small signals and will be damaged if a large signal passes through them. Conventional radio frequency (RF) power limiters using diodes [1-4] attenuate both desired and undesired signals in the entire frequency band. The need for frequency-dependent power limiters (FDPLs) arises in cases where the system dynamic range is frequency-dependent and where the threshold level is dependent on the frequency band. Thus, as a 2-port network, the objective of the FDPL is to limit the RF power to specific threshold levels that are pre-set at various levels over the operating frequency band.

The performance of an ideal tunable 2-port FDPL network is depicted in Figure 1.1a. The output power is limited to specific levels based on the frequency bands. The aim is to realize the tunable FDPL experimentally with the characteristic input/output function shown in Figure 1.1b. Note that $\boldsymbol{\Delta}$ should be as small as possible in order to make the ripples (zig-zag levels) as close as possible to a flat line.

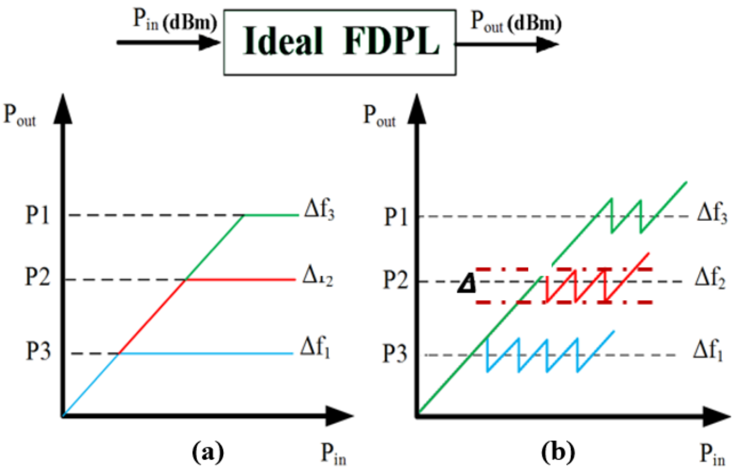

Figure 1.1. (a) Variation of the output power vs. the input power of an ideal tunable FDPL for different frequency bands; (b) the zig-zag performance of a tunable FDPL.

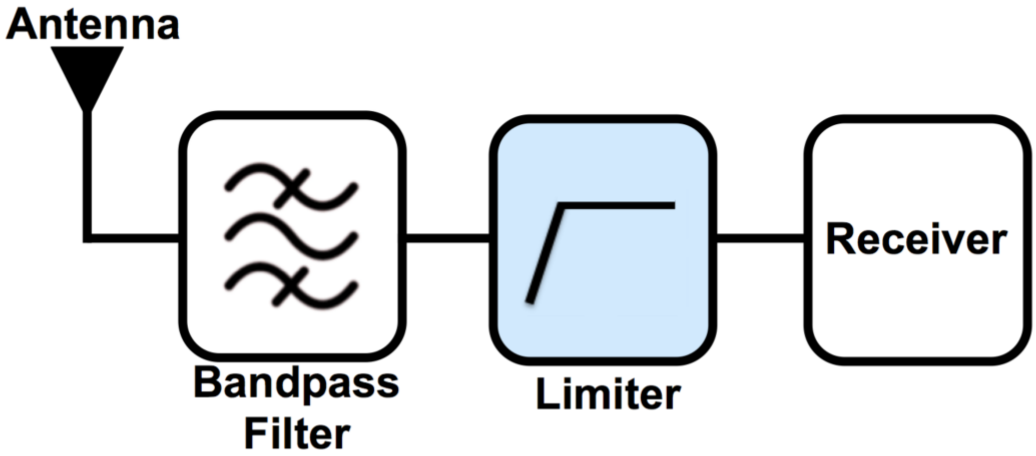

Figure 1.2. Limiter placement after bandpass filter and before digital receiver built using superconducting micro-electronics (SME) technology.

Low-temperature superconductor (LTS) digital RF receivers [1] allow direct digitization of wideband RF signals with very low dc power consumption [1, 2]. The superconductor analogue-to-digital converter (ADC) is comprised of junctions based on rapid single flux quantum (RSFQ) technology [3] that must be protected from high-power RF signals. The limiter circuit is not intended for protection against signals of extremely high power levels, as such protection circuits could be implemented at room temperatures outside the cryogenic package. Rather, the proposed circuit is intended to provide protection against power levels of a few dBm, as these can still damage RSFQ junctions. Another objective is to have the power protection circuit monolithically integrated with the receiver chip. Frequency Dependent Power Limiters (FDPLs) are placed before the superconductor micro-electronic (SME) receivers where the dynamic range of the receiver can change with frequency as well as the interfering signals as shown in Figure 1.2.

The existing realization methods of FDPLs include employing ferrite and making use of the nonlinear excitation of magnetic spin waves in magnetized ferrites such as YIG (yttrium-iron-garnet) [5]. Frequency-selective varactor-based power limiters using bandstop resonators are also reported, employing Schottky diodes with bandstop resonators. The measurement results of the prototype in [6] show a narrowband bandstop response with limiting values for threshold power levels.

We propose using RF micro-electro-mechanical systems (RF MEMS) switches to realize FDPLs. The MEMS switches can either be connected in series or in shunt and can be actuated using either electrostatic, magneto static, piezoelectric or thermal forces [7]. RF MEMS switches self-actuate under high RF power and are well known for linearity and very low insertion loss [7]. An FDPL can benefit from all the advantages of RF MEMS switches, particularly linearity. Commercially available MEMS switches are mostly electrostatic switches. While the concept of RF MEMS switch self-actuation is considered a disadvantage in the normal operation of a switch, it is employed in this design as an advantageous feature. When a high power RF signal is applied, the RF field may generate a large actuation force, causing the switch to self-actuate [7].

Niobium-based MEMS can be employed to realize the FDPLs for monolithic integration with the superconductor receiver. In order to verify the concept, room temperature RF MEMS is used. The ultimate goal for the room temperature RF-MEMS based FDPL is to have a FDPL circuit, which could be adjusted to work at different frequency bands and different power levels. Such type of MEMS-based FDPL circuits can be employed in a wide range of power limiter applications, whether at cryogenic or at room temperatures.

The power level at which switch self-actuation takes place depends on various parameters, such as the air gap between the cantilever beam and signal line (which can be controlled by the applied bias dc voltage) and the overlapping area between the cantilever beam and signal line. In this thesis, a novel approach to FDPLs is proposed. RF MEMS switches are integrated with bandpass filters to form a power limiter where the output RF power is limited to specific levels, based on the frequency bands. In order to improve FDPL device sensitivity, it is desirable to have a linear or nearly linear relationship between the self-actuation RF power and the switch dc-bias voltage. Thermally-actuated switches are good candidates, since they do not suffer from the cantilever collapse phenomenon (as do electrostatic switches) and can be suitable for limiter applications. We propose to study both electrostatically-actuated and thermally-actuated MEMS switches theoretically and experimentally to investigate their suitability for use in power limiter applications.

Another type of well-known power limiters are the high-temperature superconductor (HTS) transmission lines made of yttrium barium copper oxide (YBCO) film, where a transmission line

(TL) switches from a superconducting to a normal state [11], [12]. As power increase the RF current exceeds the critical current, the HTS YBCO microstrip line effectively becomes a line of insulator with characteristic impedance that is markedly different from the 50-Ohm impedance exhibited by the HTS microstrip line in the superconducting state. This, in turn, causes the majority of the signal to reflect back to the input of the HTS TL.

Such HTS power limiters offer superior performance compared to conventional power limiters, which use semiconductor diodes. However, the technologies (HTS and semiconductor) cannot be integrated monolithically with the low temperature superconductor (LTS) receiver chip. One may assume that the same HTS concept can be applied to LTS by simply using a narrow-width superconducting niobium (Nb) microstrip or coplanar transmission line. However, the LTS transmission line is made of niobium film that can still be considered normal metal at high power, not an insulator, as is the case with the HTS microstrip line. It is thus desirable to develop an LTS-based power limiter that can be monolithically integrated with LTS digital receivers.

1.2 Objectives

The overall objective of this research is to develop MEMS-based frequency-dependent power limiters at room and cryogenic temperatures. The main research tasks envisaged to achieve this objective include:

- Development and validation of the concept of MEMS-based power limiters.
- Development of fixed and tunable frequency-dependent power limiters.
- Investigation and characterization of the performance of both electrostatically-actuated and thermally-actuated MEMS switches for use in power limiter applications and studying the possibility of controllability improvement of FDPL circuit using thermally-actuated switches.
- Development of frequency-dependent power limiter at low-temperature superconductor circuits.

1.3 Thesis Outline

The motivation and objectives of this thesis study are described in Chapter 1. Chapter 2 discusses what is available in the literature and provides some background information about power limiters. Chapter 3 includes the MEMS-based frequency-dependent power limiter circuits at room temperature and tunable FDPL circuits, presenting theoretical and experimental results achieved. Chapter 4 presents the characterization of thermally-actuated switches for high power applications, while Chapter 5 introduces a novel low-temperature superconductor power limiter. Finally, Chapter 6 concludes the thesis by summarizing the results achieved, followed by some proposals for future research.

2. Literature Survey

Limiters are widely used in receivers before LNAs to protect them from high power. A limiter usually protects the receiver by introducing losses above a certain level of power within the operating range. In many applications, filtering is done at the front end to protect the receiver from unwanted high power signals. However, even after filtering, high power signals can still be present in the receive band and damage the receiver. A limiter circuit should provide low insertion loss to the desired band signals and very high loss to incident signals that exceed the damaging threshold. Furthermore, a limiter circuit should be very fast in order to be able to provide protection so fast and recover back to the normal state in a fraction of a second (usually in order of µs). Different types of limiter circuits are described in the literature.

2.1 Limiters and Frequency Dependent Power Limiters

In 1988, Seymour et al. [4] designed a monolithic GaAs PIN diode limiter at X- and Ka-bands. The limiter's circuit schematic is shown in Figure 2.1. In a 0 mA bias condition, low insertion loss is obtained. Different attenuation levels can be obtained by biasing the load and shunt PIN diodes. Since the diode impedance dependents on current, continuously variable attenuation can be achieved.

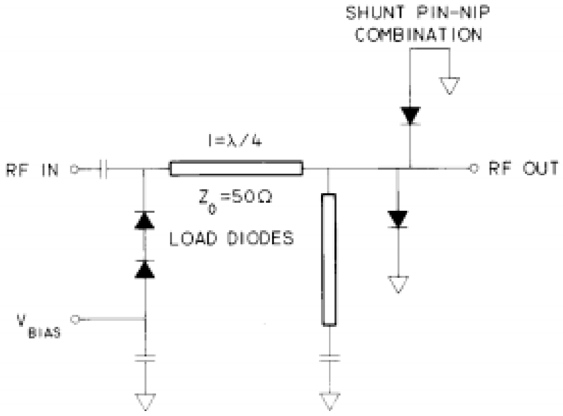

Figure 2.1. Monolithic pin diode variable attenuation limiter schematic [4].

The return loss (dB) and insertion loss (dB) results of a Ka-band attenuation limiter circuit at 0-mA bias and 20 mA bias are shown in Figure 2.2.

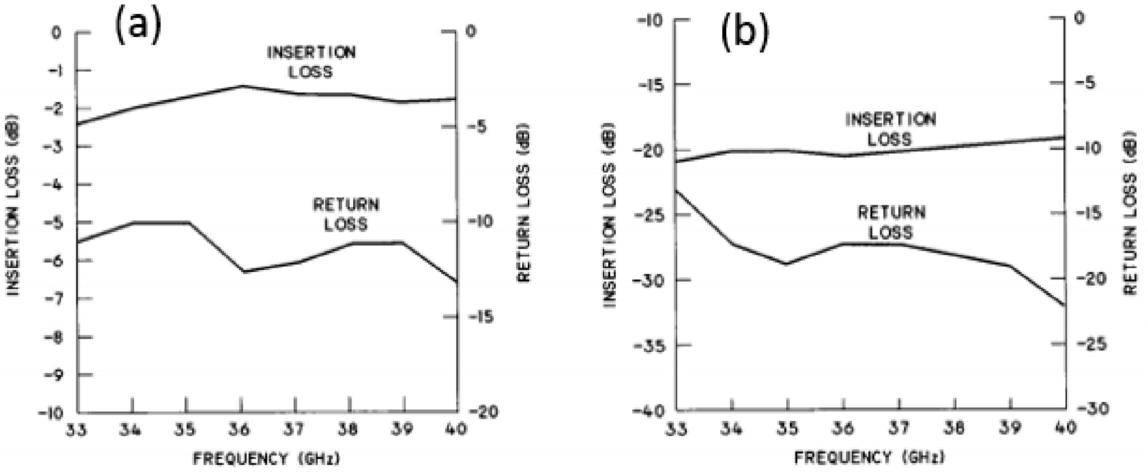

Figure 2.2. (a) Ka-band variable attenuation 0 bias performance; (b) 20 mA performance [4].

In [5], Smith et al. designed two-stage high-power limiters using GaAs diodes. The diode characteristics such as burnout and limiting were gathered for design. A set of burnout tests was done on diode structures. From this test, the amount of RF power that the diodes could handle before burnout was measured. These types of limiters attenuate all the signal amplitudes and do not differentiate between wanted and unwanted signals based on their frequencies. Figure 2.3 shows a schematic of a limiter with 8 PIN diodes, and Figure 2.4 shows a schematic of the limiter with 6 PIN diodes.

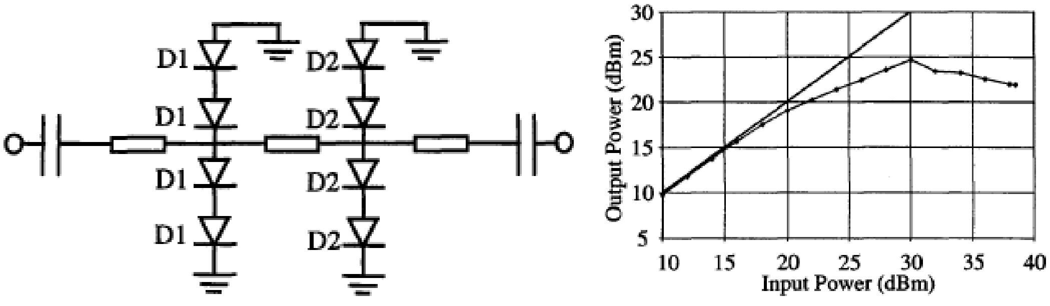

Figure 2.3. Schematic of a two-stage limiter with 8 PIN diodes (D1=D2=$33\ \mu m$) [5].

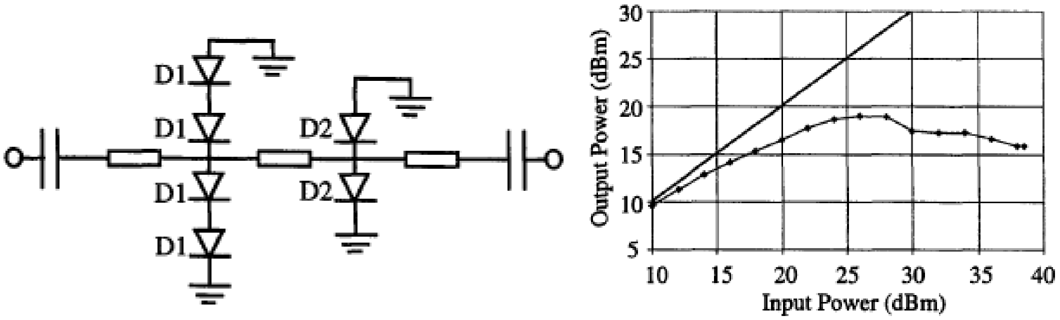

Figure 2.4. Schematic of a two-stage limiter using 6 PIN diodes (D1=D2=**33μm**) [5].

Another point to keep in mind is that the nonlinear characteristics of diodes might cause problems such as unwanted signal harmonics and intermodulation. In order to remove unwanted input signals, frequency tunable or switched notched filters were used by [13], [14]. The use of these filters restricts receiver performance and is challenging over temperature and time. Furthermore, the use of frequency selective limiters improves receiver sensitivity by limiting multiple signals at different frequencies independently. In these limiters, the large signal at a specific frequency will be compressed and the small amplitude signals at other frequencies will not be attenuated [10].

In [11] a 50 Ohm HTS superconductor-based transmission line is reversibly driven from low loss superconducting state to high loss normal state, resulting in a power limiter as shown in Figure 2.5.

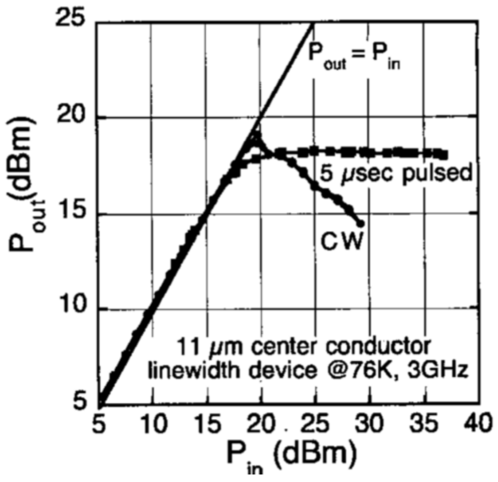

Figure 2.5. Limiting behavior for CW and 5μs pulse microwave signals at 3 GHz [11].

Continuous wave (CW) signals up to 10 W at 3 GHz and 100μs transient signals up to 100 W are used to demonstrate the reversible operation of this type of limiter [11]. Attenuation constant and characteristic impedance of these superconductor based CPW transmission line limiters are frequency dependent at normal (97 K) and superconducting (70 K) states as shown in Figure 2.6. These designs improve power consumption and provide higher incident power control and high reliability. The main problem with these designs is that, for them to work, cryogenic equipment is needed.

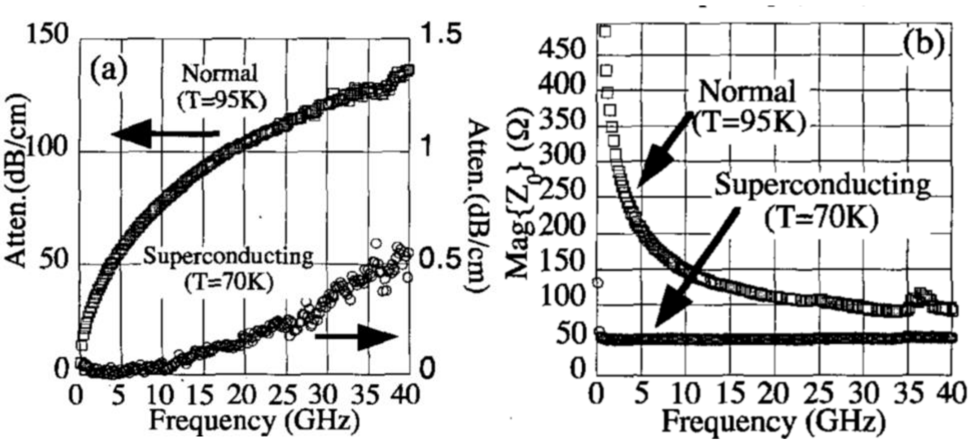

Figure 2.6. a) Attenuation constant b) Characteristic impedance [11].

The use of ferrite in frequency selective limiters was reported by several groups [12]. In these limiters, weak signals are not lost in the presence of strong signals but instead use nonlinear excitation of magnetic spin waves in magnetized ferrites such as YIG (Yttrium-Iron-Garnet). A stripline using Epitaxial YIG films can be seen in Figure 2.7.

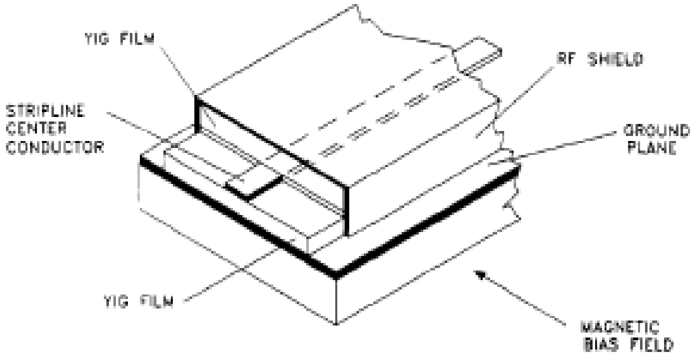

Figure 2.7. Stripline Ferrite signal line (FSL) using Epitaxial films [12].

The microwave signal coupled to a sample YIG at a low signal level produces linear and low loss response. However, above a critical RF magnetic field level, the nonlinearity becomes strong (magnetic dipoles in ferrite) and surpass natural losses. Energy then starts transferring to very short wavelengths. In [16], a uniform limiter using a GaScYIG film was achieved over 400 to 800 MHz with a threshold level of -25 dBm. Another technique that uses the gas discharge phenomena for designing limiters is presented in [16], but these limiters are not frequency selective and use other techniques to improve their transient response.

Padisan et al. [17, 18] proposed a frequency selective limiter design using bandstop resonators. The basic operation of a frequency selective limiter is illustrated in Figure 2.8.

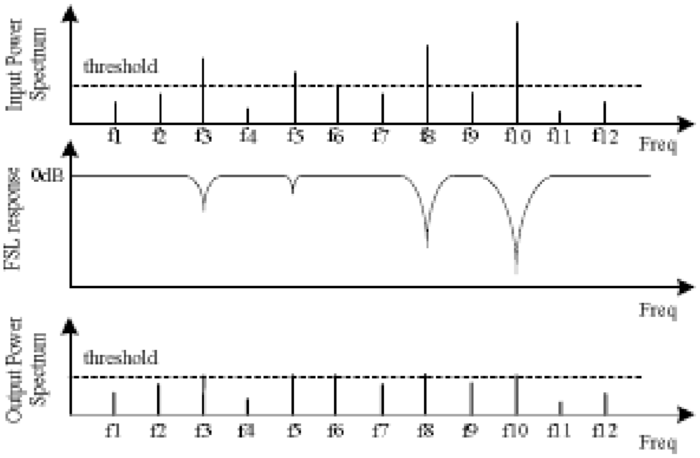

Figure 2.8. Operation of a frequency selective limiter [17].

Here, a prototype of a single resonator bandstop limiter was built and measured. The third order model of this limiter showed high performance in limiting. It is possible to cascade several of these limiters for wideband applications; since the return loss is equal to zero. The term ‘bandstop limiter’ was proposed because this new method of frequency selective limiting consists of a bandstop resonator loaded with a Schottky diode (Figure 2.9). The layout of the microstrip bandstop limiter is shown in Figure 2.10.

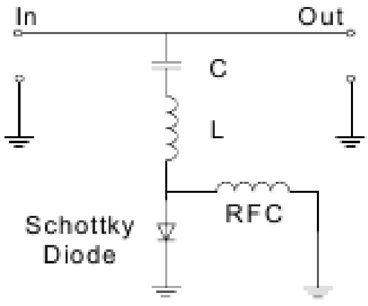

Figure 2.9. Lumped LC bandstop limiter [17].

Because the level of input power can control a diode's resistance, the response of the circuit can vary, depending on the input RF power level from all passes to bandstop.

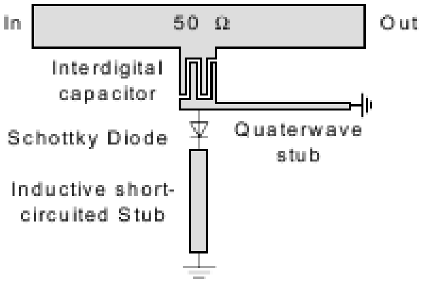

Figure 2.10. Microstrip bandstop limiter layout [17].

A diode's quality factor, which is relatively low in the highest possible situation, is the dominant feature in the total quality factor of the circuit. Hence, the total Q of the bandstop limiter will be low. The method presented [18] was used to improve the quality factor of the resonator. The new configuration of the limiter is shown in Figure 2.11.

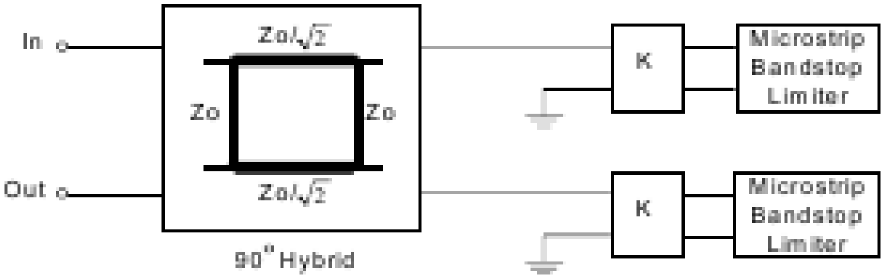

Figure 2.11. Enhanced Q_u of the limiter circuit [18].

A prototype of this limiter, along with the measurement results, is shown in Figure 2.12.

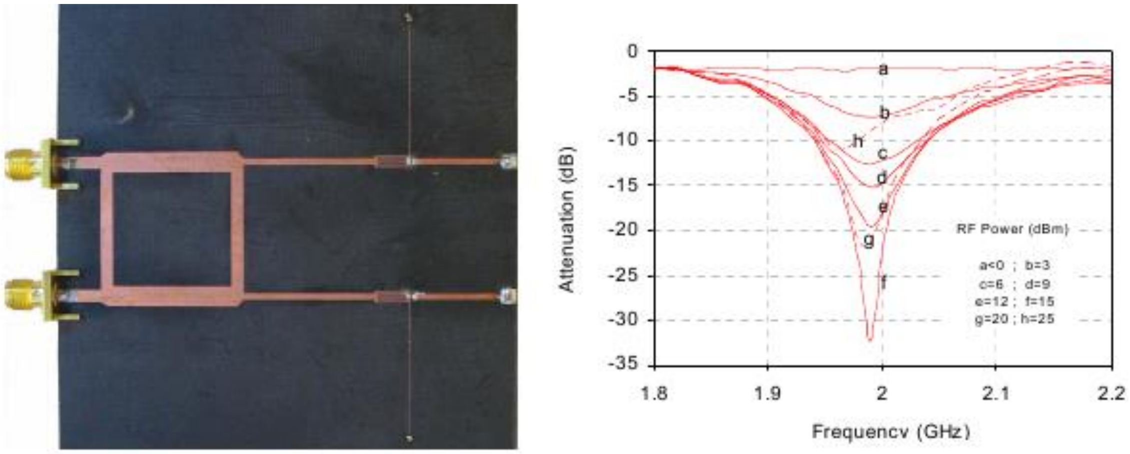

Figure 2.12. Fabricated limiter circuit and measurement results [18].

In [20], a high reliability and high repeatability power limiter was designed and fabricated using vanadium-dioxide (VO2) thin films in a coplanar waveguide (CPW) transmission line. VO2 is an interesting material that has a semiconductor-to-metal transition (SMT) phase. In this design, the CPW line was loaded with VO2 patterns to fill the gap between the signal line and ground lines of CPW. This switching device was thus a 'fuse' in a very broad frequency range (100 MHz to 40 GHz). An image of a CPW waveguide loaded with VO_2 patterns is shown in Figure 2.13.

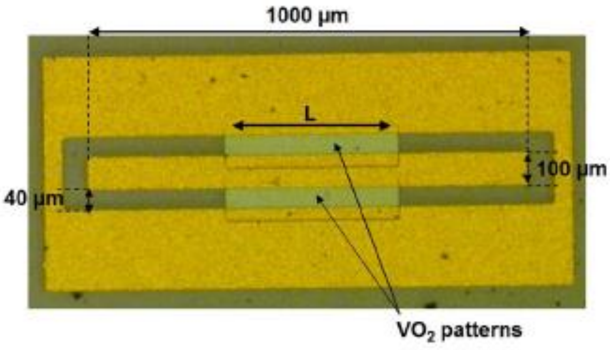

Figure 2.13. Image of a CPW waveguide loaded with $\mathbf{VO_2}$ patterns [20].

These CPW waveguides were used to design a two-divider-based power limiter. The measurements of transmitted power versus incident power at 10 GHz for this power limiter at different DC bias voltages at room temperature are shown in Figure 2.14.

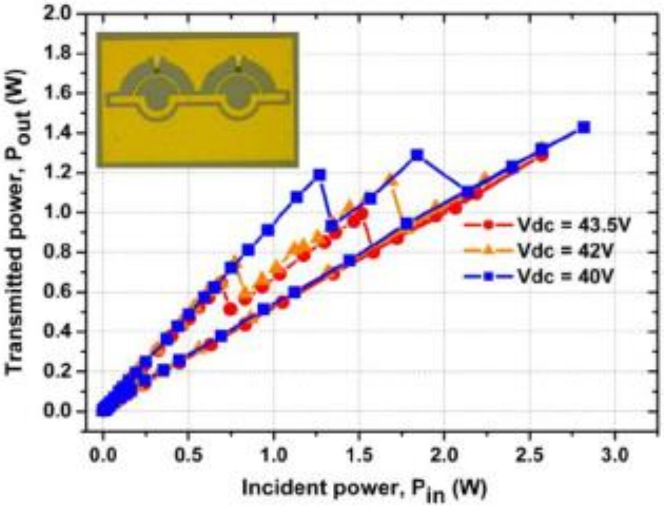

Figure 2.14. Measurement results of the two-divider-based power limiter at 10 GHz [20].

A frequency selective surface (FSS) with an integrated limiter for receiver protection was designed and fabricated in [21]. This surface acts normally until a certain power level is reached, at which point a dramatic resistance change across the element is made that causes the insertion loss to change from 0.2 dB to 20 dB. Vanadium dioxide films were deposited and characterized using a four-point probe method. It is important to mention that this action is passive and automatically reversible. Tuning concepts for limiting frequency selective surfaces have been presented for THz frequencies [22].

RF-MEMS switches were used in power limiters circuits instead of PIN/Schottky diodes due to their better performance. Using shunt switches, RF-MEMS based limiters were designed using the self-actuation phenomena in MEMS switches [23], [24]. In [25], by doing a complete analytical computation of the self-actuation of shunt RF-MEMS switches, a 10.24 GHz RF-MEMS-based power limiter was designed and fabricated. An electrical model of a shunt switch is shown in Figure 2.15.

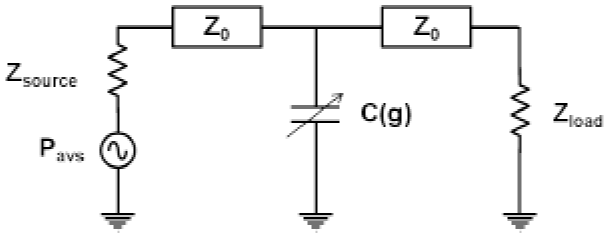

Figure 2.15. Electrical model of a capacitive shunt RF MEMS switch [25].

The pull-down and release powers of a shunt switch were calculated in [26], assuming the same RF and DC electrodes. These powers depend on the V_p pull-down voltage of the switch, the frequency (ω), the value of upstate capacitance (C_0) and the impedances at input/output.

A cross-section of the proposed MEMS-based limiter [25] (single capacitive switch) is shown in Figure 2.16.

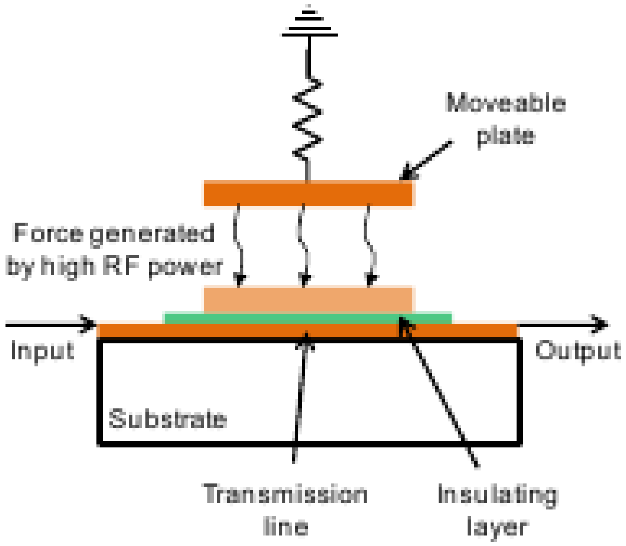

Figure 2.16. Cross-section of MEMS-based limiter considering self-actuation [25].

This model can be extended to more than one switch (array of switches), which will provide the zig-zag response of a power limiter. The number of attenuations depends on the number of switches used. An SEM picture of a single shunt switch and array of 4 shunt switches is shown in Figure 2.17. An electromechanical model for MEMS switches was presented in [27], which could be used to compute the switch properties.

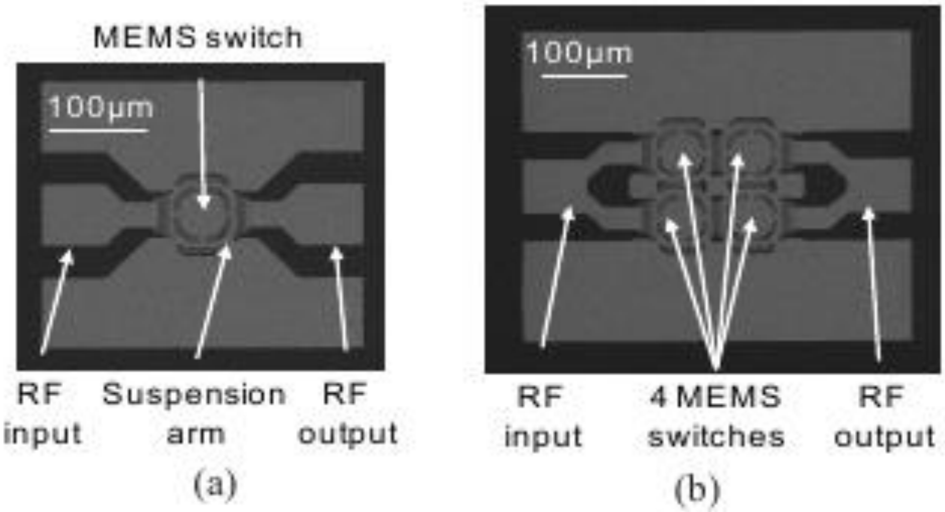

Figure 2.17. SEM pictures of (a) single switch and (b) array of four switches [24].

The limiter circuits, which used PIN/Schottky diodes, had nonlinearity problems and were also not frequency dependent in most cases [4-6]. A limiter circuit using diodes which was also frequency selective was proposed in the literature however the nonlinearity problem still existed [13]. The limiter circuits, which used ferrite, were frequency selective but were also nonlinear [12], [16]. The use of RF MEMS switches can solve the nonlinearity problem in limiter circuits. A Frequency dependent power limiter using capacitive MEMS switches was proposed by [25]. However, the controllability of the MEMS switches under high power is the main concern. A novel approach for MEMS-based FDPLs is presented in this thesis, which does not suffer from the linearity problems while, maintaining good controllability. This design is also extended to a tunable device, which can be used in different frequency bands.

3. MEMS-Based Frequency Dependent Power Limiter

Figure 3.1 shows a schematic of a power limiter that attenuates the input power within the passband of the filter, assuming that the return loss of the bandpass filter used in the circuit is $R(\text{dB})$ and the self-actuation RF power of the MEMS switch is $PA(\text{dbm})$. Initially, the switch is in the 'off' state, so the signal is reflected and P_{out} is almost equal to P_{in}, minus the loss of the circulator. As the input RF power, P_{in} , reaches $PA(\text{dBm})$, the MEMS switch changes to the 'on' state, and the signal passes through the filter and is absorbed by the load. The reflected signal from the filter is directed to the output, i.e., the output power is attenuated over the filter's bandwidth by the return loss of the filter $R(\text{dB})$.

The relationship between P_{in} and P_{out} in this circuit is shown in Figure 3.2a. The circuit given in Figure 3.1 acts as a frequency-dependent attenuator that is initiated by the input high power level. The level of attenuation is mainly determined by the return loss level of the filter. However, in this circuit, the output power level will keep increasing as the input power level increases.

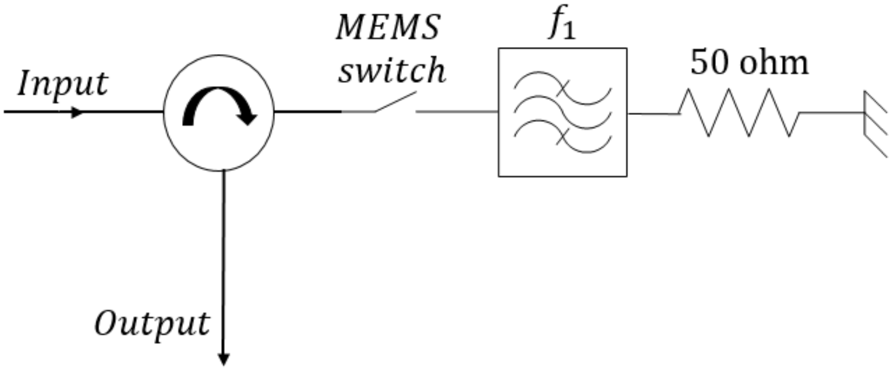

Figure 3.1. Schematic of a circuit that attenuates the output power at a specific frequency band initiated by the input high power.

In order to maintain a constant power level, i.e., to realize a zig-zag behavior around constant output power level, the circuit can be modified to have another identical branch (sub-branch), as shown in Figure 3.3. In this case, both switches are initially in the 'off' state, so the signal is reflected and P_{in} is equal to P_{out} (assuming that the circulators are lossless). As P_{in} reaches $PA(\text{dBm})$, the first MEMS switch changes to the 'on' state, and the signal is transmitted and absorbed by the load.

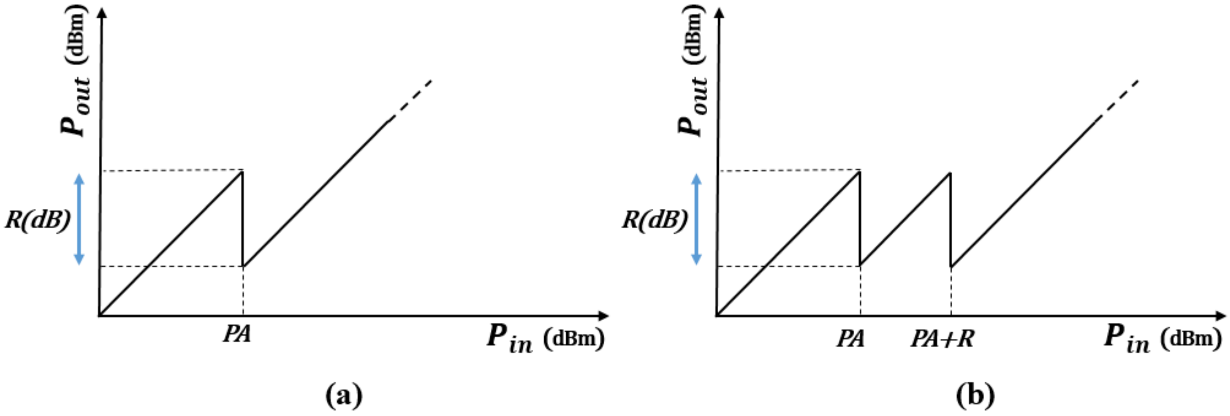

Figure 3.2. a) Performance of the circuit shown in Figure 3.1; b) performance of the circuit shown in Figure 3.3.

The reflected signal from the filter within the pass-band is reflected back with $R(\text{dB})$ attenuation. To turn the second switch to the 'on' state, P_{in} should reach $PA + R$ (dBm), since the signal is attenuated by $R(\text{dB})$. As P_{in} reaches $PA + R$ (dBm), both switches will be in the 'on' state and P_{out} is limited again, leading to the zig-zag performance shown in Figure 3.2b. It should be noted that the zig-zag level is controlled basically by controlling the return loss of the filters. The insertion loss of the filter does not play any role in the functionality of the power limiter, so the limiter performance is affected only by the filter bandwidth and its return loss.

Note that the circuit presented in Figure 3.3 can realize 2 zig-zags; to add an additional zig-zag, another branch should be added to the circuit, as shown in Figure 3.4.

In order to make the limiter frequency-dependent over various bands, more branches should be added to the proposed circuits, including filters in different frequency bands. In this case, the circuit shown in Figure 3.3 can be extended to the circuit shown in Figure 3.5. The limiting power level at each frequency band can be adjusted by controlling the dc bias voltages to the MEMS switches in the associated branch to yield the performance given in Figure 1.1b. It can also be adjusted simply by using different switches in each branch that exhibits different self-actuation power levels.

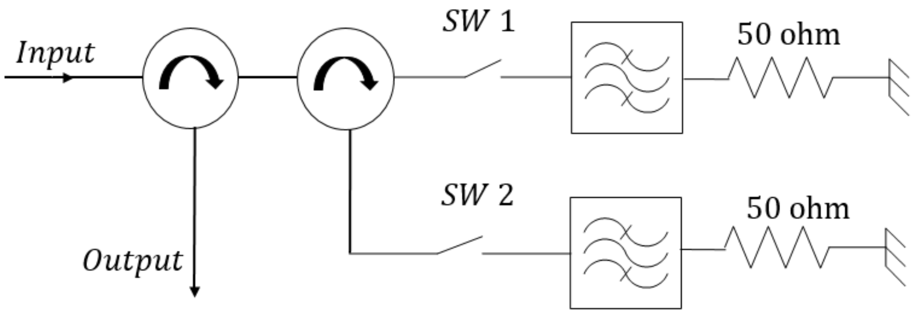

Figure 3.3. Schematic of a circuit that attenuates the output power at a specific frequency band initiated by the input high power.

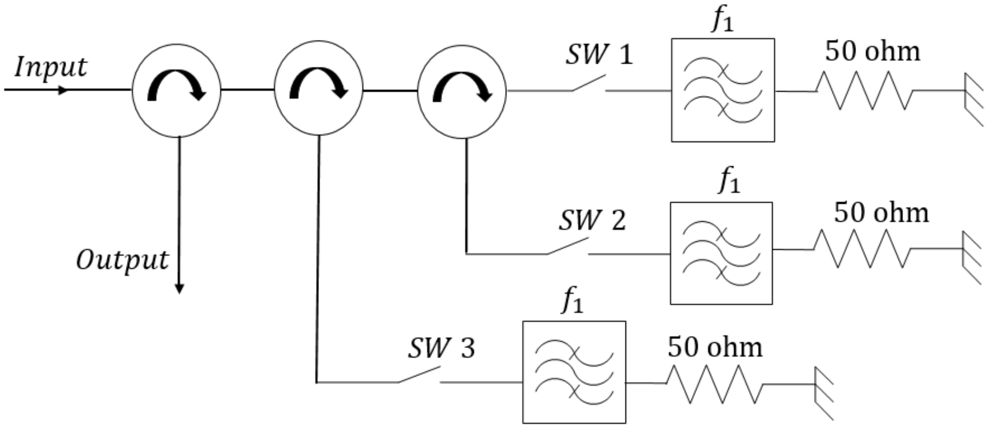

Figure 3.4. Power limiter circuit with three branches.

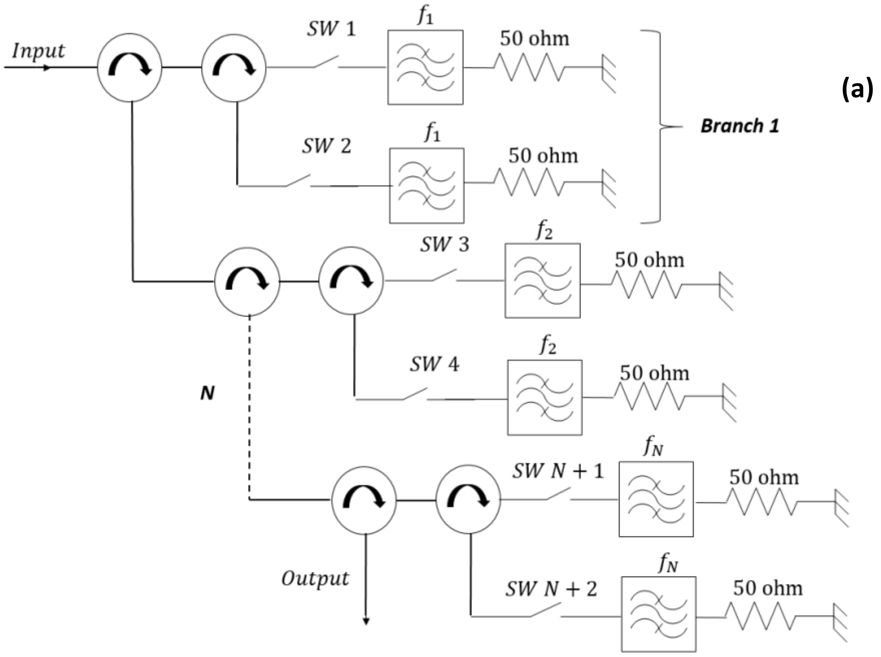

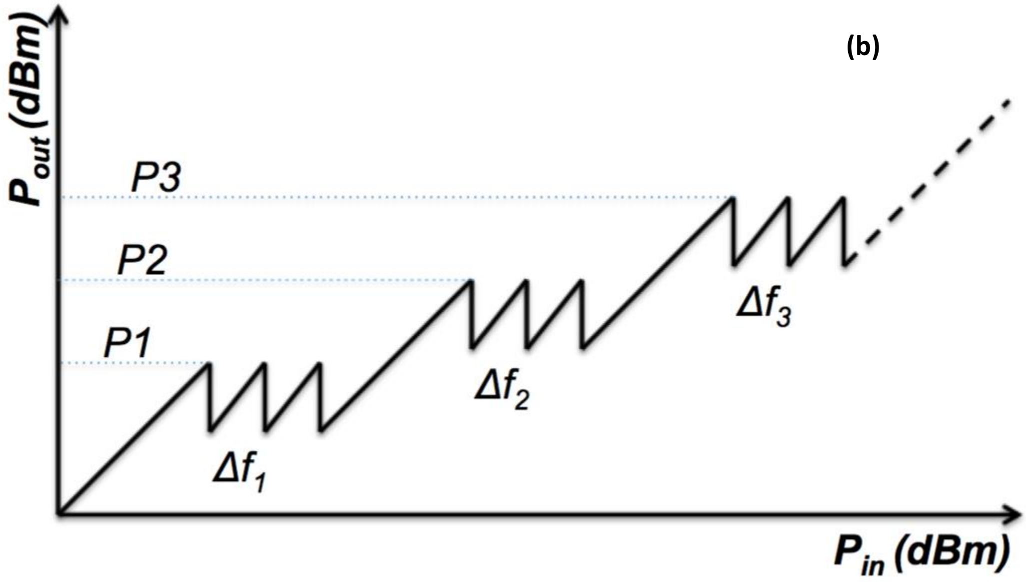

Figure 3.5. a) Schematic of the FDPL circuit using multiple branches; b) Response of the circuit shown in (a).

For a limited number of sub-branches, the output power level will still increase beyond the zig-zag level with the increase of input RF power. However, in most practical applications, the power limiter is rated to operate for a maximum power level. Thus, the number of the sub-branches can be adjusted accordingly. The configuration given in Figure 3.5 provides flexibility in tailoring the limiter performance by adjusting the dc bias for the MEMS switches.

In order to make the FDPL circuit entirely planar, the circulator can be replaced with a $90°$ Hybrid that covers the filter's frequency band, as shown in Figure 3.6. Initially, at a low level of input RF power, both switches are in the 'off' state. Hence, the signal is reflected and P_{out} is almost equal to P_{in} minus the loss of the hybrid. Let us now assume that the return loss of the bandpass filter used in the circuit is $R(\text{dB})$ and the self-actuation RF power of the MEMS switches is $PA(\text{dBm})$. In such an instance, as the input RF power, P_{in}, reaches $2PA(\text{dBm})$, the MEMS switches change to the 'on' state and the signal passes through the filters and is absorbed by the loads. The reflected signal from the filters is directed to the output, i.e., the output power is attenuated over the filter bandwidth by the return loss of the filter $R(\text{dB})$.

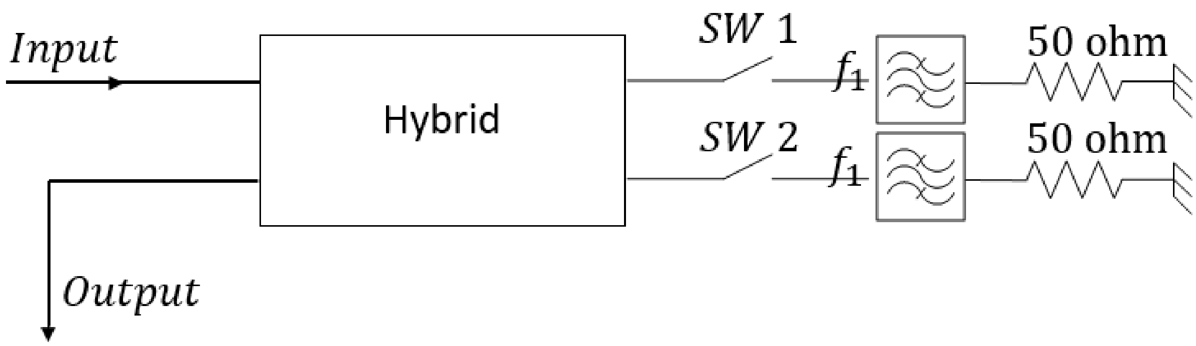

Figure 3.6. Schematic of a circuit that attenuates the output power at a specific frequency band initiated by the input high power. The circuit can be implemented in a planar configuration.

The relationship between P_{in} and P_{out} in this circuit is shown in Figure 3.7. As with the circulator version case, the insertion loss of the filter does not play any role in the functionality of the power limiter.

In order to maintain a constant power level, i.e. to realize a zig-zag behavior around constant output power level, the circuit can be modified to have another identical sub-branch, as shown in Figure 3.8a. In this case, the circuit will have the characteristic shown in Figure 3.9, which is similar to the response of the circuit shown in Figure 3.3. The only difference is that the input power level that initiates the attenuation is equal to twice the self-actuation power of the MEMS switch.

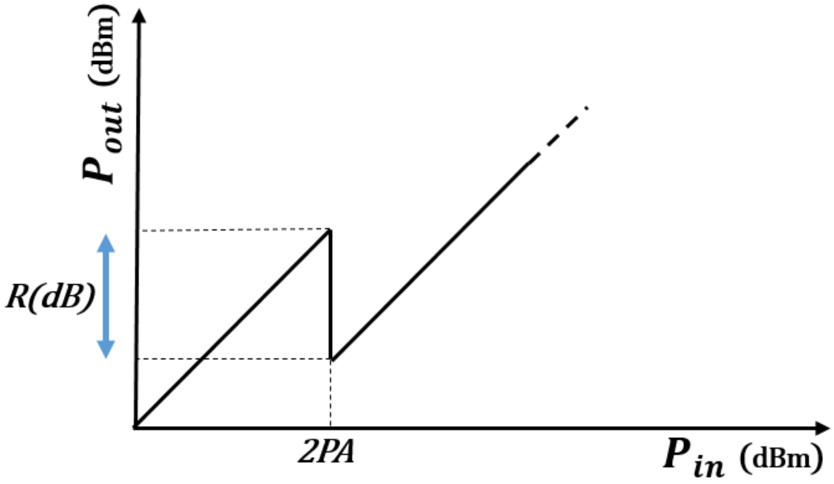

Figure 3.7. $P_{in} - P_{out}$ performance of the circuit shown in Figure 3.6.

Here, both switches are initially in the ‘off’ state, so the signal is reflected and P_{in} is equal to

P_{out} (assuming that the hybrid is lossless). As P_{in} reaches $2PA$(dBm), the first 2 MEMS switches (SW1 and SW2) change to the 'on' state, and the signal is transmitted and absorbed by the loads. The reflected signal from the filter within the pass-band is reflected back with R(dB) attenuation. To turn the third and fourth switches to the 'on' state, P_{in} should reach $2PA$+R (dBm), since the signal is attenuated by R(dB). When P_{in} is $2PA + R$ (dBm) , all switches are 'on' and P_{out} is again limited. It should be noted that the zig-zag level is controlled by controlling the return loss of the filters.

In order to make the limiter frequency-dependent over various bands, more branches should be added to the proposed circuit, including filters in different frequency bands. For this purpose, the circuit in Figure 3.8a can be extended to N branches employing filters of various bands. The output of the first branch is connected to the input of the second branch, and so on. The switches used in the circuit could be identical RF MEMS switches, but their dc bias voltage is varied to control the self-actuation RF power level in each branch. To add more flexibility in controlling the power level and the frequency band while minimizing the overall FDPL circuit size, tunable filters can be employed to replace the fixed filters. This will allow the FDPL to be fully dynamic to adapt to any interfering signals that may appear during system operation.

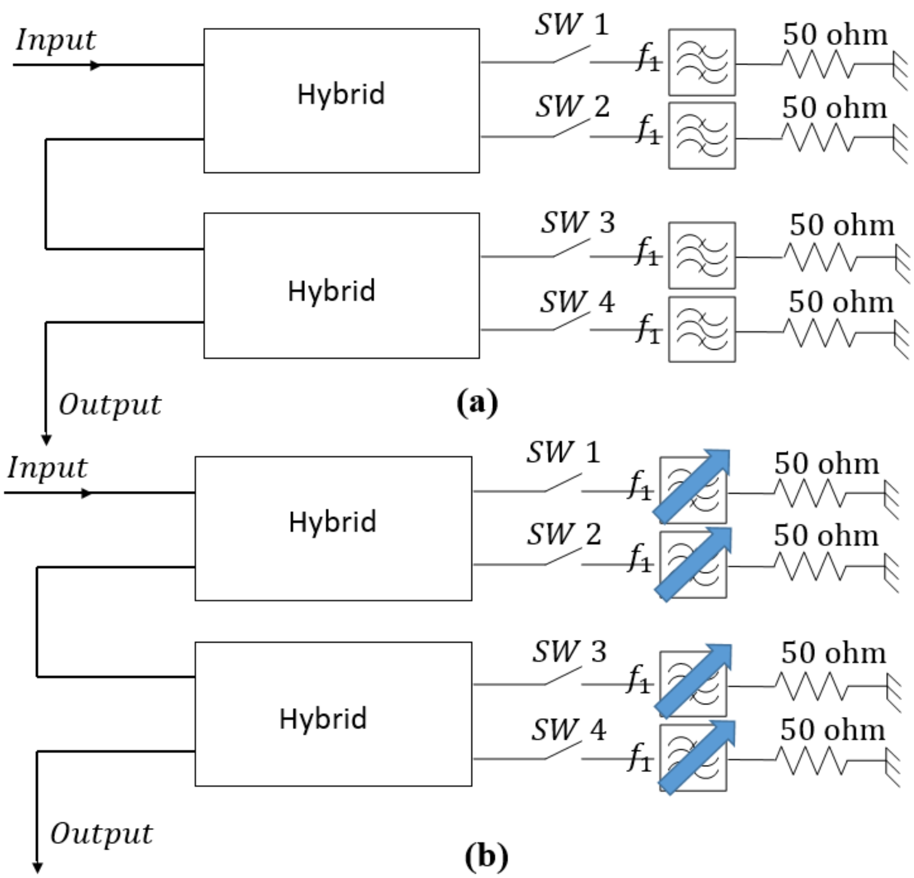

Figure 3.8. a) Power limiter circuit with two sub-branches; b) power limiter circuit with two sub-branches employing tunable filters.

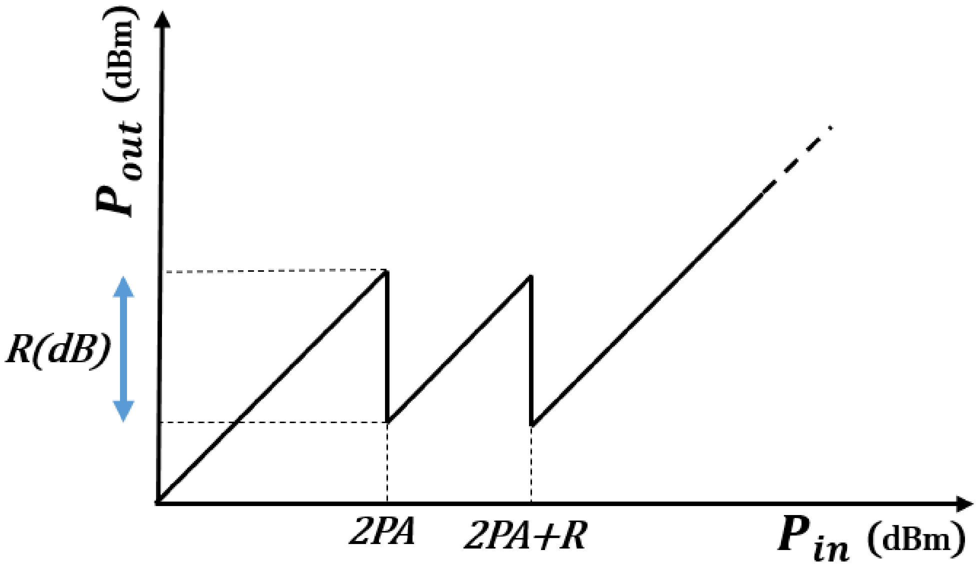

Figure 3.9. Performance of the circuit shown in Figure 3.8a.

3.1 Simulation results of the proposed FDPL circuit

In this section, we present simulation results of limiter circuits using circulators and hybrids. First, two branches of the limiter circuit shown in Figure 3.5 are simulated using four Chebyshev filters – two filters with a center frequency of 2.62 GHz, and two filters with a center frequency of 2.82 GHz for the other branch, all with 90 MHz bandwidth. The filters are intentionally designed with an 8 dB return loss.

A circuit similar to that of Figure 3.5, with two branches and two sub-branches for each branch, exhibits two zig-zigs at each frequency band. The four switches in this circuit (SW1, SW2, SW3 and SW4) are included in the simulation using the measured S-parameters of RMSW100 Radant switches in the 'off' and 'on' states. Simulations were done in five states. In State 1, all switches are off; in State 2, only SW1 is 'on'; in State 3, only SW1 and SW2 are 'on'; in State 4, only SW1, SW2 and SW3 are 'on'; and in State 5, all switches are 'on'. The simulation results obtained for the five states are shown in Figure 3.10a and Figure 3.10b.

It should be noted that the attenuation will not be exactly doubled, as the switch in the second branch is actuated from the interaction of the cascaded components. As mentioned in the previous section, the circulators can be replaced with hybrids in order to make the limiter circuit completely planar. The circuit shown in Figure 3.8a (one branch with two sub-branches) is simulated. The 90° Hybrid is designed using microstrip transmission lines and a Rogers 5880 substrate with 20 mils thickness. The same bandpass Chebyshev filter at 2.62 GHz with 90 MHz bandwidth is used for the limiter circuit, and the switches are represented with data items using S-parameters of measured Radant RMSW100 switch in the 'off' and 'on' states, exactly the same as the previous limiter circuit.

The circuit shown in Figure 3.8a (one branch with two sub-branches) is simulated. It has three possible states. At State 1 the power level is low and all the switches are 'off'; at State 2, the power level is increased until the first 2 switches, SW1 and SW2 of the first sub-branch, are 'on'; and at State 3, the power level is increased enough so that all four switches are 'on'. The S_{21} response of the circuit in all three states is shown in Figure 3.11.

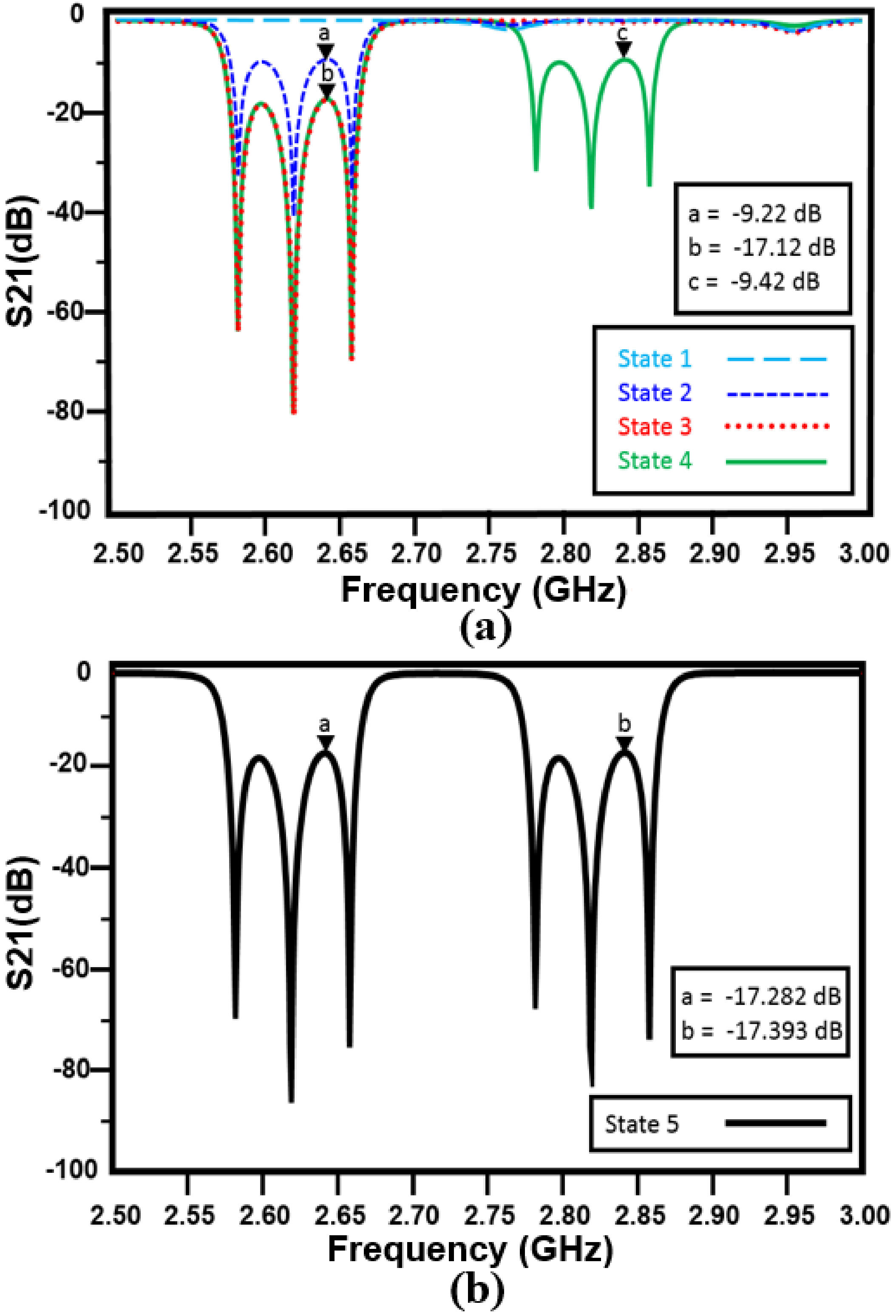

Figure 3.10 a) Performance of the circuit shown in Figure 3.5 assuming only two branches and S21 results of the first four states of the limiter circuit; b) S21 results of the fifth state of the limiter circuit.

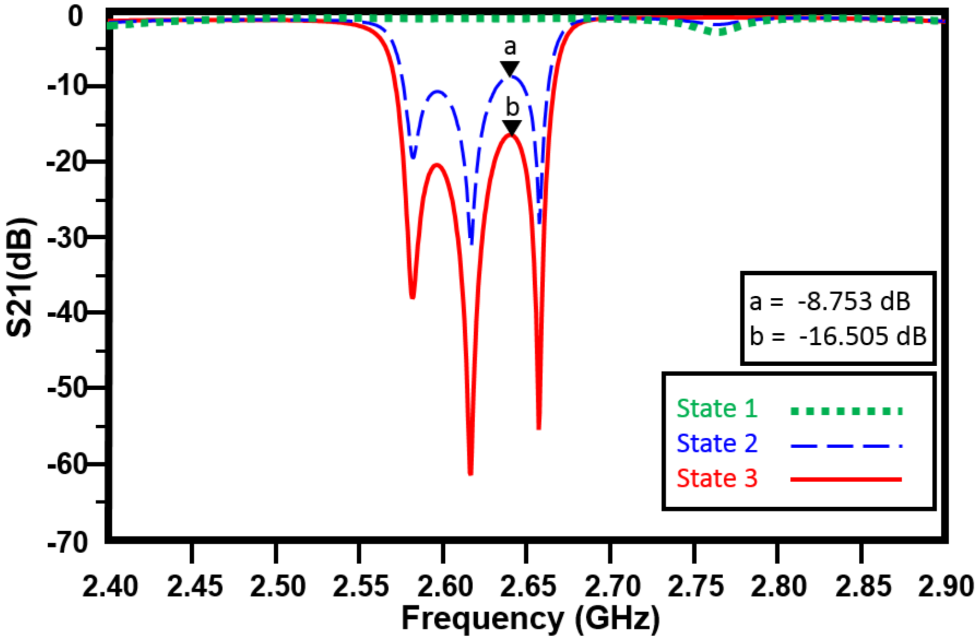

Figure 3.11. S_{21} results of all 3 states of the limiter shown in Figure 3.8a. (one branch with two sub-branches).

3.2 Relationship between self-actuation RF power and dc bias voltage for MEMS switches

High power testing was done on two commercial MEMS switches (the OMRON [28] switch and the Radant [29] RMSW101 switch) in order to find the relationship between the self-actuation RF power (P_{RF}) and the dc bias voltage(V_{dc}). Figure 3.12 shows the high power test set-up. The readings on the power meters are used to identify whether the switch is in the 'on' or 'off' state. The switches are assembled on 2-port PCB circuits, as shown in Figure 3.13, and are inserted as the device under test (DUT) shown in Figure 3.12.

First, the V_{dc} is set to a voltage lower than the actuation voltage and the RF power level is increased until the switch self-actuates. The bias voltage, V_{dc} , is then increased and the test is repeated to obtain a relationship between P_{RF} and V_{dc}. The results obtained for both the OMRON and Radant switches are shown in Figures 3.14 and 3.15, respectively.

The actuation voltage of the OMRON switch is 24.4 volts, while that of the Radant is around 76.1 volts. A power amplifier (PA) with a gain of 41dB is used in the test set-up. The insertion loss of the coupler/connectors and cables limits the maximum power that the DUT sees to 8 Watts, which explains why the high power testing results for the OMRON switch are shown up to this level.

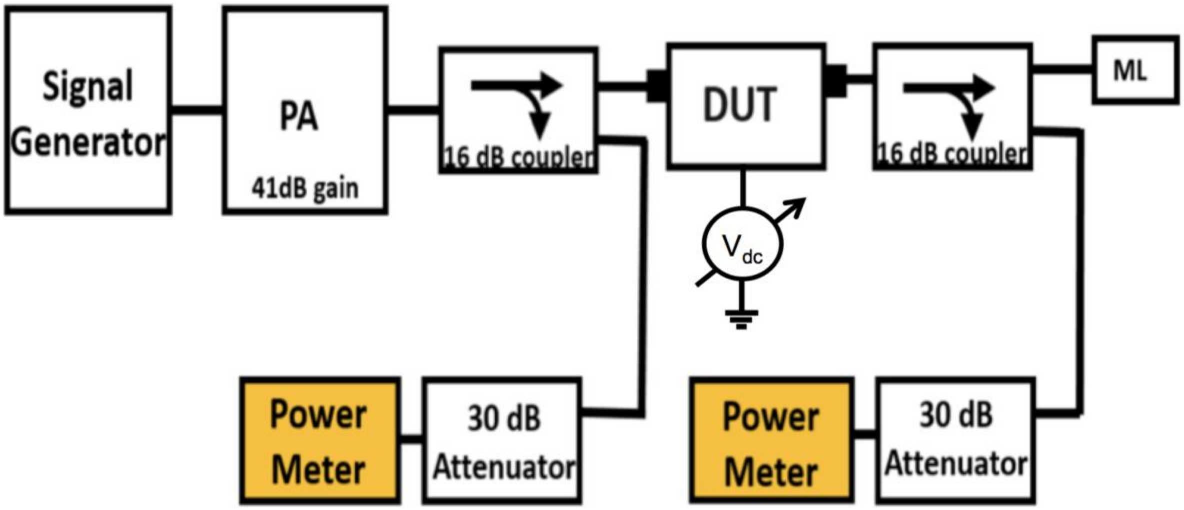

Figure 3.12. High power test set-up.

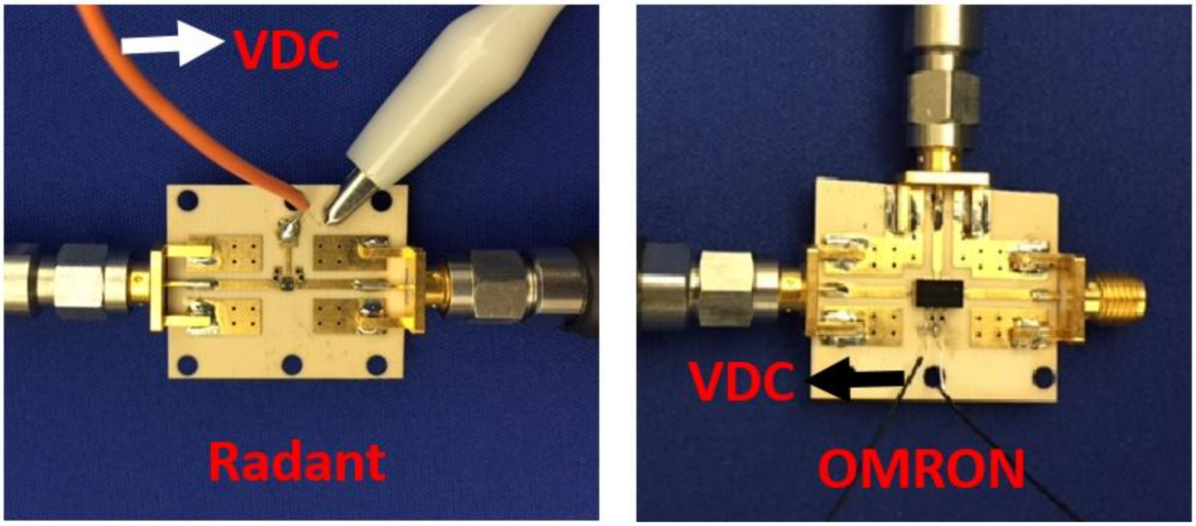

Figure 3.13. OMRON and Radant switches assembled.

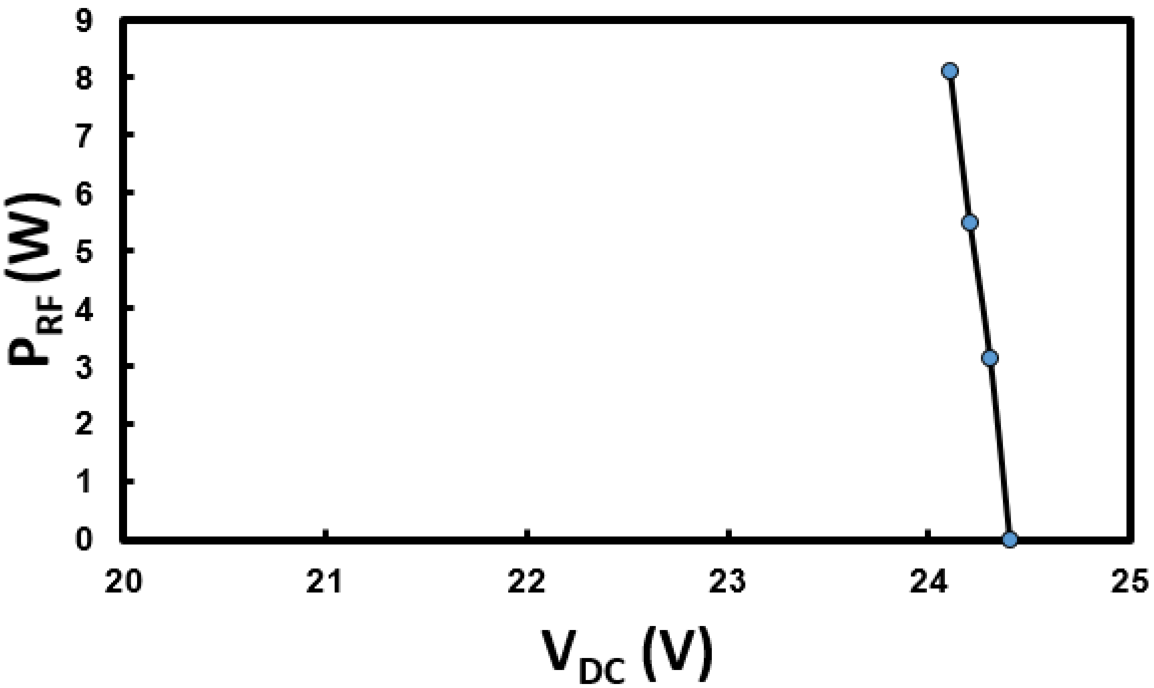

Figure 3.14. Measurement of $\boldsymbol{P_{RF} - V_{dc}}$ of the OMRON switch.

It can be seen that the largest variation of the self-actuation power level with the dc bias voltage takes place around the dc actuation voltage. This is attributed to the fact that as the dc bias voltage increases in electrostatic switches, the largest change in gap takes place around the dc actuation voltage.

The range of variation of the self-actuation power P_{RF} with V_{dc} can potentially be widened by using MEMS switches with thermal actuation [29]. The results shown in Figure 3.14 and 3.15 can be theoretically evaluated by using a Multiphysics analysis that combines CoventorWare mechanical analysis with HFSS high-power analysis. It would be possible to provide a theoretical analysis if the internal dimensions of these commercial switches were known.

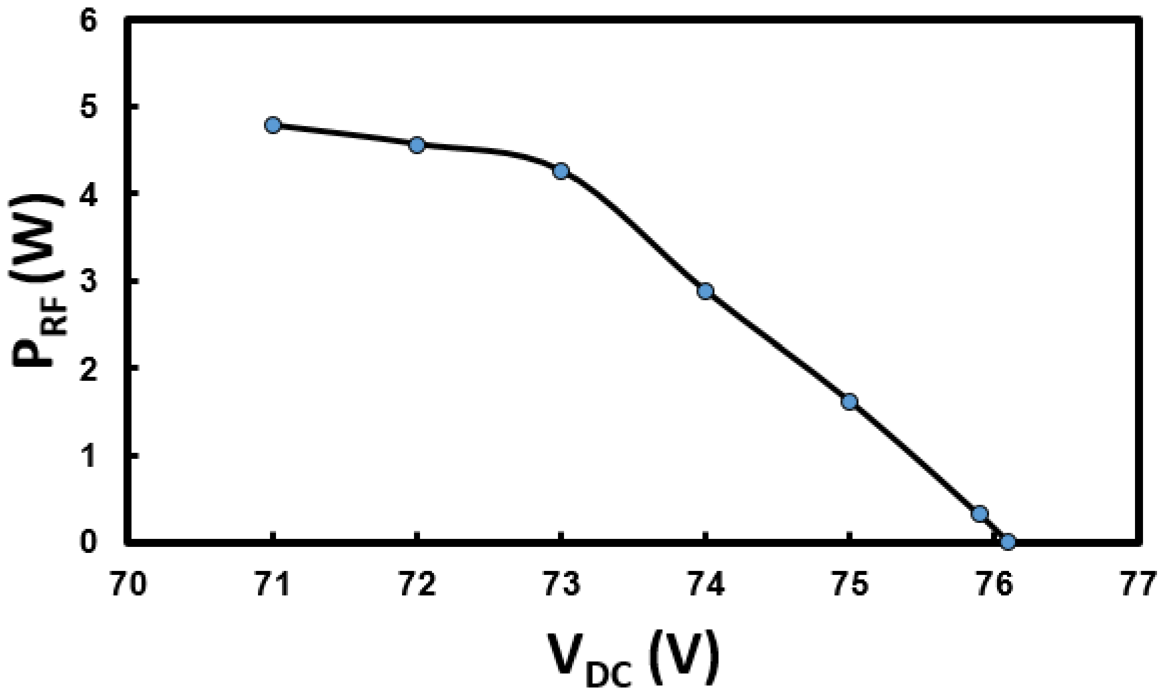

Figure 3.15. Measurement of $P_{RF} - V_{dc}$ of the Radant switch.

3.3 Measurement results of limiter circuits

The circuits of this section are fabricated on a Rogers5880 substrate with wire-bondable gold coated copper (1 oz.). A 3-pole microstrip filter is used in the circuits, which matches the required specifications for being used in the FDPL circuit. Figure 3.16 shows an FDPL circuit using a surface mount JCM2500t2700 JQL [31] circulator. The circulator has a minimum isolation of 20 dB and a maximum insertion loss of 0.35 dB between 2.614 GHz and 2.690 GHz. It can handle up to 60 Watts average power.

It is important to note that the filter is intentionally designed with a low return loss level in order to obtain a lower zig-zag level. RF measurement results of this circuit when the switch is in the ‘off’ and ‘on’ states are shown in Figure 3.17.

In order to see the zig-zag performance, the circuit can be fabricated using two sub-branches, as shown in Figure 3.18. The RF measurement results of the circuit when both switches are in the ‘off’ state, when one switch is in the ‘on’ state, and when both switches are in the ‘on’ state, are shown in Figure 3.19.

As mentioned in section II, in order to make this circuit entirely planar, the circulator can be replaced with a 90° Hybrid that covers the filter’s frequency band. The 90° Hybrid is designed at 2.6 GHz with 10% BW, and the RF MEMS switches used in these circuits are Radant RMS101 SPST types. The output ports of the bandpass filters (BPFs) are terminated by 50 ohm loads. The fabricated circuit is shown in Figure 3.20 The RF measurement results of the circuit when both switches are ‘off’ and when both switches are ‘on’ are given in Figure 3.21.

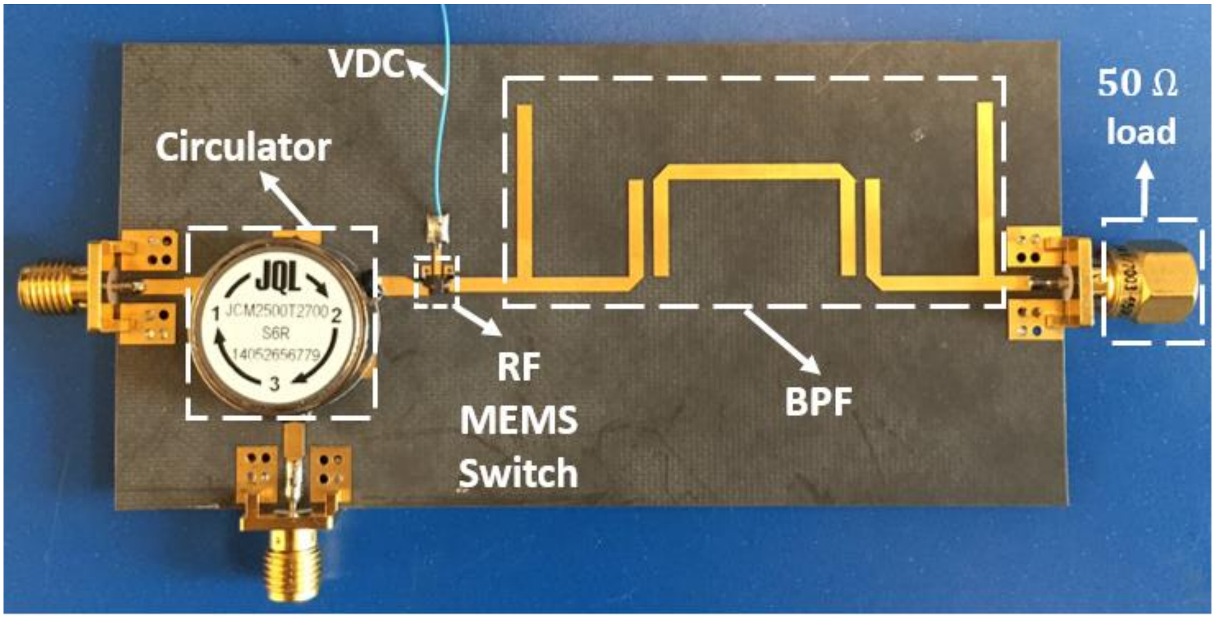

Figure 3.16. Fabricated FDPL using one circulator.

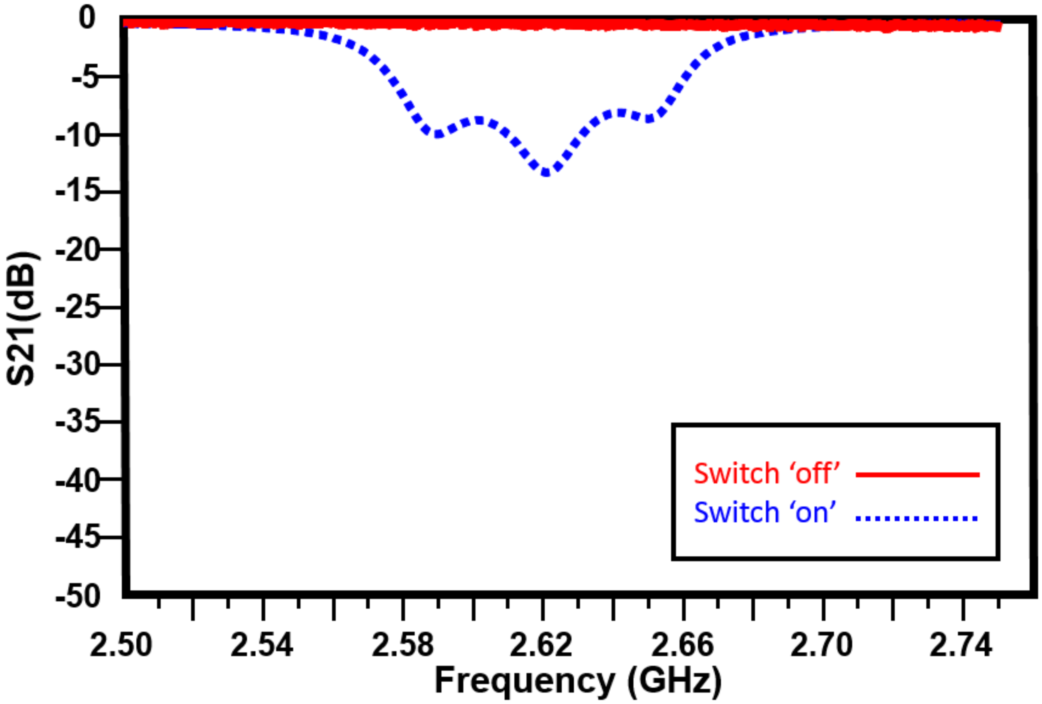

Figure 3.17. Measurement results of the circuit shown in in Figure 3.16.

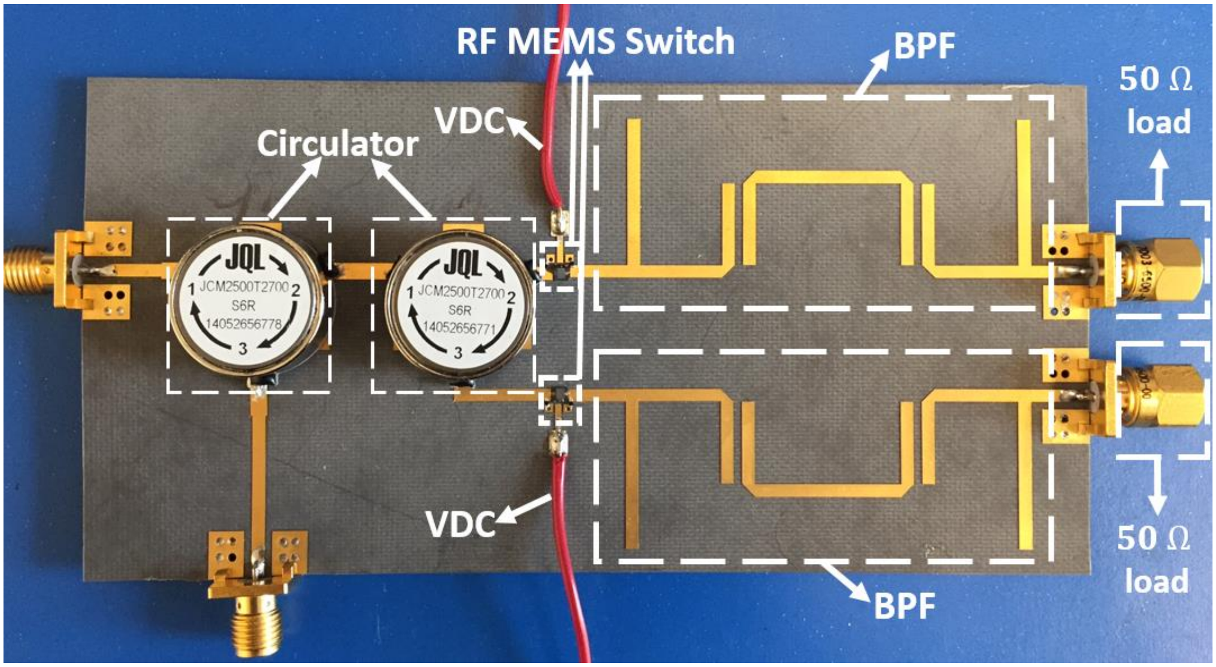

Figure 3.18. Fabricated FDPL using two circulators.

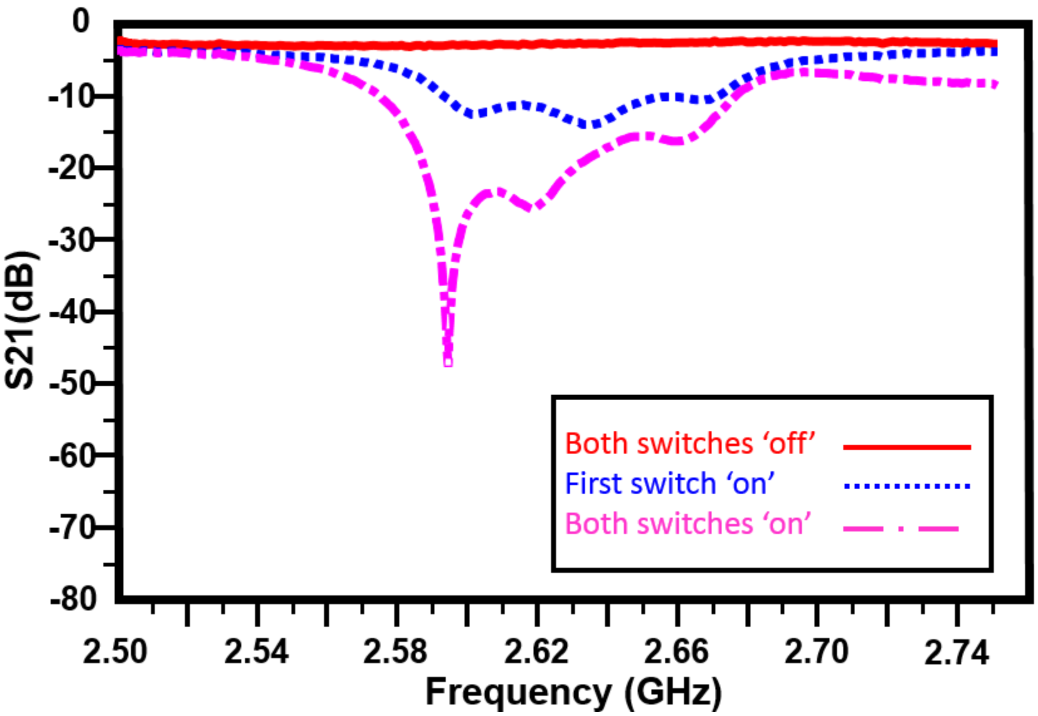

Figure 3.19. RF measurement results of the FDPL circuit including two circulators.

The high power test set-up used is similar to that shown in Figure 3.12 At low input RF power, the switches are in the 'off' state and P_{in} is equal to P_{out} . Then, as the input power increases, the switches change state from the 'off' state to the 'on' state, and attenuation increase to around 8dB. The set-up allows measuring output power versus input power of the limiter circuit (DUT) at one frequency at a time.

First, the RF power is set to -30dBm. With the use of a PA that has a 41dB gain, the input power to the limiter circuit is 11 dBm (~0.01 W), which is low enough not to actuate the MEMS switches. The Radant switch used in this circuit was from a different batch than the one used in the circuit shown in Figure 3.13. Specifically, the dc actuation voltage for this particular switch was 81 volts, not 76.1 volts.

In order to prove that it is possible to control the limiting power level, the dc bias voltage to the MEMS switch was reduced to 78 volts (i.e., below the dc actuation voltage) and the input power in the signal generator was increased gradually. With the amplification, the input power to the limiter was allowed to vary. As the input power level reached 12.58 Watts, a drop in the limiter output power by 8 dB was observed, as shown in Figure 3.22. Note that at an input power of 12.58 Watts, the RF MEMS switches see an input power of approximately 4 Watts due to the 3 dB power division of the hybrid and the 2 dB combined insertion loss of the hybrid and the coupler.

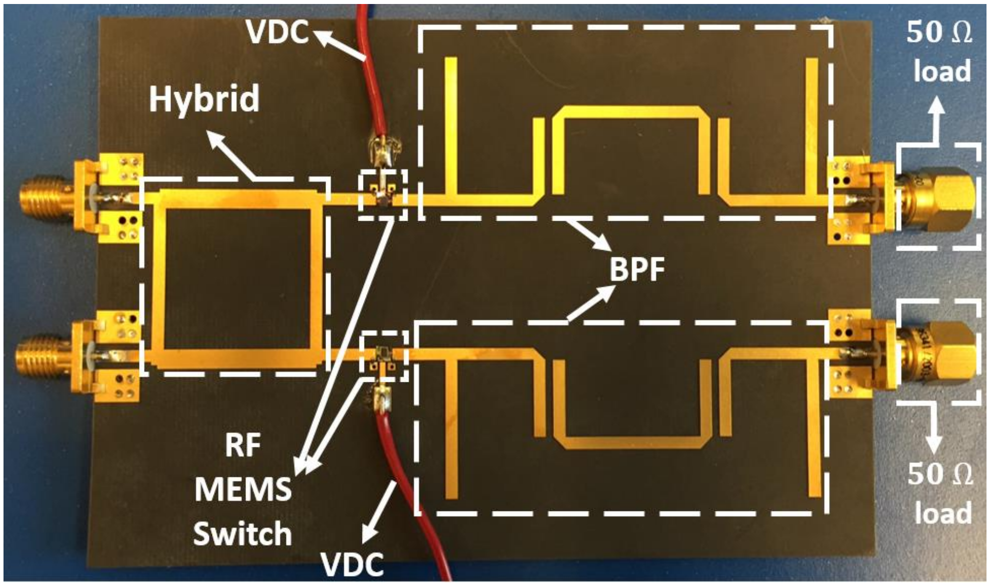

Figure 3.20. Fabricated limiter using a hybrid, 2 switches, and 2 filters.

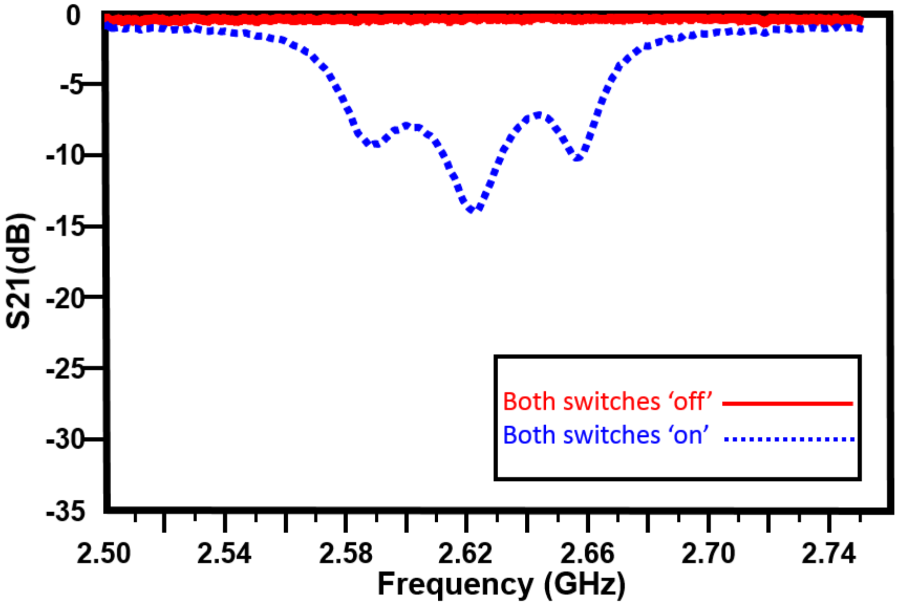

Figure 3.21. Measurement results of the FDPL in Figure 3.20.

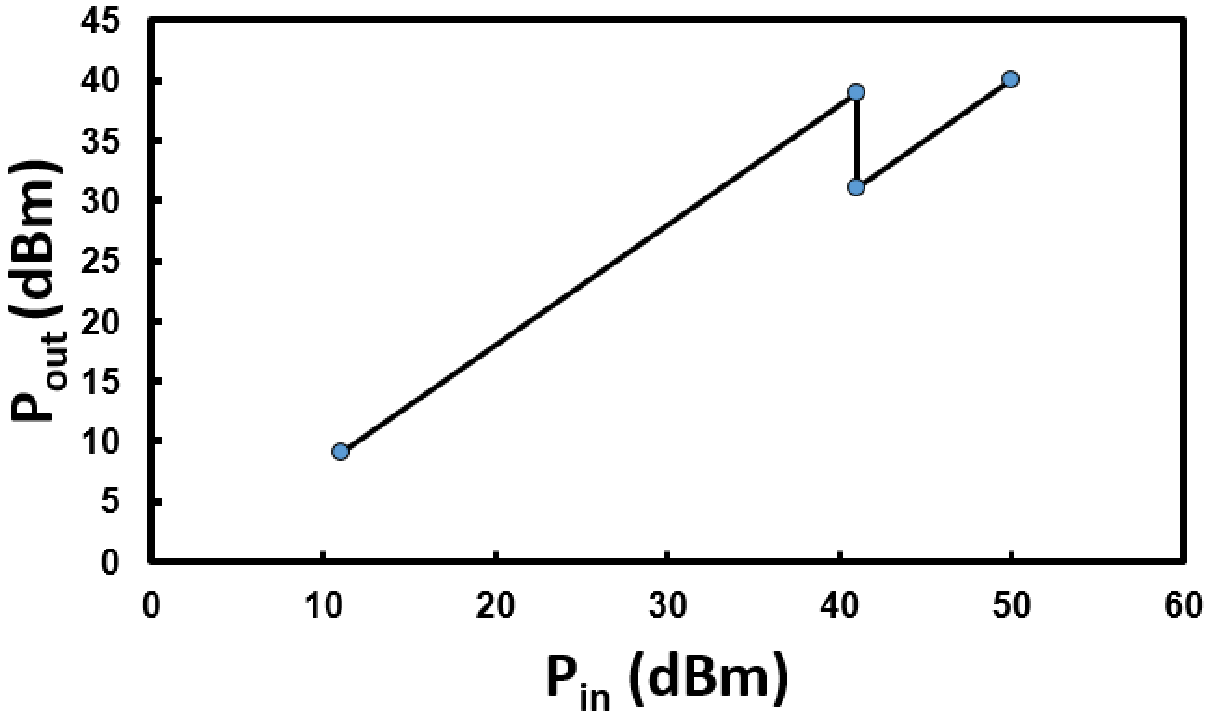

Figure 3.22. Measurement results of high-power testing. P_{in} is the input power to the coupler and P_{out} is the output from DUT.

3.4 Using tunable filters in FDPL circuits

A tunable filter was designed to be used in the proposed FDPL limiter circuit. At this point, the filter was designed using varactors. It should be noted the Q of the filter does not have an impact on the performance of the limiter. Thus, having a loss in the tunable filter in this instance in fact helps, since it makes it possible to distribute the heat dissipation between the termination loads and the filter when the switches are switched ‘on’. It is important to ensure that the varactor values cover all the range we are looking for. For this purpose, the initial design should aim for the middle varactor value, (which is 0.5 pF in this case), since the varactor used in the tunable filter is MACOM, MA46H120 [32]. The simulation results of the designed tunable filter for varactor values equal to 0.5 pF can be found in Figure 3.23.

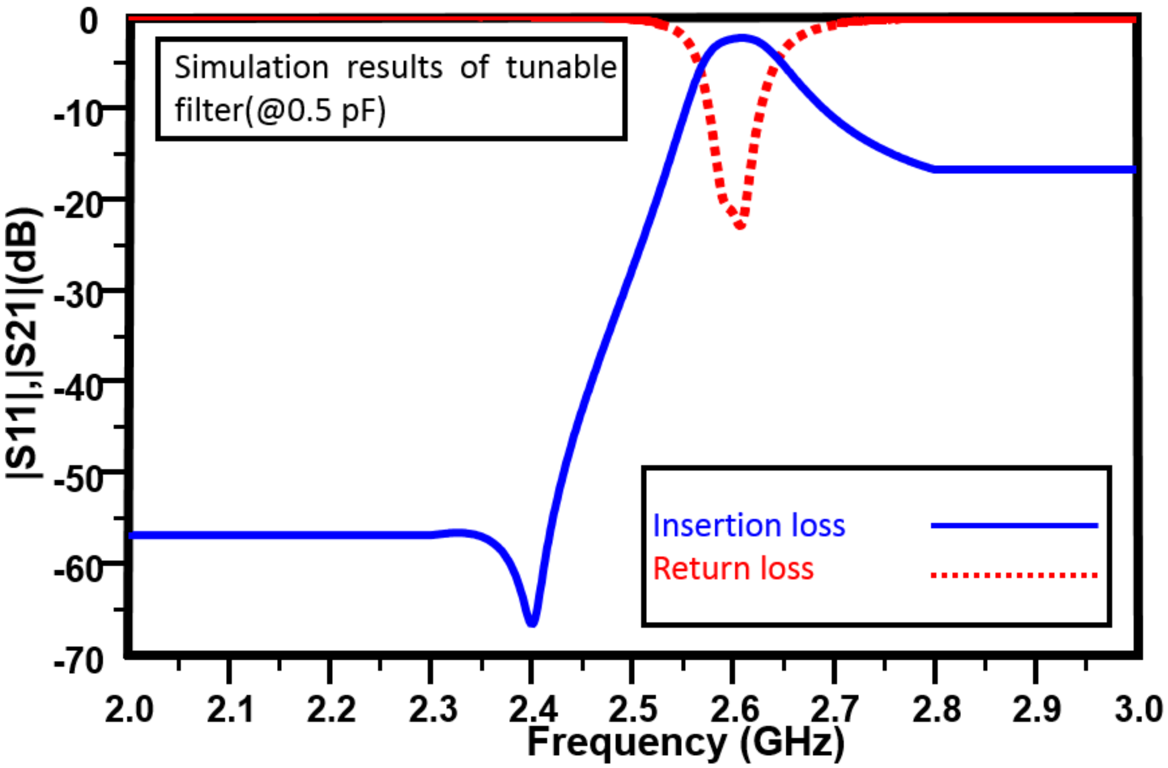

Figure 3.23. Simulation results of tunable filter with varactor values equal to 0.5 pF.

The varactors are inserted inside the resonator to vary capacitive loading and accordingly change the resonator's resonance frequencies. A $\lambda/4$ transmission line is used to eliminate the dc bias loading effect while allowing dc bias to be supplied to the varactors. In addition to varactors, chip capacitors are used in the resonators to prevent the varactor dc bias voltage from being shorted to the ground. The voltage range applied to this varactor can vary from 1 to 11 volts.

Figure 3.24 shows the fabricated tunable filter. It is tested as a standalone filter in order to ensure that tunability within the frequency range of the hybrid is achieved. The substrate used for the design and fabrication of the tunable filter and the tunable limiters was RO4003C, with 0.813 mm thickness. The metal used was 1 oz. copper with gold finishing. The measurement results of the filter with different voltage values applied to the varactor are given in Figure 3.25. Since the focus of this thesis is on frequency-dependent power limiters rather than on tunable filters, planar tunable filters are only used to demonstrate the concept. Certainly, tunable three-dimensional

(3D) cavity filters that are tunable in center frequency and bandwidth similar to the tunable filters presented in [33]-[34] would be ideal for use in such power limiter applications.

An integrated FDPL circuit with tunable filters is shown in Figure 3.26. OMRON switches are used for these circuits. Two control bias circuits were added – one to control the dc actuation voltage applied to the switch, and the other to control the dc bias applied voltages to the varactors that are integrated with the tunable filters. The circuit was also fabricated using Radant switches (RMSW220hp), as shown in Figure 3.27.

Figure 3.28 shows the RF measurement results (transmission) of the FDPL that employs the OMRON switches when both switches are in the 'off' state and when both switches are actuated with dc voltage while the varactors are biased at different voltages.

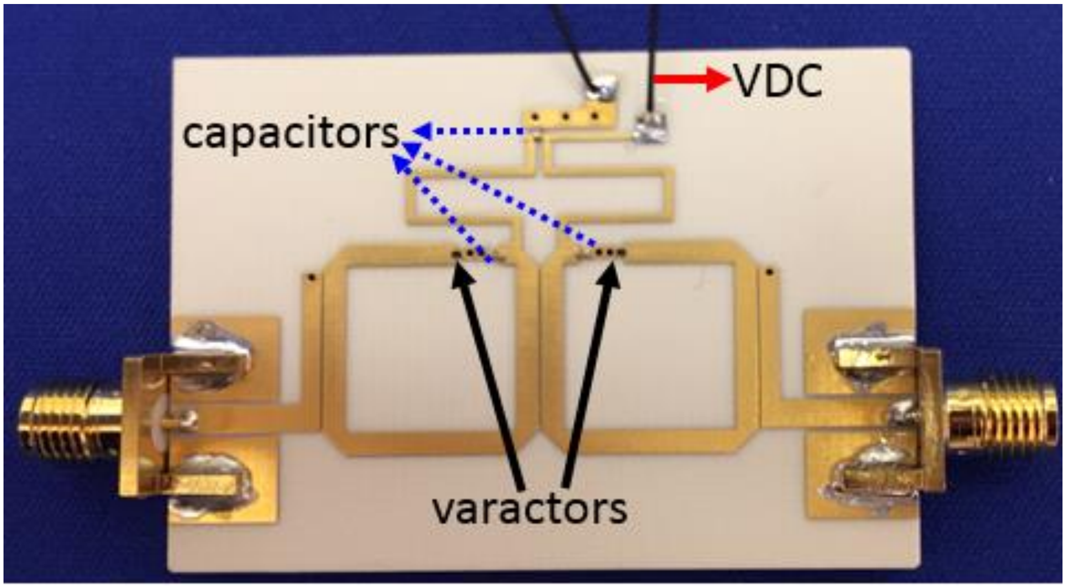

Figure 3.24. Tunable filter using varactors.

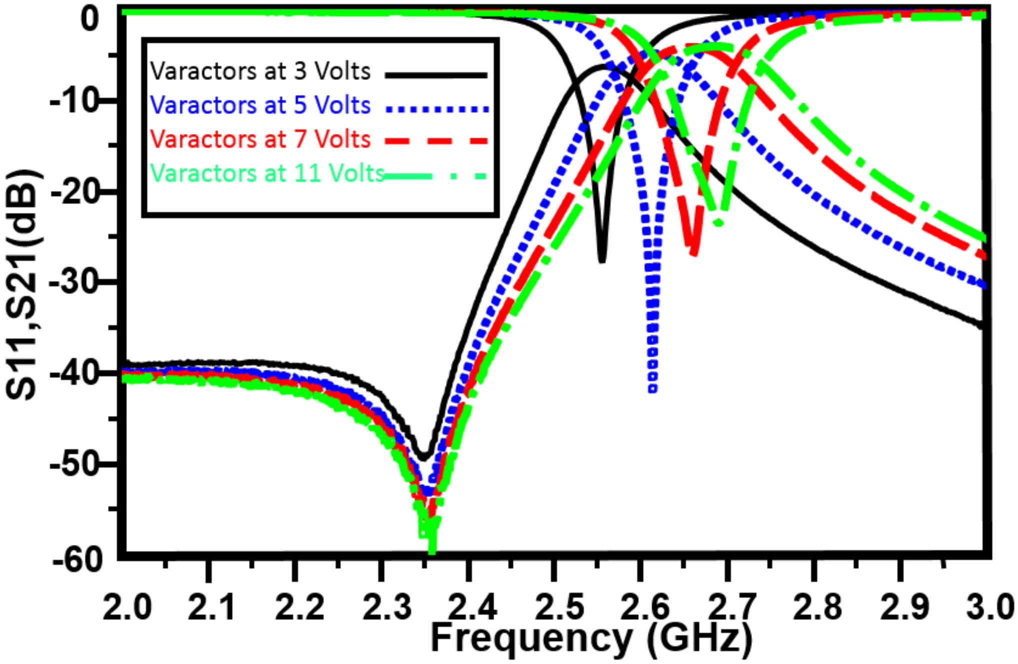

Figure 3.25. Measurement results of tunable filter with different voltages applied to varactors.

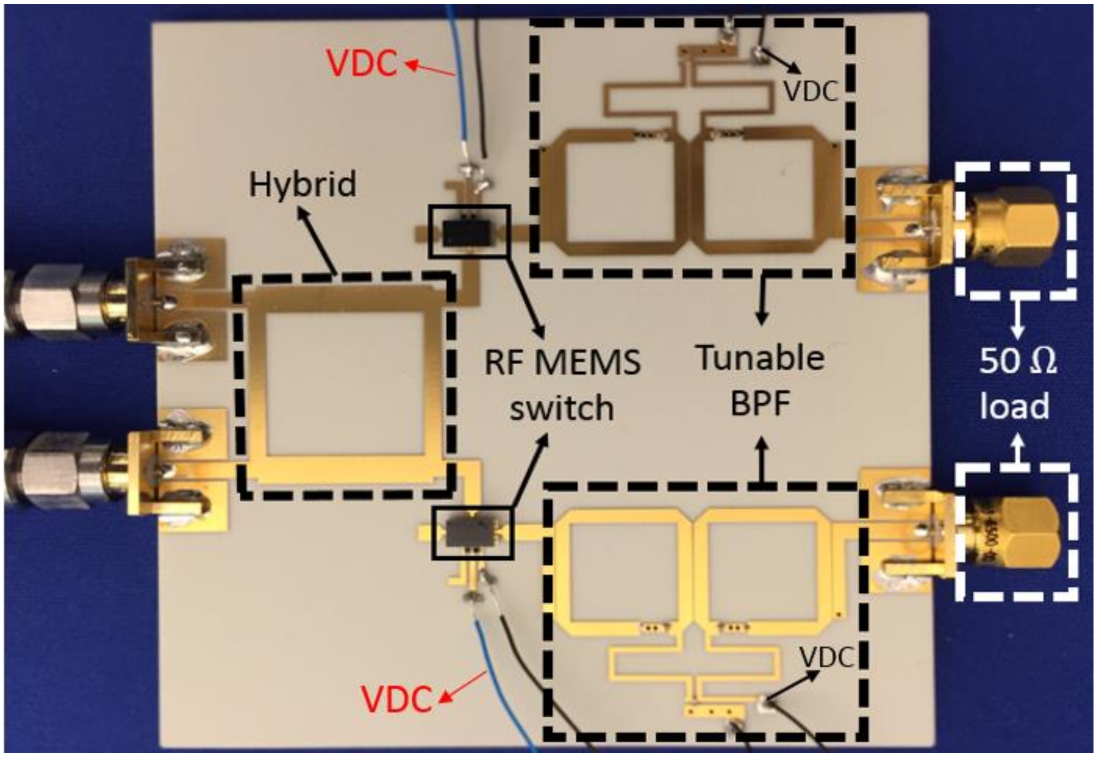

Figure 3.26. FDPL using tunable filters designed using OMRON switches.

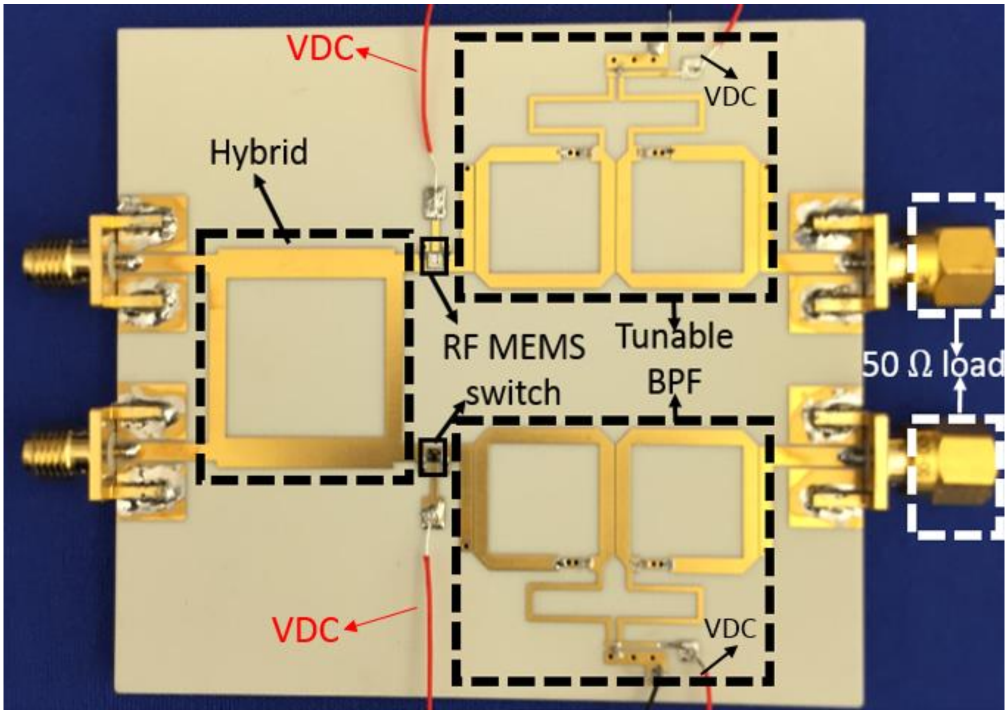

Figure 3.27. FDPL circuit using tunable filters and Radant switches.

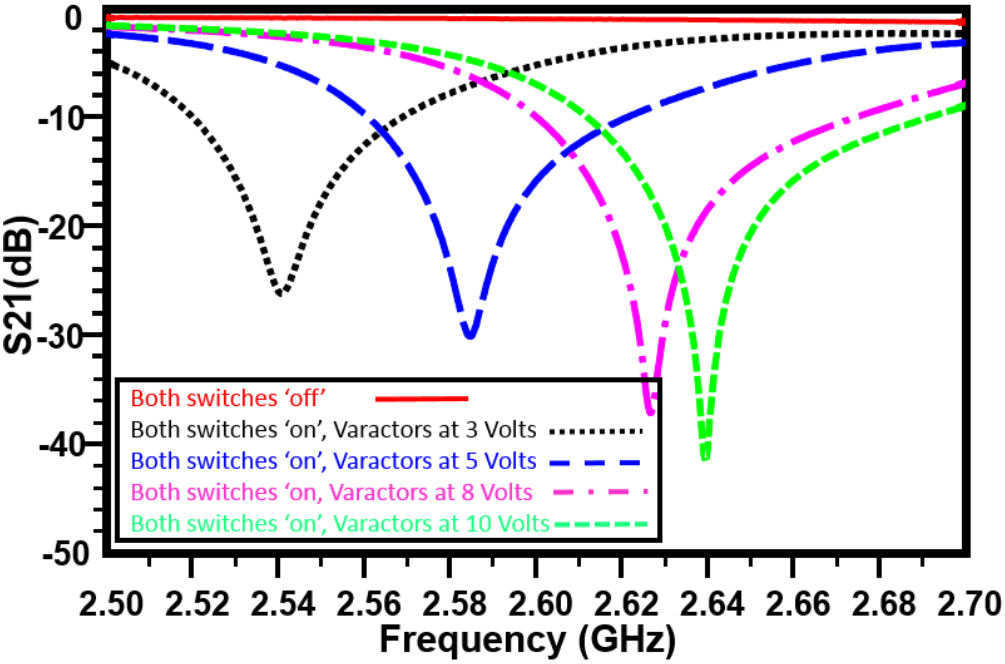

Figure 3.28. Measurement results of FDPL when both switches are 'on'.

4. A Novel method of thermally-actuated RF-MEMS switch actuation for power limiter application

The $P_{RF} - V_{dc}$ relationship for two commercial electrostatically-actuated RF MEMS switches was studied experimentally for Radant and OMRON in the previous chapter (Figure 3.14 and Figure 3.15). Due to the collapse nature of electrostatically-actuated switches that occurs when the gap between the cantilever and actuation pad approaches 1/3 of the original gap [7], the relationship obtained shows an abrupt change of P_{RF} versus V_{dc}, as illustrated in Figure 4.1. The large change in P_{RF} at dc bias voltage close to the pull-in dc voltage degrades the device sensitivity and limits the range of power levels that can be controlled by the dc bias voltage. In order to improve device sensitivity, it is desirable to have a linear or nearly linear relationship, as shown in Figure 4.1. In other words, it is desirable to have the dc actuation voltage control the self-actuation RF power level with a smaller slope of $P_{RF} - V_{dc}$.

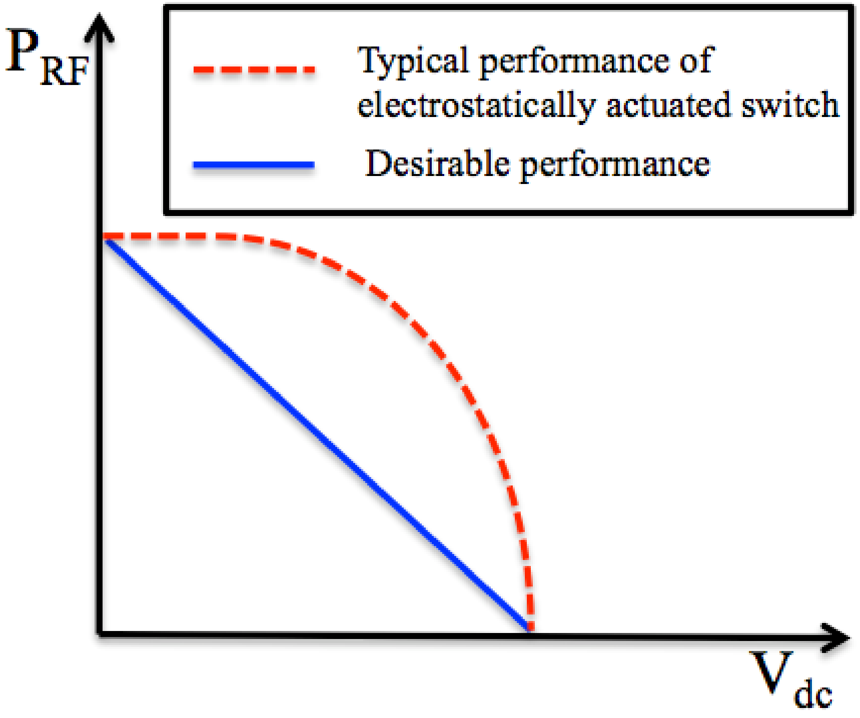

Figure 4.1. Conventional switch and ideal linear switch $P_{RF} - V_{dc}$ plots.

One potential option for achieving a desirable $\mathrm{P_{RF}} - \mathrm{V_{dc}}$ is to use thermally-actuated switches, as thermal actuators do not suffer from the cantilever collapse phenomenon which occurs in electrostatically-actuated switches and the main reason is that the thermal actuation mechanism decouples the RF self actuation from the electrostatic actuation. Another objective for using thermally-actuated switches is that they are able to handle relatively higher power levels than electrostatically-actuated thin film cantilever switches. This ability will be useful in power limiter applications that need to limit high power levels.

In this thesis, the concept of using thermally-actuated switches in power limiter applications is studied for the first time to determine the relationship between $\mathrm{P_{RF}}$ and thermal actuation $\mathrm{V_{dc}}$ voltages for such switches. A thermally-actuated switch fabricated using the Metal-MUMPS process is investigated both theoretically and experimentally. Both COMSOL mechanical/thermal and HFSS simulations are coupled to have a multiphysics analysis of. the relationship obtained between $\mathrm{P_{RF}}$ and $\mathrm{V_{dc}}$ illustrates the advantages of using thermally-actuated switches in power limiter applications.

4.1 Fabricated thermally-actuated Metal-MUMPS switch RF measurements

Figure 4.2 shows a schematic configuration of the thermally-actuated switch investigated in this study. The actuator used in the switch is the metal-based V-shaped thermal MEMS actuator employed in [35-37]. Two sets of Nickel beams are anchored to the substrate on one side and connected to the shuttle on the other side. A dc voltage is applied to dc beams shown in Figure 4.2. As a results heat is induced in the polysilicon resistance and eventually transferred to the nickel shuttle that is in direct contact with the polysilicon resistance through a thin film of silicon nitride. The heated resistor causes the array of beams in the chevron actuator to move forward, initiating a forward movement in a flexible arm. The flexible arm carries a contact plate that establishes contact between the two signal lines. The contact plate is isolated from the actuator through the use of a nitride layer. The thickness of all metal Nickel structures is 20 μm [38].

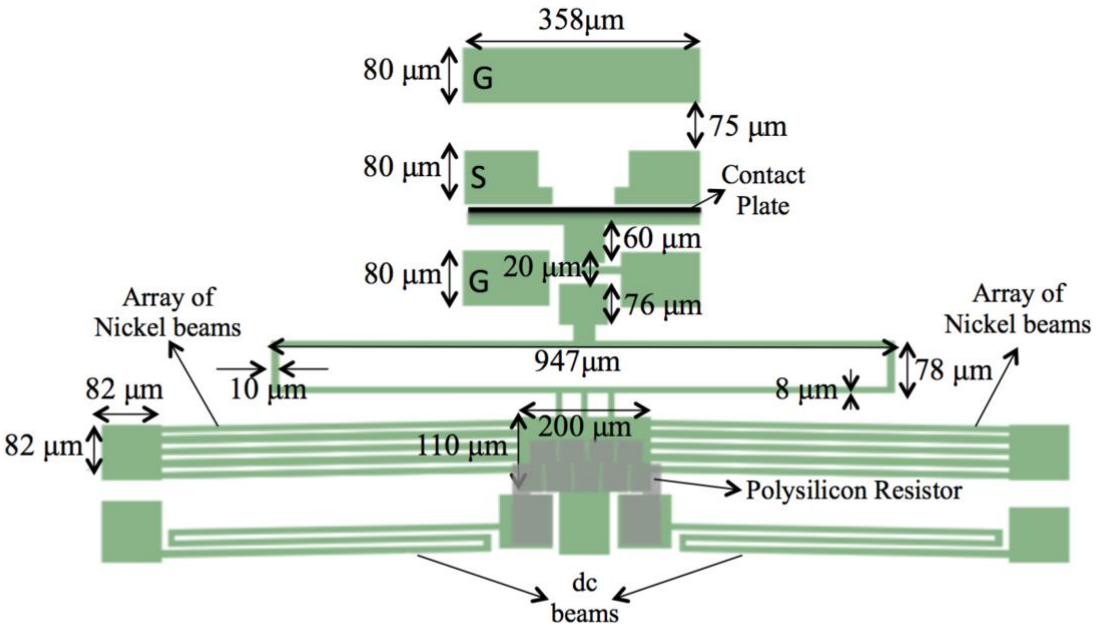

Figure 4.2. The layout of the proposed RF-MEMS switch.

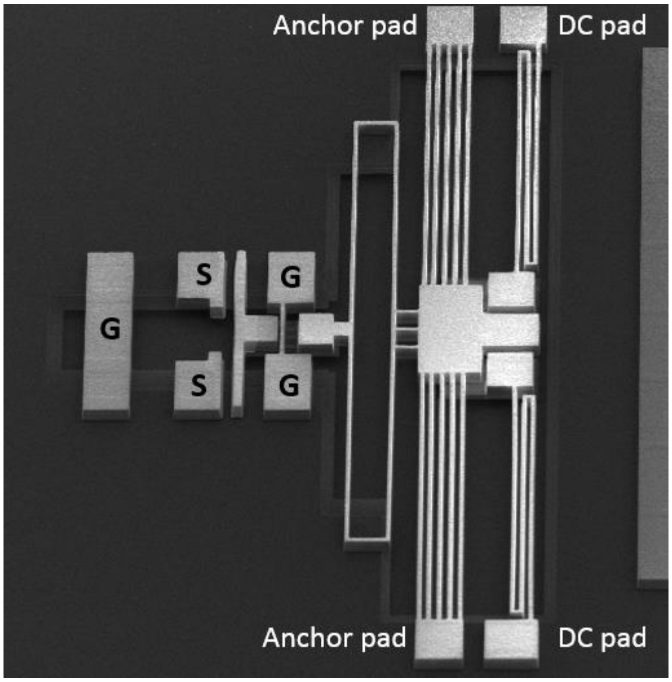

Figure 4.3. SEM picture of the fabricated thermally actuated switch.

Since this switch is designed for a self-actuation application, the overlap area between the signal lines and the contact plate has been maximized. The measurement results of the switch in ‘off’ and ‘on’ states can be found in Figures 4.4 and 4.5, respectively. The switch actuates at V_{dc} of the 11 volts applied to the dc pads, as shown in Figure 4.3.

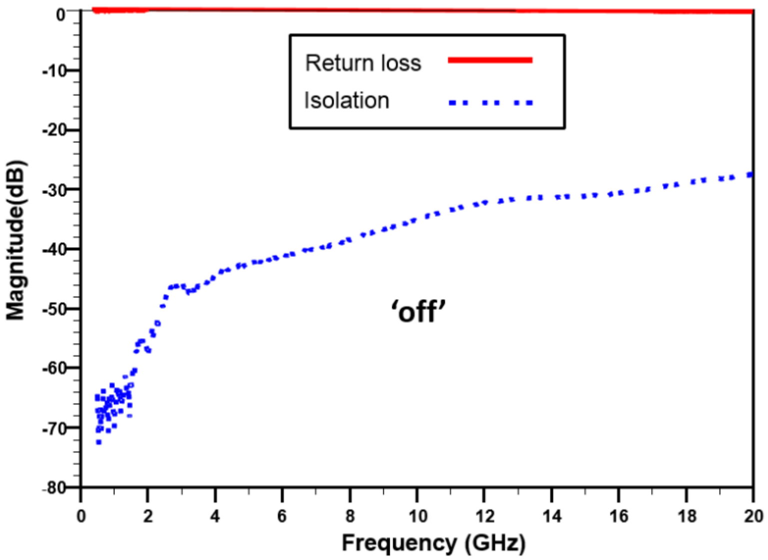

Figure 4.4. Measurement results of the switch in ‘off ‘state “isolation”.

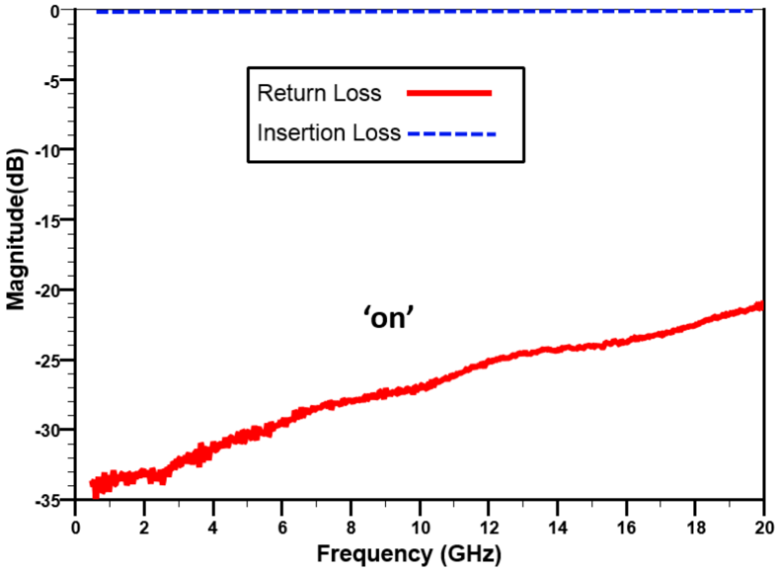

Figure 4.5. Measurement results of the switch in ‘on‘ state.

4.2 Thermal and electrostatic analysis of the switch

COMSOL Multiphysics [39] is used to model the proposed switch. The first set of simulations is the thermal simulations through applying a dc voltage, $V_{thermal}$. A list of the material characteristics used in the switch can be found in Table 4.1. The coupled structural-thermal simulation is done in order to obtain the displacement caused by the applied voltage V_{dc}, which in turn controls the gap between the contact plate and the signal lines.

Table 4.1. Materials used in Metal MUMPS

Material	Thermal Conductivity (W/mK)	Electrical Conductivity (S/m)	Thermal Expansion Coefficient (1/K)	Heat Specific J/(kg.K)	Mass Density (kg/m^3)	Young's Modulus (Pa)
Nickel	90.7	1.25e7	13.4e-6	445	8900	205e9
Gold	317	4.347e7	14.2e-6	129	19300	79e9
Poly	150	78125	2.6e-6	600	2230	169e9
Sio2	1.42	0	0.5e-6	1000	2150	70e9
Nitride	18.5	0	2.8e-6	170	3440	385e9
Si	20	2.5e4	2.6e-6	600	2230	169e9

The physics applied in these simulations are heat transfer in solids, structural mechanics, and electric currents. The von Mises stress plot of the actuator at 11 volts is shown in Figure 4.6. In order to simulate the 3D structure of the switch with the exact dimensions, the layout of the fabricated switch has been imported as GDS file into COMSOL.

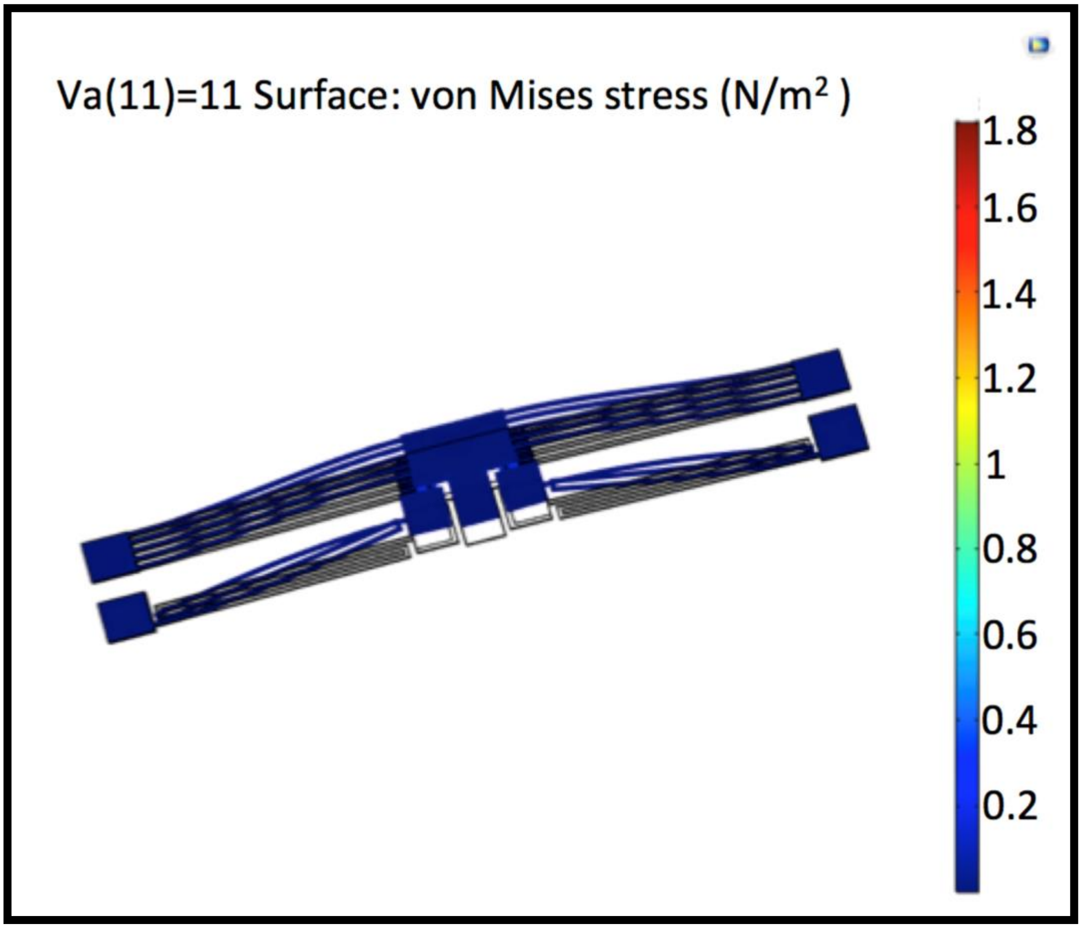

Figure 4.6. The von misses stress caused by applying 11 volts.

By varying the applied dc voltage V_{thermal}, the actuator displacement changes. Figure 4.7 shows the displacements found from sweeping the voltage from 0 to 11 volts. The dc voltage applied to the thermal actuator is called V_{thermal} in the analysis, which is the actuation voltage (V_{dc}) that we would like to relate to P_{RF}. Table 4.2 gives the relationship between V_{thermal} and the gap between the contact plate and the signal lines, which is derived by subtracting the displacements given in Figure 4.7 from the initial gap of 11 μm for this switch.

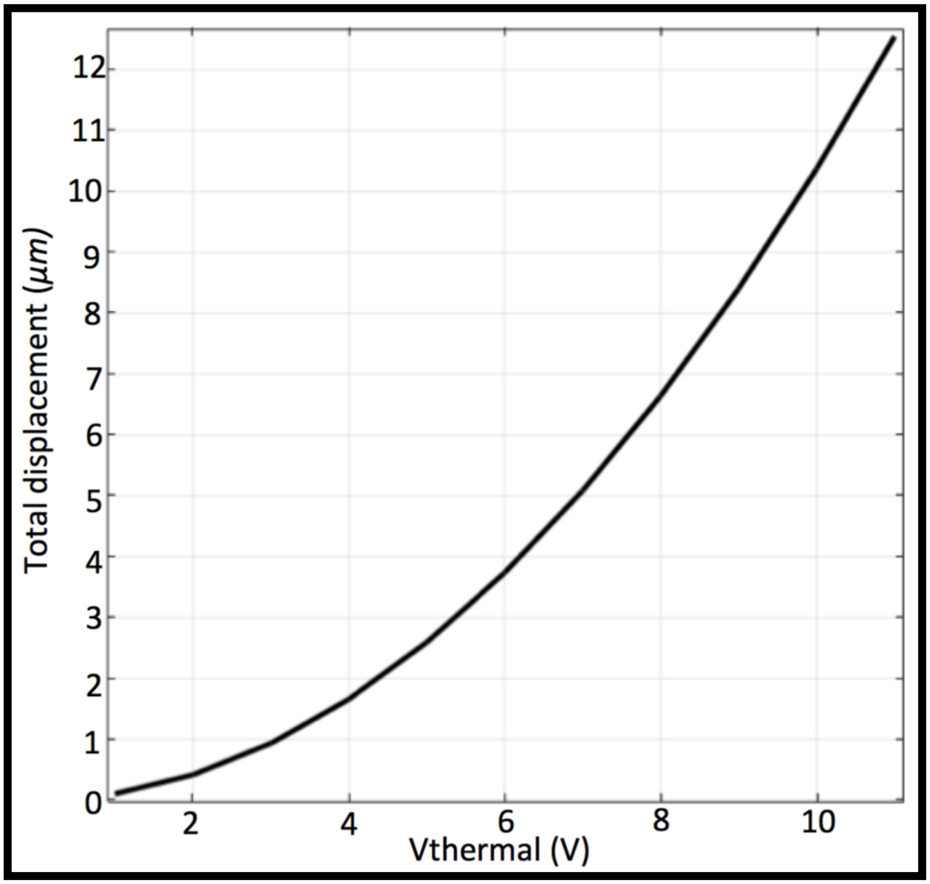

Figure 4.7. Displacement versus Vthermal plot found from COMSOL thermal simulations.

Table 4.2. $V_{thermal}$-Gap table

$V_{thermal}$ (V)	Gap (μm)
0	11
1	10.89
2	10.58
3	10.06
4	9.34
5	8.41
6	7.27
7	5.92
8	4.36
9	2.6
10	0.63

The results shown in Table 4.2 are plotted in Figure 4.8. The curve is fitted into a 6th order polynomial as $V_{\text{thermal}} = \text{f (gap)}$.

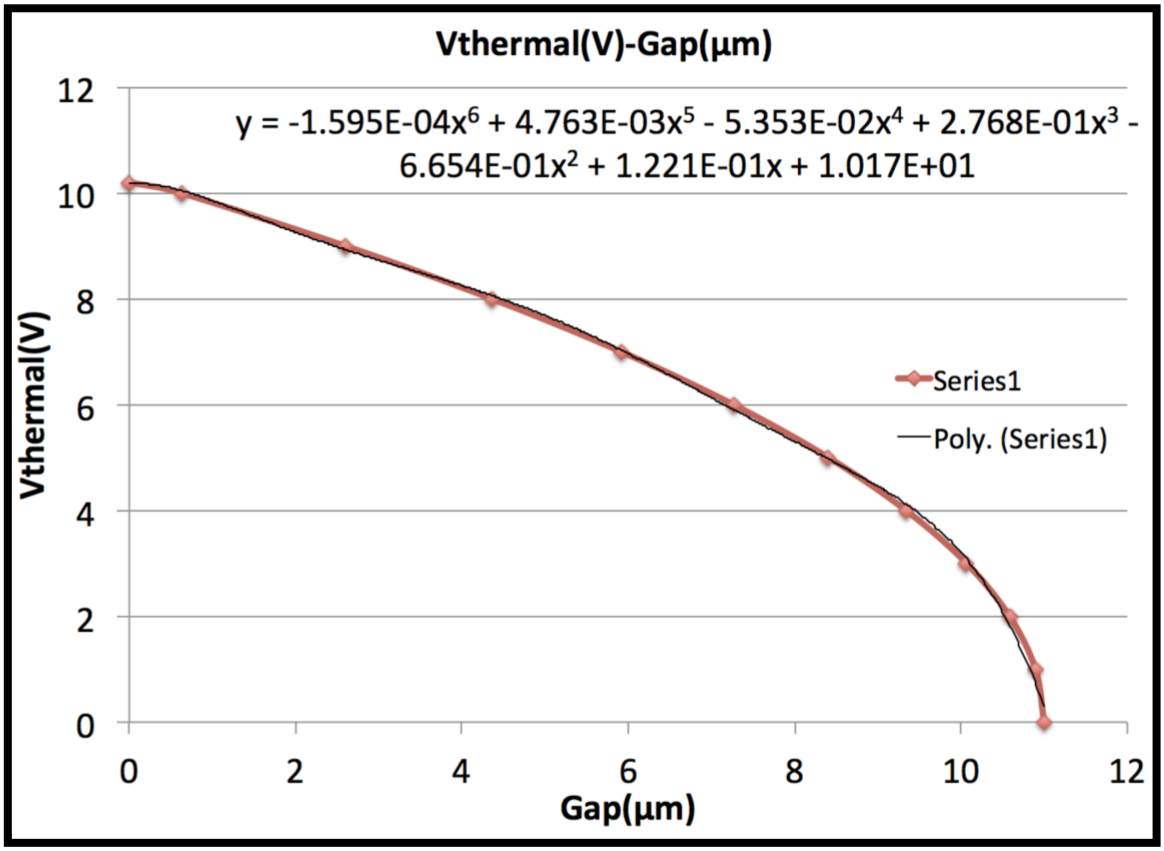

Figure 4.8. The fitted V_{thermal}-Gap plot and the derived polynomial.

The equation shown in Figure 4.8 can be used to find the gap for an applied actuation voltage of V_{thermal}. The next step is to carry out an electrostatic analysis to determine the electrostatic pull-in voltage needed for a given gap to pull the contact plate to establish a contact between signal lines, i.e., to turn the switch to the 'on' state. This electrostatic voltage is denoted as $V_{\text{electrostatic}}$ and is the voltage between the contact plate and one of the signal lines.

Figure 4.9 shows the location of the terminal and ground boundary conditions applied for the electrostatic analysis in COMSOL. It should be noted that the terminal boundary condition is applied only to one side of the switch, which represents the input. (This is shown later in section 4.4, when dealing with the electromagnetic analysis of the switch; as can be seen, there is a build-up of RF electric field only at the input side of the switch.). The results obtained for the

$V_{\text{electrostatic}}$ and the gap are given in Table 4.3. The results plotted in Figure 4.11 are also fitted into a 5th order polynomial, where x represents the gap and y represents $V_{\text{electrostatic}}$ (gap $= g^{-1}(V_{\text{electrostatic}})$.

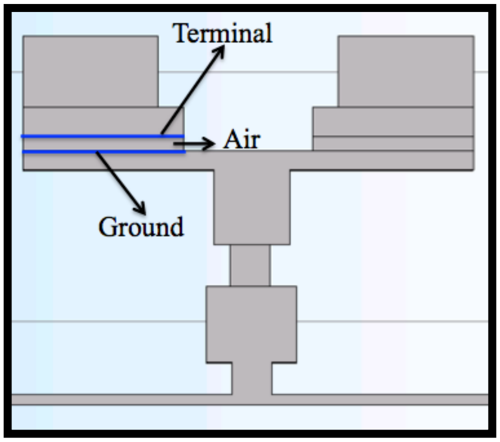

Figure 4.9. Terminal and ground boundary conditions applied in COMSOL.

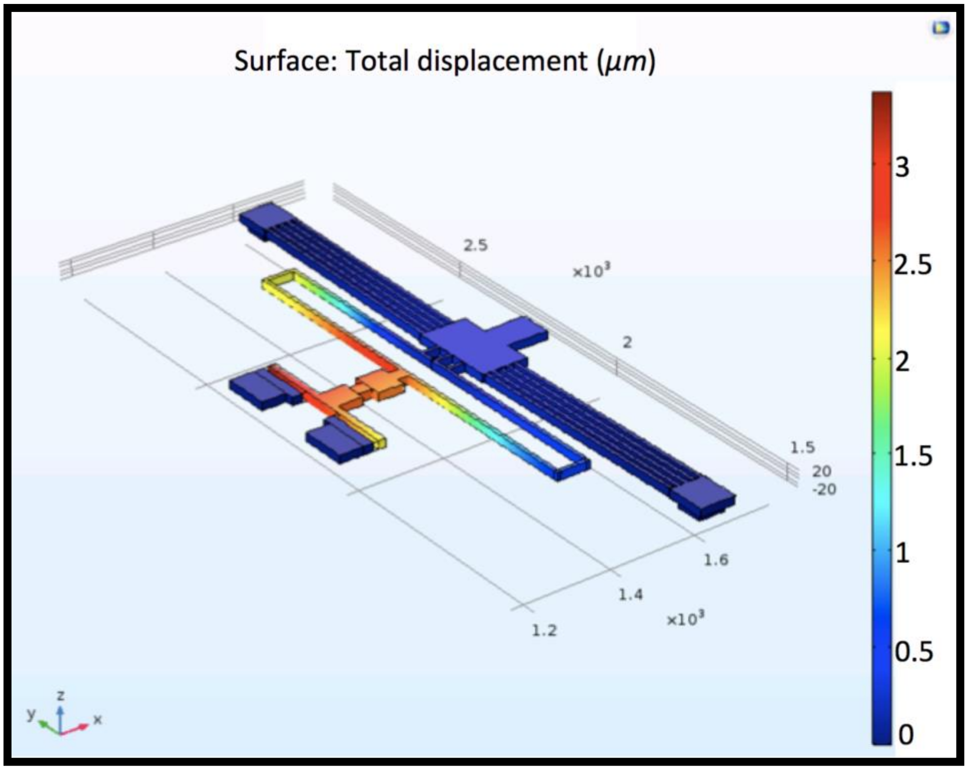

Figure 4.10. An example of displacement in COMSOL.

Table 4.3. $V_{electrostatic}$-Gap table

$V_{electrostatic}$ (V)	Gap (µm)
13.01	0.89
15.83	1
41.61	1.9
55.44	2.3
124.8	4
189.05	5.3
219.69	6
293.44	7
414.78	8.8
588	11

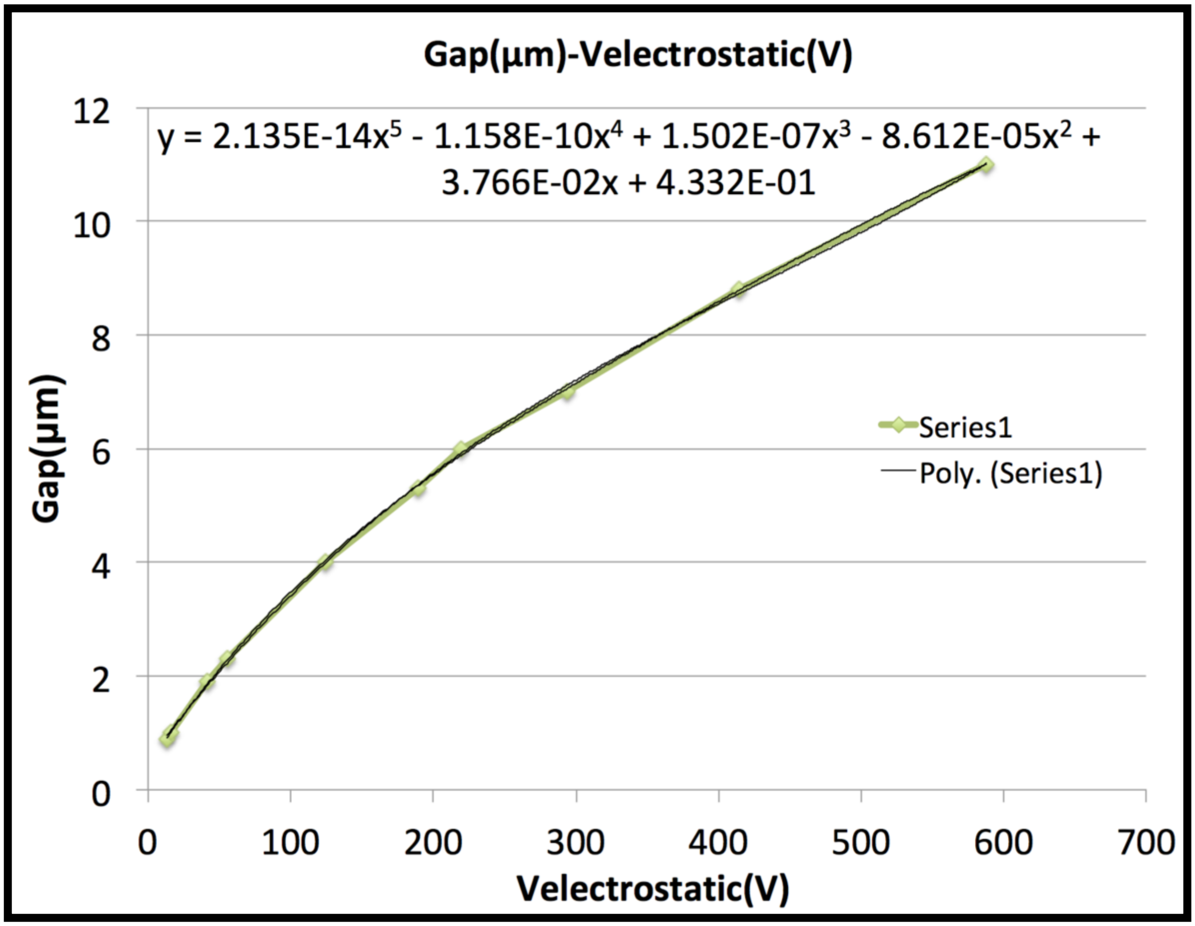

Figure 4.11. The fitted gap-$V_{thermal}$ plot and the derived polynomial.

The two polynomials are used to find the relationship of $\mathrm{V_{thermal}}$ versus $\mathrm{V_{electrostatic}}$ as $\mathrm{V_{thermal}} = \mathrm{f}\left(\mathrm{g}^{-1}(\mathrm{V_{electrostatic}})\right)$. The $\mathrm{V_{thermal}} - \mathrm{V_{electrostatic}}$ plot is shown in Figure 4.12.

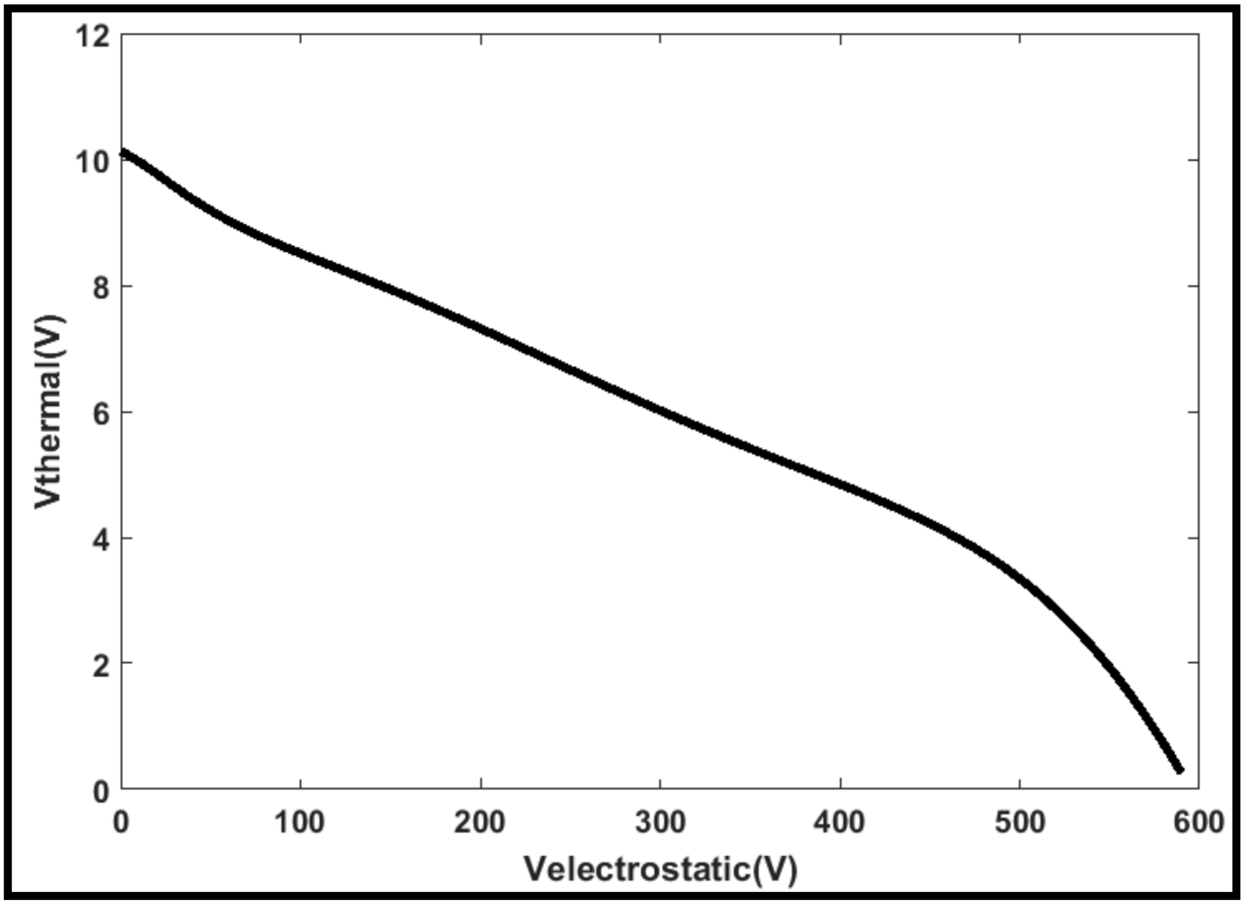

Figure 4.12. $\mathrm{V_{thermal}}$-$\mathrm{V_{electrostatic}}$ plot.

Figure 4.12 basically gives the electrostatic voltage needed between the signal line and the contact plate for a given gap (i.e., for a particular $\mathrm{V_{thermal}}$ value). For example, for an applied $\mathrm{V_{thermal}}$ of 9 volts, the thermal actuator will move forward to reduce the gap from 11 μm to 2.6 µm, as given in Table 4.2. One then can estimate the $\mathrm{V_{electrostatic}}$ needed to pull the contact pad to the signal lines of the CPW port, which, in Figure 4.12, is found to be 66.55 volts.

4.3 High RF power simulations of the Metal-MUMPS thermally-actuated switch

In order to find the $P_{RF} - V_{thermal}$ plot, we need to find the RF electric field between the contact plate and the signal line as a function of the input RF power. We first assume an input power of 1 Watt and calculate the RF E-field. Since P_{RF} is proportional to E^2, the RF E-field at any other input power level can then be readily calculated. A plot for the field distribution as generated from HFSS for an input power of 1 Watt and a gap of 8.8 um is shown in Figure 4.13.

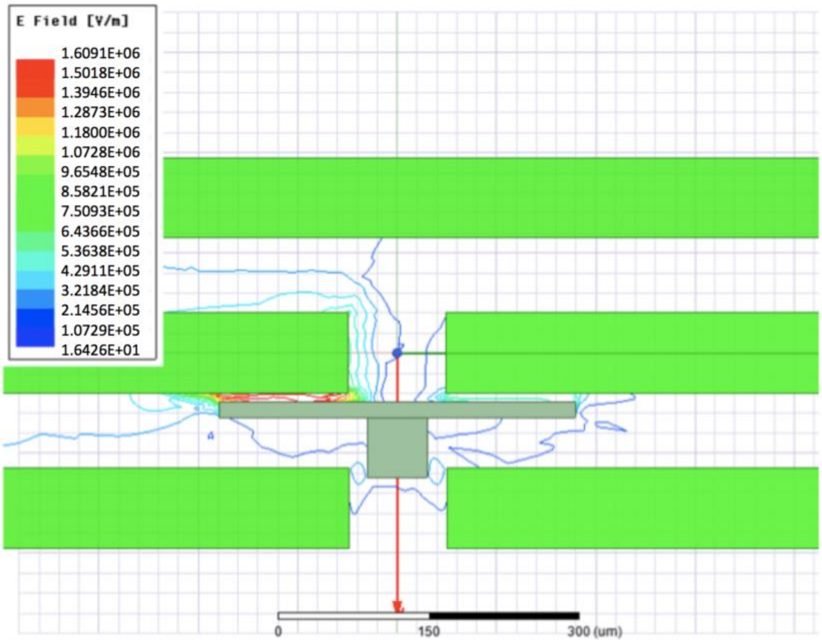

Figure 4.13. E-field plot in HFSS.

The RF simulation is repeated for different gaps and the E-field results are given in Table 4.4, along with the V_{RF} associated with each gap. V_{RF} is calculated by Multiplying a gap by the maximum electric field calculated from HFFS for that gap.

Table 4.4. Thermally actuated switch HFSS simulation results (assuming 1 watt of input RF power)

Gap (μm)	V_{RF} (V)
0.89	10.54
1	11.407
1.9	10.615
2.3	11.933
4	13.539
5.3	13.264
6	13.669
7	14.806
8.8	14.16

The COMSOL electrostatic results shown in Table 4.3 can then be used to calculate the power P_{eqvc} that effectively equals P_{RF}, which will cause self-actuation for a given gap. Hence, Tables 4.3 and 4.4 (or equivalent polynomials) along with Equations 4.1 and 4.2 can be used to generate Table 4.5.

$$1W = KV_{RF}^{\ 2} \qquad (4.1)$$

$$P_{eqvc} = KV_{electrostatic}^{\ 2} \qquad (4.2)$$

The results given in Table 4.5 are used to plot $P_{RF} - V_{dc}$, as shown in Figure 4.14. Note that P_{eqvc} is the RF power that will self-actuate the switch.

Table 4.5. Combining all tables to find $V_{thermal}$ (V) versus Peqvc (W)

Gap (μm)	$V_{thermal}$ (V)	$V_{electrostatic}$ (V)	P_{eqvc}(W)
0.89	10.9133	13.01	1.522
1	10.8912	15.83	1.923
1.9	10.6182	41.61	15.366
2.3	10.4442	55.44	21.576
4	9.3401	124.8	84.971
5.3	8.0900	189.05	203.119
6	7.2696	219.69	258.309
7	5.9193	293.44	392.753
8.8	2.9679	414.78	858.021

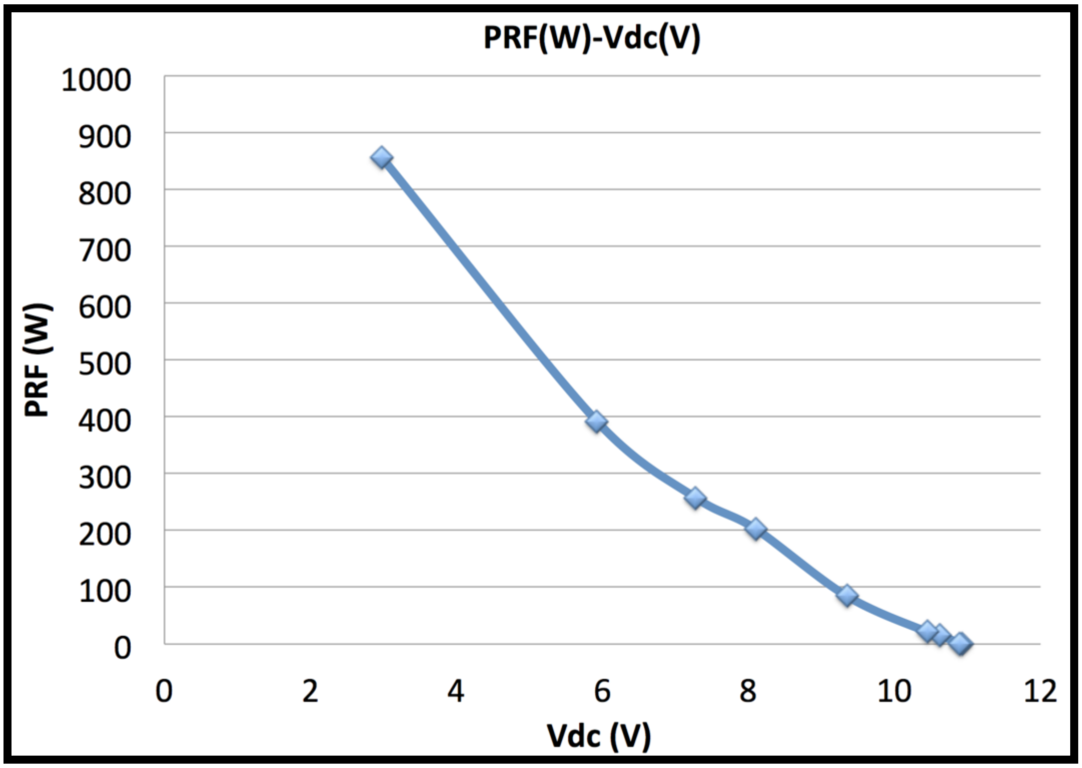

Figure 4.14. The $P_{RF} - V_{dc}$ plot of the switch.

Each point of the plot shown in Figure 4.14 represents an actuation point, using both V_{dc} and P_{RF}. For example, when V_{dc} ($V_{thermal}$) is 11 volts, the chevron actuator moves forward enough to close the switch and the contact plate will be in touch with both signal lines, i.e., the switch is already at the 'on' state. However, if the $V_{thermal}$ is reduced, for example, from 11 volts to around 10 volts, the displacement of the chevron actuator is not enough to close the gap. The RF power needed for self-actuation is around 35 Watts.

It should be noted that the RF power levels needed for self-actuating this particular switch is relatively high. This is attributed to the large thickness of 20 µm used for the nickel beams and the rigidity of both the Chevron actuators and the beams that connect the actuator to the contact plate. The self-actuation RF power levels can be certainly reduced by optimizing the mechanical design.

4.4 Measurement results

Since the gap between the signal line and the contact plate is relatively higher than that encountered in electrostatic-actuated switches, the RF power levels that self-actuate the switch are relatively high, as can be seen in Figure 4.14. However, it is difficult to carry out high power RF testing at such extreme power levels in a university lab.

In order to verify the validity of the results reported, an alternative experimental approach is used for the simulation results. Since the V_{RF} voltage between the signal line and the contact can be represented by $V_{electrostatic}$, the following experiment is carried out.

1) The switch is thermally actuated by a voltage called $V_{thermal}$. The displacement of the chevron actuator will reduce the gap between the contact plate and the signal line.

2) With $V_{thermal}$ applied, a dc voltage is then applied between the signal line and the actuation pad to actuate the switch into the 'on' state, i.e., to pull the contact plate to the signal lines.

3) Repeating the test for various values of $V_{thermal}$ will lead to a relationship between $V_{thermal}$ and $V_{electrostatic}$.

COMSOL thermal and electrostatic analyses are used to verify these experimental results. It should be noted that in the electrostatic COMSOL analysis, dc voltage is applied between the contact plates and the signal lines at both sides of the switch. The dc voltage is applied between the signal lines in the actual experiment, since the contact plate is carried by a dielectric and is considered electrically as a floating metal. However, the mechanical support is taken into consideration in the COMSOL analysis. A comparison between the theoretical and experimental results obtained for $\mathrm{V_{thermal}}$ versus $\mathrm{V_{electrostatic}}$ is done. The actuation voltage found experimentally ($\mathrm{V_{thermal}}$) was equal to 9.8 volts, however going back to the displacement versus $\mathrm{V_{thermal}}$ plot of the switch, found from thermal simulations in COMSOL, it is found that for this switch which is supposed to have 11 μm gap between the actuation plate and signal lines the actuation voltage is supposed to be 10.2 volts. The reason of this difference could be an issue in the fabrication process, which has caused a gap change. Both of these actuation points are shown in displacement-$\mathrm{V_{thermal}}$ plot in Figure 4.15.

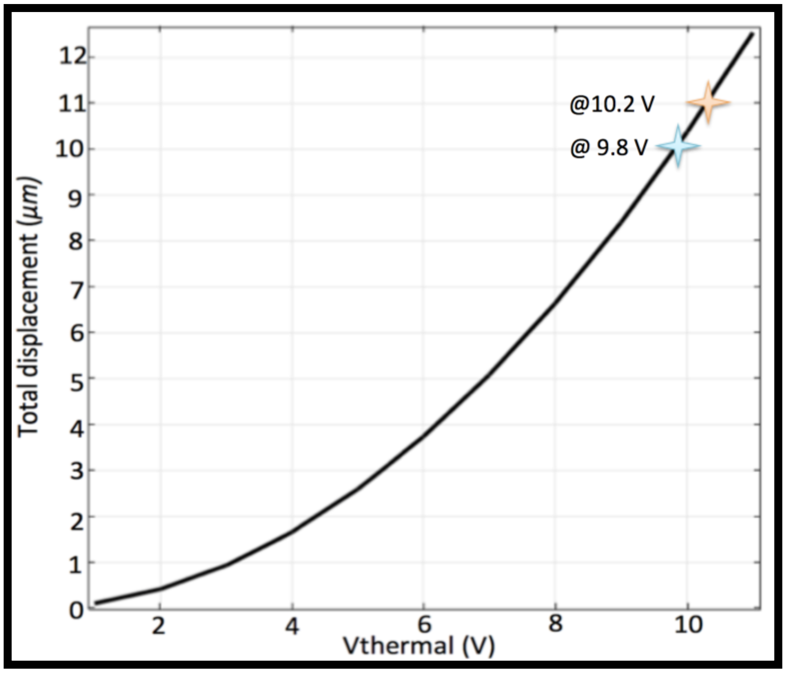

Figure 4.15. Displacement versus $\mathrm{V_{thermal}}$ plot found from COMSOL thermal simualtions.

In order to find the $\mathrm{V_{thermal}} - \mathrm{V_{electrostatic}}$ response of the switch, COMSOL thermal and electrostatic simulation results of the switch are combined in MATLAB. The results are shown in Figure 4.16. The electrostatic voltage is applied between the signal lines in measurements while it is applied between the actuation plate and signal lines on both sides of the switch in simulation. Applying voltage V across the signal lines imposes the electric field equal to the case when 2V is applied between the actuation plate and signal lines. Therefore, $V_{electrostatic}$ voltages found from simulations are doubled and a new $V_{electrostatic} - \text{Gap}$ polynomial is derived to compare simulation and measurement results.

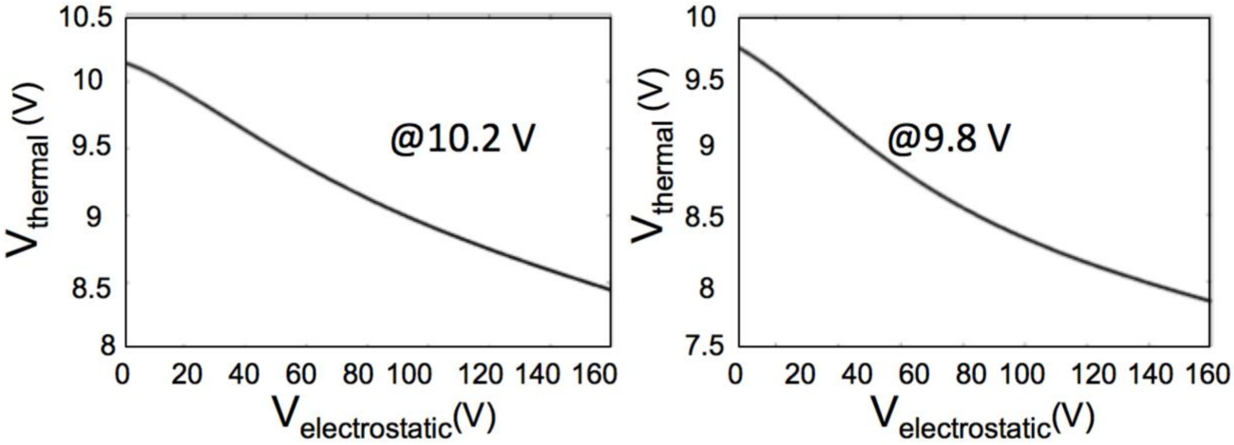

Figure 4.16. $V_{thermal}$-$V_{electrostatic}$ MATLAB plots for 9.8 and 10.2 volts.

The simulation and measurement results of the switch can be found in Figure 4.17.

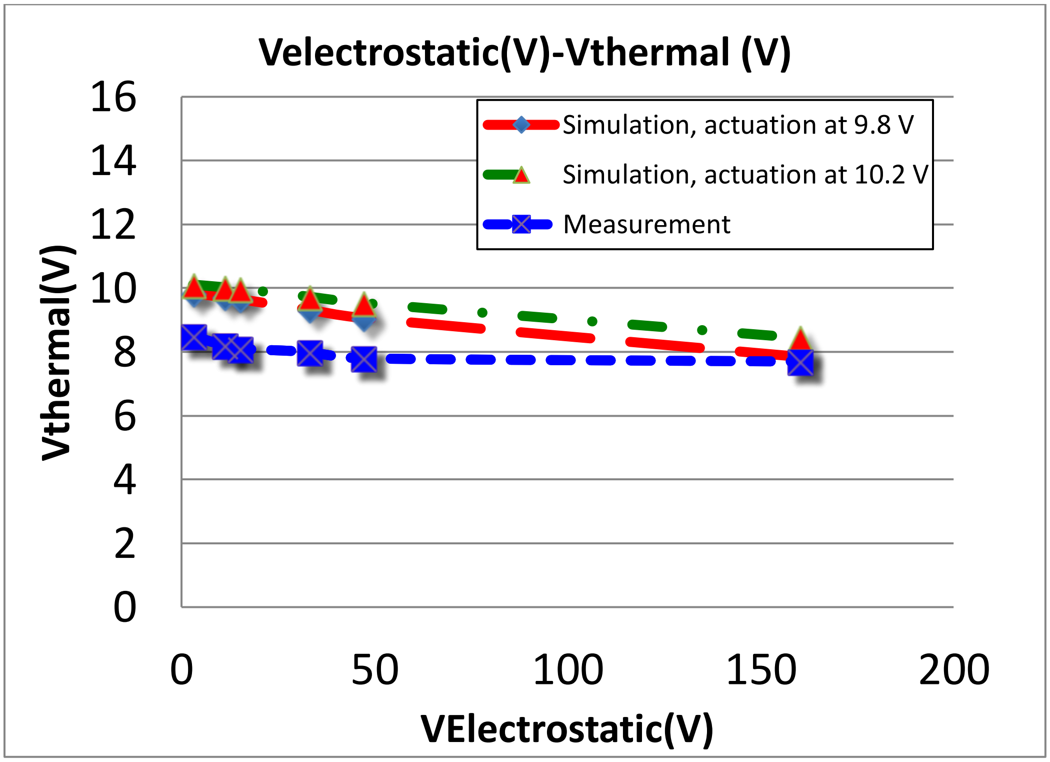

Figure 4.17. Measurement and simulation results.

5. A Novel low-temperature superconductor power limiter

Direct digitization of wideband RF signals with very low dc power consumption is possible at Low-temperature superconductor receivers [41]. Junctions based on rapid single flux quantum (RSFQ) technology [41] are used in building superconductor analogue to digital converters (ADC) that must be protected from high-power RF signals. The proposed circuit is intended to provide protection against power levels of a few dBm, as these can still damage RSFQ junctions. Another objective is to have the power protection circuit monolithically integrated with the receiver chip.

High-temperature superconductor (HTS) transmission lines made of yttrium barium copper oxide (YBCO) film have been employed in power limiter applications where a transmission line (TL) switches from a superconducting state to a normal state [42], [43]. As the RF current exceeds the critical current when operating at high power levels, the HTS YBCO microstrip line effectively becomes a line of insulator with characteristic impedance that is markedly different from the 50-Ohm impedance exhibited by the HTS microstrip line in the superconducting state. This, in turn, causes the majority of the signal to reflect back to the input of the HTS TL. Such HTS power limiters offer superior performance compared to conventional power limiters, which use semiconductor diodes [44], [45].

However, the technologies (HTS and semiconductor) cannot be integrated monolithically with the LTS receiver chip. One may assume that the same HTS concept can be applied to LTS by simply using a narrow-width superconducting niobium (Nb) microstrip or coplanar transmission line. However, the LTS transmission line is made of niobium film that can still be considered normal metal at high power, not an insulator, as is the case with the HTS microstrip line. The idea of using lumped-element niobium filters in power limiter applications was conceived during testing niobium lumped-element filters at cryogenic temperature (4K). It was observed that increasing the input power level of the PNA from a low power level to a high power level resulted in a circuit that reflected the input power. When testing a niobium transmission line at the same power levels, however, the performance of the transmission line did not change.

Moreover, it is well known from filter theory that as the resonator Q changes from a very high value to a very low value, the filter insertion loss will increase significantly but the filter will still yield a reasonable return loss. This led us to investigate in detail the filter circuit both theoretically and experimentally. Upon investigating the inductors, we observed that the ones used in these LTS lumped-element filters switch from being inductive when the niobium is in the superconducting state to capacitive when the niobium is in the normal metal state. The filter circuit then consists of all capacitors rather than capacitors and inductors (resonators) reflecting the input power. For this purpose, lumped-element filters are designed and fabricated using a multilayer (4-layer) niobium process developed by the MIT-Lincoln Lab [46] for LTS applications. An LTS niobium protection circuit consisting of two hybrids and two lumped-element filters is presented. It is also illustrated how the concept can be employed to realize a T/R switch to isolate the transmit circuit from the receive circuit.

5.1 MIT_LL fabrication process

A cross-section of the MIT-Lincoln Lab multilayer LTS niobium-based process [46] is given in Figure 5.1. In this process, there are four superconducting layers (M3, M2, M1, and M0) and one normal layer (M4). The process allows insertion of vias between all metal layers. This fabrication method is very well suited for low-frequency lumped-element filter design, since the nm thickness of the oxide layers allows the realization of very high capacitance values. All devices reported in this paper are measured at our Lakeshore Cryogenic Probe Station [47].

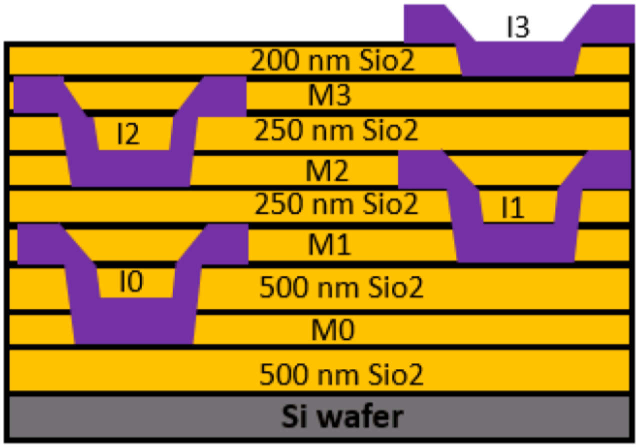

Figure 5.1. Cross-section of multilayer (4-layer) MIT-LL process. [46].

5.2 Coplanar transmission line simulation results

A niobium-based 50-ohm coplanar transmission line is simulated in Sonnet [48], using the same process. The simulation results of this line at room and cryogenic temperatures can be found in Figure 5.2. The width of the signal line simulated is 100 µm, with a 40 µm gap to the ground and a finite width of 200 µm.

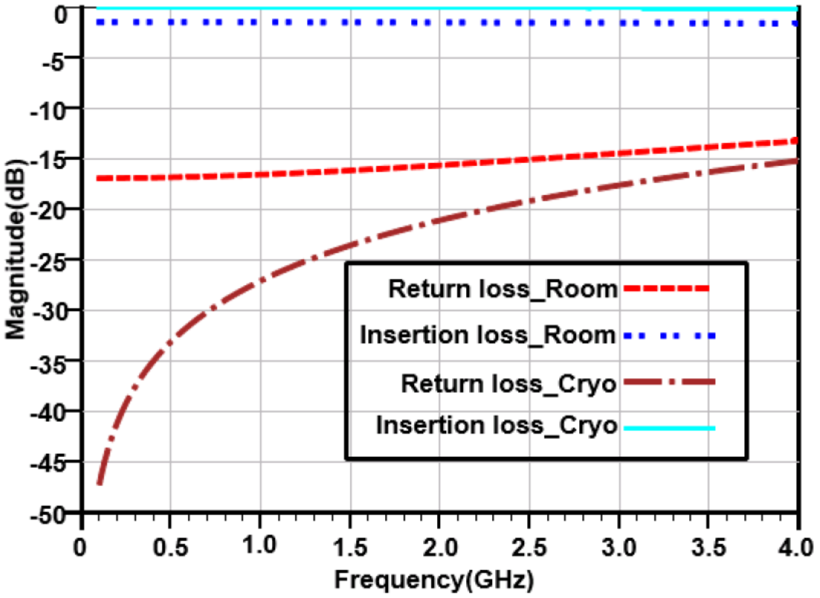

Figure 5.2. Simulation results of coplanar line in Sonnet.

It is observed that the transmission line in the normal state maintains a reasonable return loss. The majority of the RF power is transmitted to the output, with some of the RF power dissipated in the line due to the high resistivity of Nb in the normal state. The degradation in the return loss at low frequency from 45 dB to 15 dB is attributed to changes in the characteristic impedance. The impedance of the simulated coplanar line at room and cryogenic temperatures is shown in Figure 5.3. The characteristic impedance of the line presented in Figure 5.3 at both room and cryogenic temperatures is found using Equation 5.1. The lossy transmission line analysis can be found in [49].

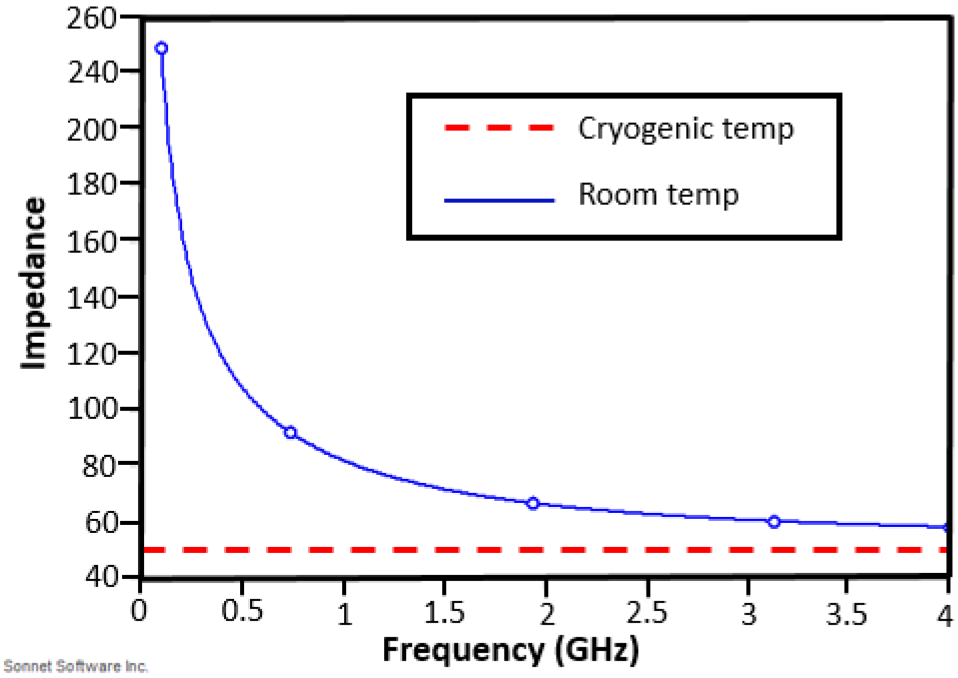

Figure 5.3. Impedance of coplanar line at cryogenic and room temperatures.

5.3 7-pole filter design and simulations

A 7-pole niobium lumped-element filter is designed with a center frequency of 416 MHz and a bandwidth of 326 MHz. The circuit model and the ideal response of this filter can be found in Figure 5.4a and Figure 5.4b. Miniaturized Nb superconductor-based wide band filters have been reported in the literature [50], [51], using the HYPRES niobium process [54].

Sonnet software is used for all EM simulations. The capacitors are realized between the M3 and M2 layers, with a 250 nm SiO2 layer in between. The inductors are all realized on the M2 layer. The lumped-element filter circuit is first synthesized, after which each element is independently designed in Sonnet. Even though the individual elements are designed accurately, the parasitic coupling between elements and the bridges/vias used to connect the elements necessitates tuning (optimizing) the filter response to match the ideal response. The tuning is done in Sonnet, using the group delay tuning technique presented in [50], [52].

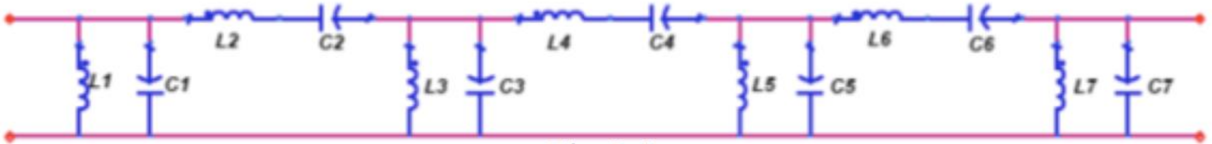

Fig 5.4a

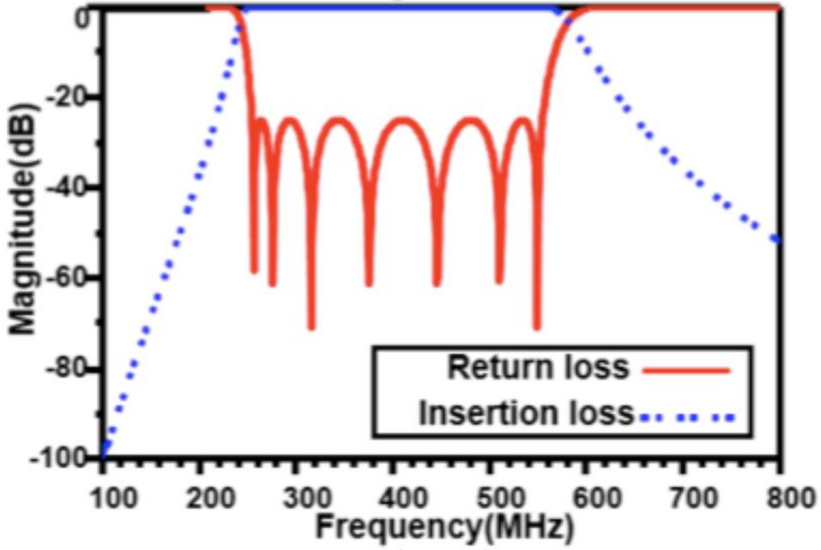

Fig 5.4b

Figure 5.4. a) Circuit model of 7-pole filter, b) circuit model response of the filter.

From the ideal circuit model, the group delay of the first resonator with all other resonators detuned (removed from the circuit) can be found. The dimensions of the first lumped LC elements are then refined to match the ideal group delay response calculated from the circuit model. The process continues with the 2nd, 3rd and 4th resonators. For the 7-pole Chebyshev filter, only the group delay of the first four resonators needs to be matched to the ideal circuit model. The last three resonators are added to the structure exactly the same as the first three resonators, for reasons of symmetry. Very fine-tuning of resonators 4 and 5 is then needed to improve the response of the filter. The tuning process of the first four resonators along with their group delays can be found in Figures 5.5 and 5.6.

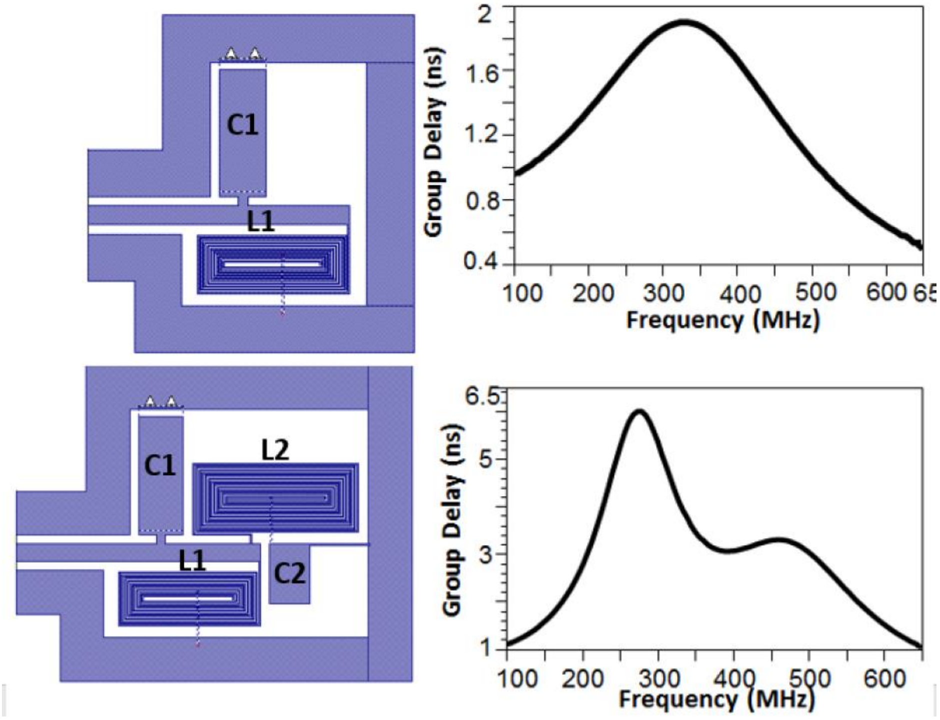

Figure 5.5. First resonator and first two resonators and their optimized group delay responses.

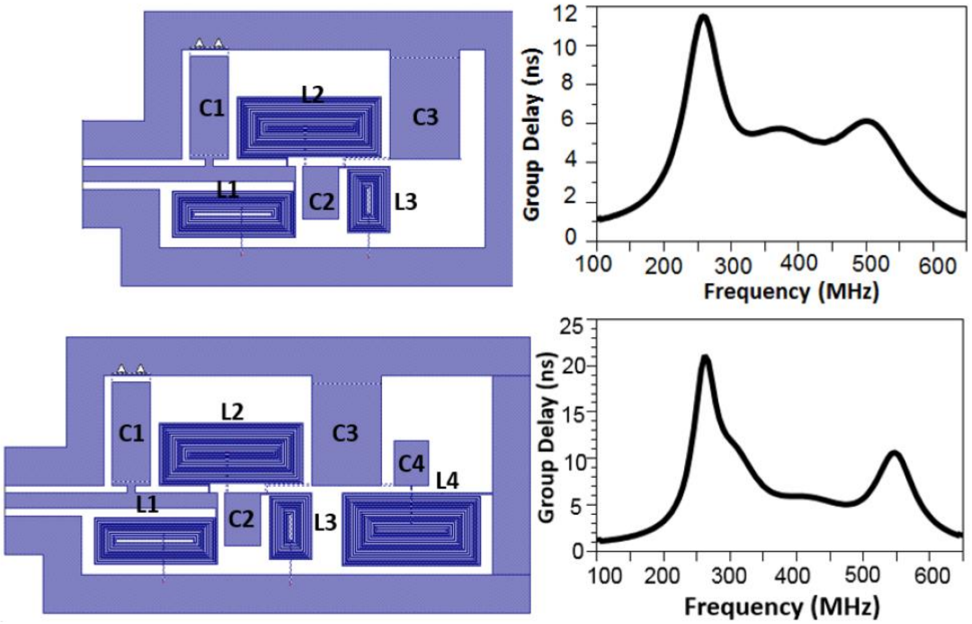

Figure 5.6. First three resonators and first four resonators and their optimized group delay responses.

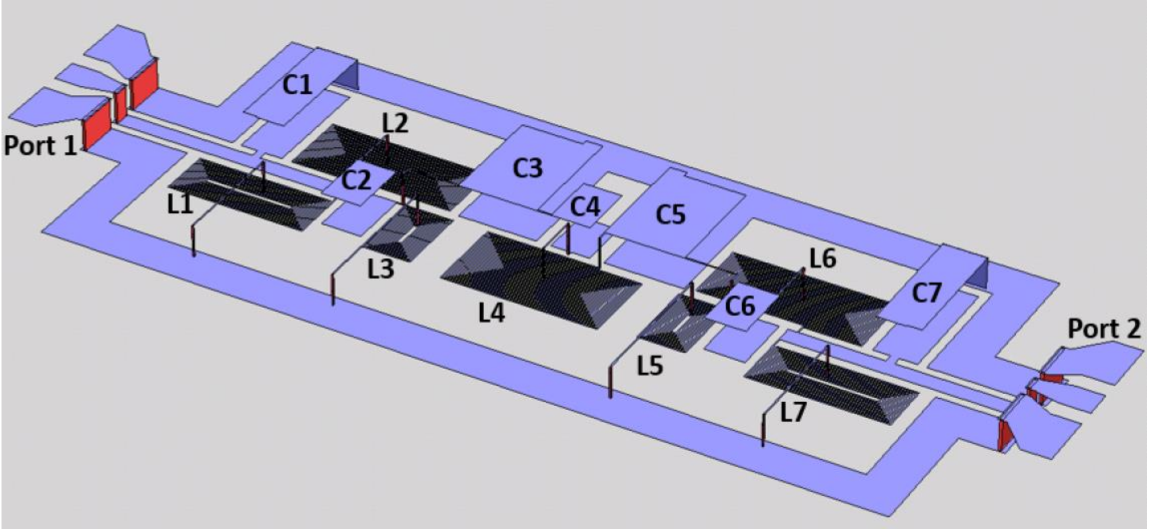

Figure 5.7. Complete 7-pole filter layout in Sonnet. The filter size is 3.2 mm × 1.1 mm.

The 3D layout of the final filter is given in Figure 5.7. The total size of the final filter is 3.2 mm by 1.1 mm. The sonnet EM simulation results of the filter are given in Figure 5.8. Note that in order to be able to measure the filter (using on-probe measurements), CPW lines with proper gaps were added to the ports. The simulation results of the filter at room temperature can be found in Figure 5.9.

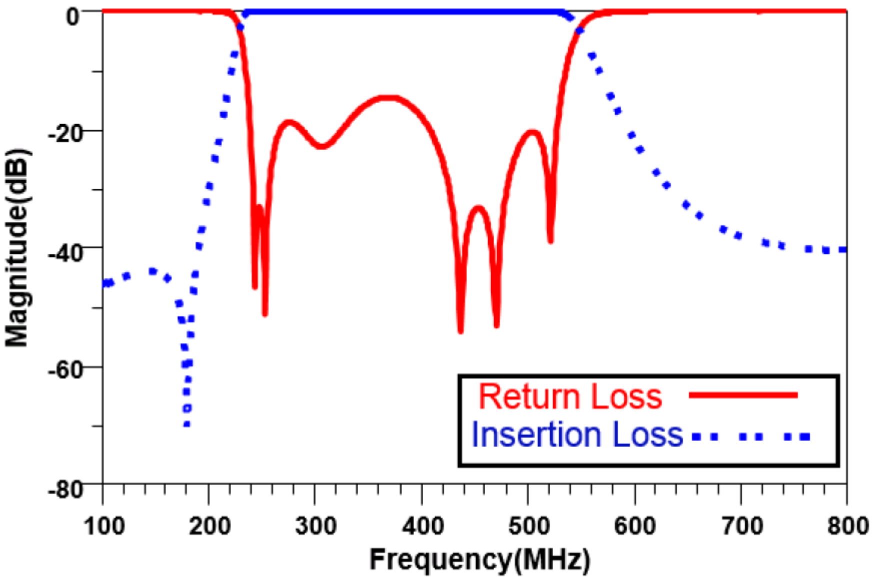

Figure 5.8. EM simulation results of the filter at cryogenic temperature.

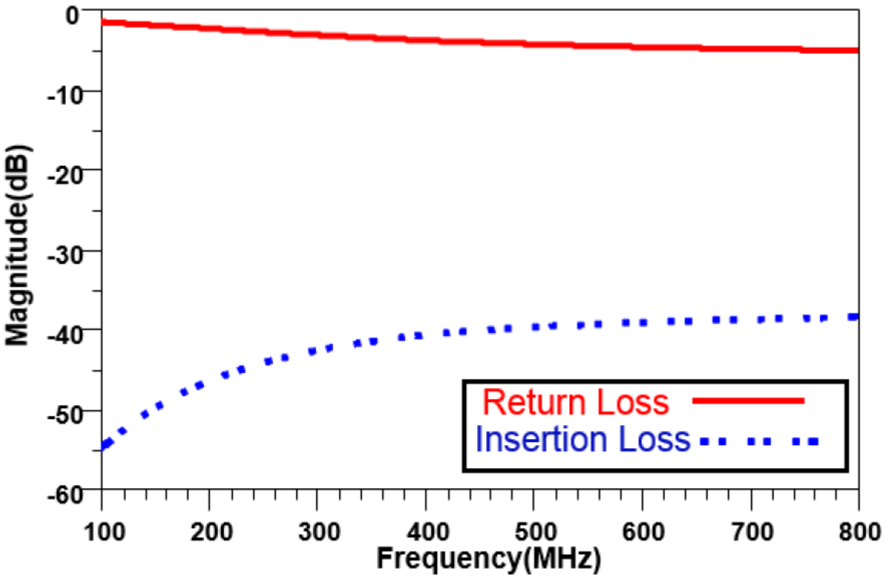

Figure 5.9. EM simulation results of the filter at room temperature.

The fabricated chip is placed in the vacuum chamber of the Lakeshore cryogenic probe station [47] shown in Figure 5.10 and cooled to bring the temperature down to 3 K on the chuck inside the vacuum chamber.

The measurement results of the filter at low power (-5 dBm) and high power (+9 dBm) are given in Figures 5.11 and 5.12. It is clear that more than 35 dB of isolation is achieved.

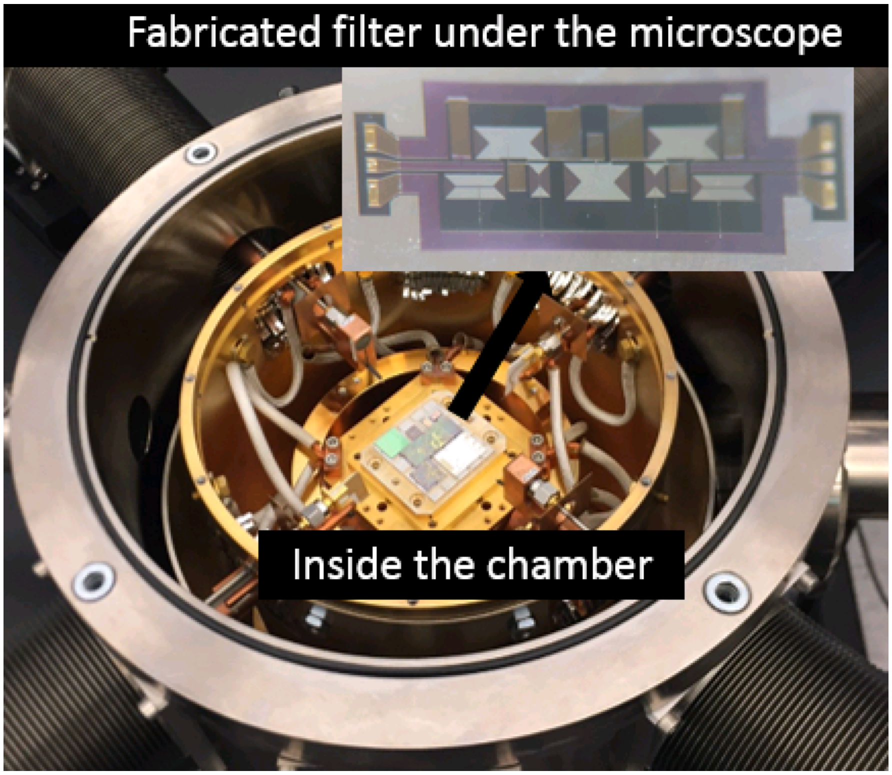

Figure 5.10. All chips inside the chamber and the fabricated filter under the microscope.

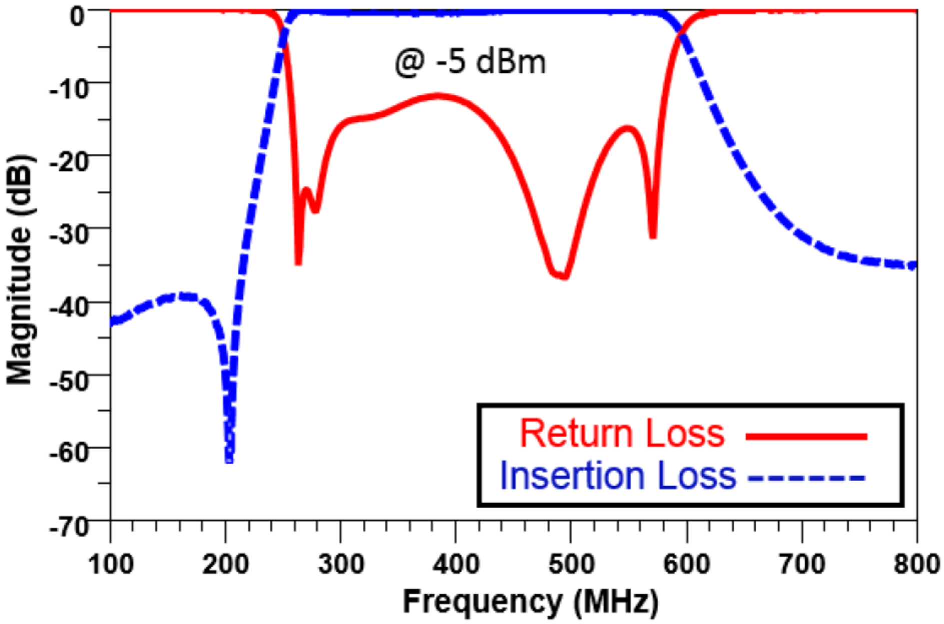

Figure 5.11. Measurement results of filter after cool-down at low power.

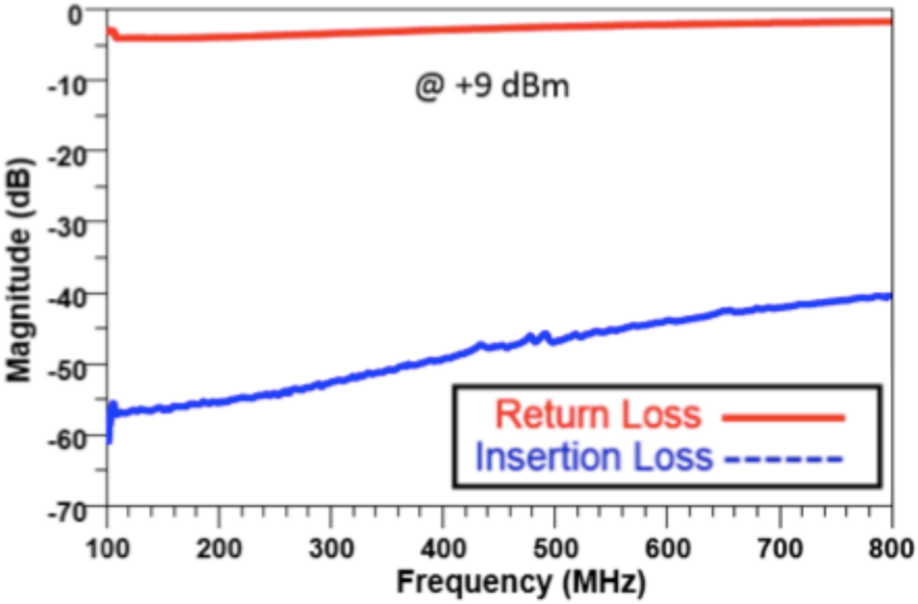

Figure 5.12. Measurement results of filter after cool-down at high power.

The 7-pole filter was modeled using the coupling matrix model [52], which takes the quality factor (Q) of the resonators into consideration. For band pass, the effects of a non-infinite resonator quality factor (Q_u) are included by offsetting s by a positive real factor $\delta(ie\ s \rightarrow \delta + s)$, where $\delta = f_0/(BW \times Q_u)$, f_0 is the center frequency of the passband, and BW is the designed bandwidth.

The formulations used to calculate the filter S-parameters including Q_u are given in Equations 5.3 to 5.6. M is the general $N \times N$ coupling matrix, which includes mainline couplings, cross-couplings and self-couplings, as shown in Eq. 5.1. R is the $N \times N$ termination impedance matrix, which contains the values of source and load impedances, as shown in Equation 5.2. Note that N is the number of poles used in the filter.

$$M = \begin{bmatrix} M_{11} & M_{12} & M_{13} & \cdots & M_{1,N-1} & M_{1,N} \\ M_{21} & M_{22} & M_{23} & \cdots & \cdots & M_{2,N} \\ \cdots & \cdots & M_{33} & \cdots & \cdots & \cdots \\ \cdots & \cdots & \cdots & \cdots & \cdots & M_{N-2,N} \\ \cdots & \cdots & \cdots & \cdots & M_{N-1,N-1} & M_{N-1,N} \\ \cdots & \cdots & \cdots & \cdots & M_{N-1,N} & M_{N,N} \end{bmatrix} \qquad (5.1)$$

$$R = \begin{bmatrix} R_S & 0 & \cdots & 0 \\ 0 & 0 & 0 & 0 \\ \vdots & 0 & \ddots & \vdots \\ 0 & 0 & \cdots & R_L \end{bmatrix} \qquad (5.2)$$

$$S_{21} = -2j\sqrt{R_S R_L}[A^{-1}]_{n1} \qquad (5.3)$$

$$S_{11} = 1 + 2jR_s[A^{-1}]_{11} \qquad (5.4)$$

$$A = \lambda I - jR + M \qquad (5.5)$$

$$\lambda = \frac{f_0}{BW}\left(\frac{f}{f_0} - \frac{f_0}{f}\right) \qquad (5.6)$$

The simulation results of the 7-pole filter, using Q factor values of 1000, 50, 10 and 5, are shown in Figure 5.13. It is observed that even using resonators with a Q value of 5 gives a good return loss. However, this contradicts with the measured results shown in Figures 5.9 and 5.12. These findings led us to believe that the reason why the filter acts as a reflector is thus not attributed to the lower Q value of the resonator obtained when the niobium is in the normal state.

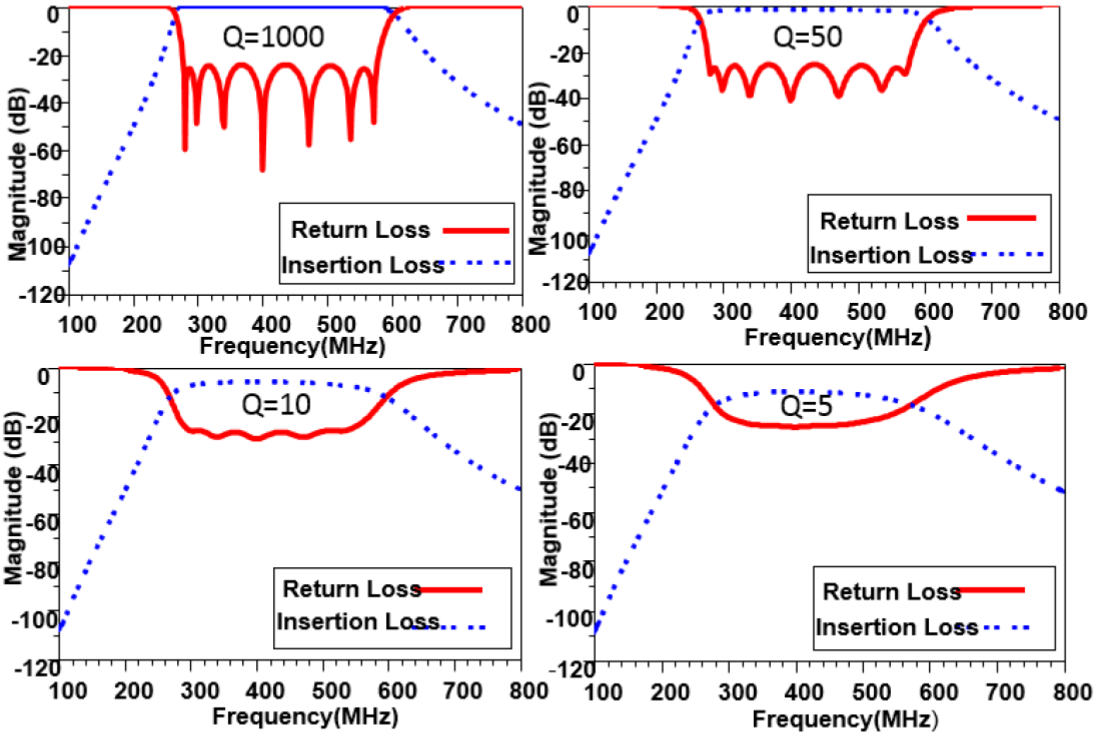

Figure 5.13. Filter results using different Q values.

After further investigation, it was found that the reason for the filter’s behavior at high power levels (i.e., the niobium in the normal state) is that the inductors used in building the filter act as inductors at low power levels (i.e., LTS niobium in the superconducting state) while they act as capacitors at high power levels (i.e., LTS niobium in the normal state).

In order to confirm this phenomenon, the first resonator was isolated from the filter circuit using a cut carried out by laser, as shown in Figure 5.14, and was evaluated as a single resonator circuit.

Figure 5.15 shows both the simulation and measured results of the first resonator while at cryogenic temperature at a low power level (-5 dBm). The results on the Smith chart clearly show the resonance transitioning from an inductive to a capacitive state.

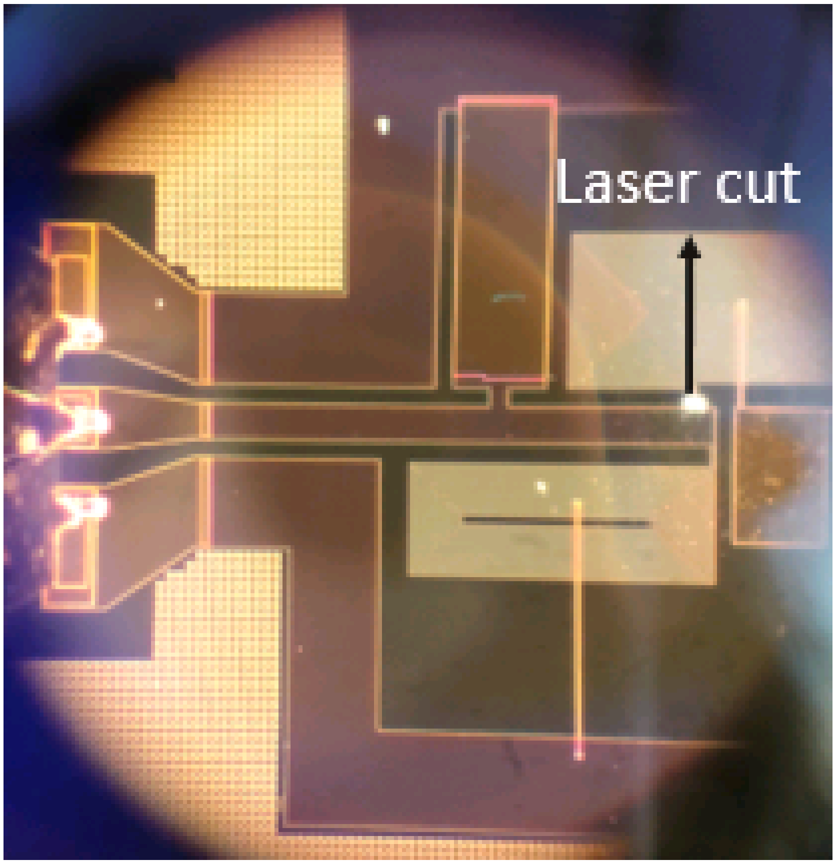

Figure 5.14. Laser cut used to isolate the first resonator.

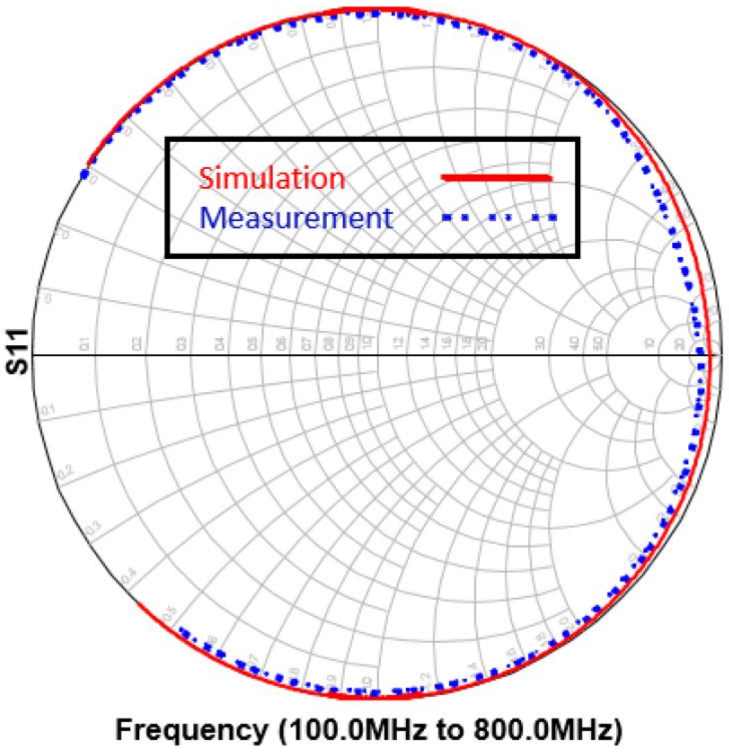

Figure 5.15. First resonator simulation and measurement results at cryogenic temperature (while at cryogenic and under low power -5 dBm).

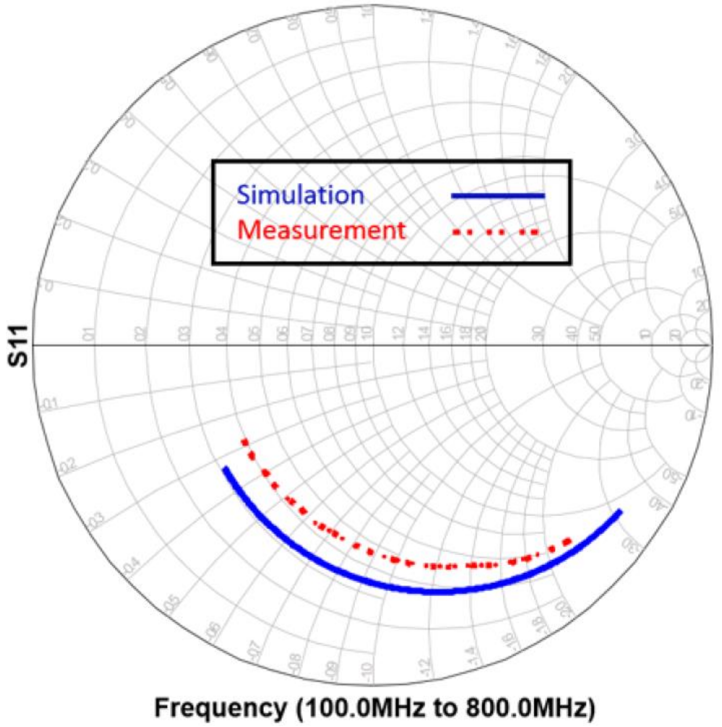

Figure 5.16. First resonator simulation and measurement results (while at cryogenic and in high power +9 dBm).

The same simulations, assuming normal niobium metal and measurements, were done at high power levels. The results obtained in this case are shown in Figure 5.16. It can be seen that the resonator acts as a capacitor. To further investigate the phenomenon, a single inductor was simulated assuming room temperature niobium and lossless niobium. The 3D model of one of the single inductors used in the filter that is used for simulations can be found in Figure 5.17. The simulation results of the input impedance seen for the inductor for the lossy and lossless cases are shown in Figures 5.18 and 5.19, respectively. The imaginary value of the inductor input impedance is positive for the lossless case, indicating that it acts as inductor, while it is negative at room temperature, meaning it acts as a capacitor. Through the extraction of the complete equivalent circuit of the inductor, it can be shown that having a very high series resistance can yield the same response.

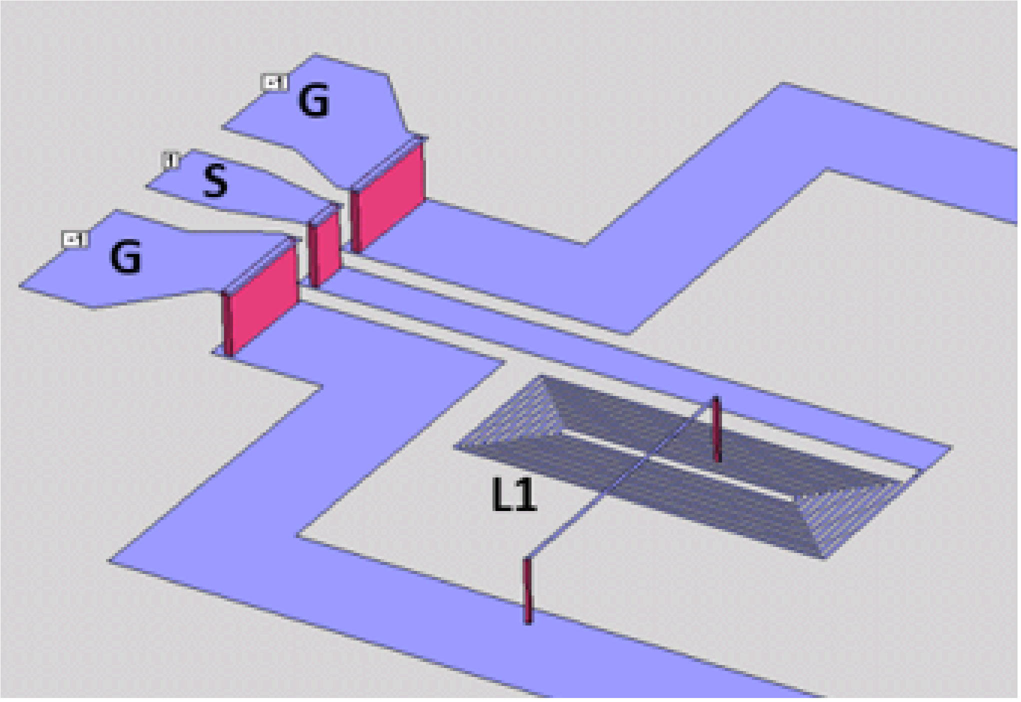

Figure 5.17. Single inductor used for simulations.

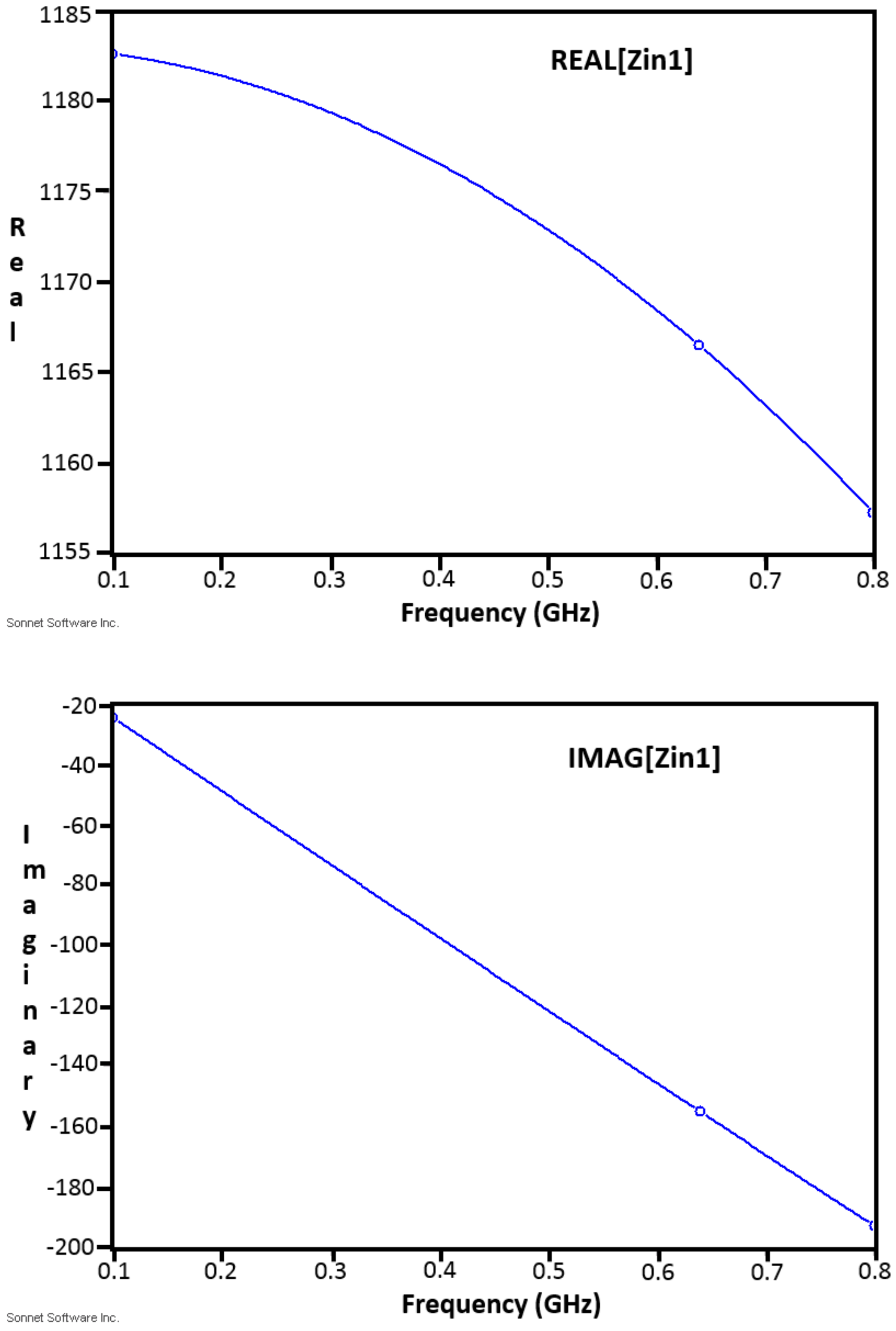

Figure 5.18. Simulation results of single inductor at room temperature.

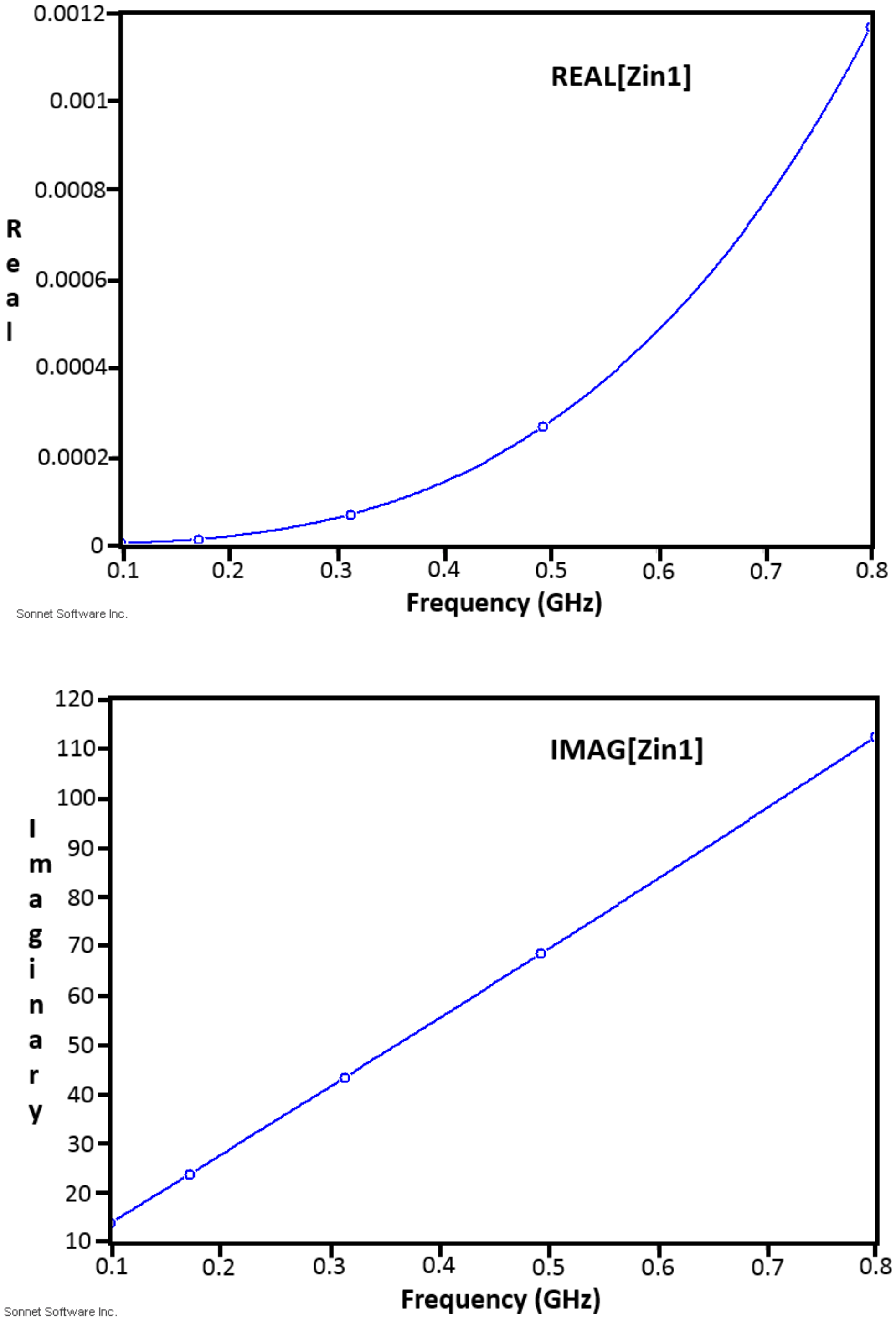

Figure 5.19. Simulation results of single inductor at cryogenic temperature.

Looking at the equivalent circuit of the inductor shown in Figure 5.20, it can be readily shown mathematically that the impedance seen between the two terminals can vary with the resistance value R. Assuming a small value for the parasitic capacitance C, and a small value for the resistance R, the imaginary part of the impedance seen is inductive. However, with the same small value of the capacitance C, increasing the resistance R can lead to impedance which its imaginary part is capacitive. This explains why the niobium inductor is seen as a capacitor when operating at high power levels

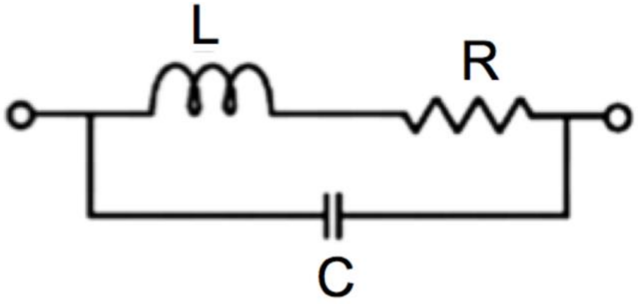

Figure 5.20. Equivalent circuit model of a spiral inductor.

5.4 Application examples

The Nb-based lumped-element filter can be used in a variety of applications. One of the proposed applications is a high-power protection circuit for superconductor digital RF receivers. Because such receivers require the use of a front-end RF filter anyway, the lumped-element filter, which can be integrated monolithically with the receiver, can serve two purposes: as a front-end filter to protect the digital receiver from out-of-band interfering signals, and as a protection circuit to protect the receiver from in-band high levels of input power levels to prevent damaging the LTS analogue-to-digital converter (ADC).

Figure 5.21 shows a schematic block diagram of the digital receiver. The front-end Nb filter is replaced with two filters and two 90° hybrids. The circuit allows low-power RF signals to pass to the ADC, while reflecting the signal to a load as the RF power exceeds a certain power level. The LTS lumped-element filter is ideal for this application because, as is shown in Figure 5.9 for an input power of +9 dBm, the filter switches to the normal state, reflecting most of the power over a 40 dB isolation to the superconductor ADC. Due to the high Q of the superconductor resonators, there is a build-up of high levels of RF currents in the resonator elements, which in turn allows the use of reasonable line widths for the lumped-element components within the fabrication process limitation while still permitting the filter to switch to the normal state at more moderate dBm power levels.

It should be noted that the first hybrid of the protection circuit and load is placed outside the cryogenic package at room temperature. The two filters and second hybrid can be implemented with lumped-element superconductor niobium technology and integrated monolithically with the ADC on a single chip. Note also that the second hybrid does not need to be studied for high-power handling capability, since it is already protected by the filters.

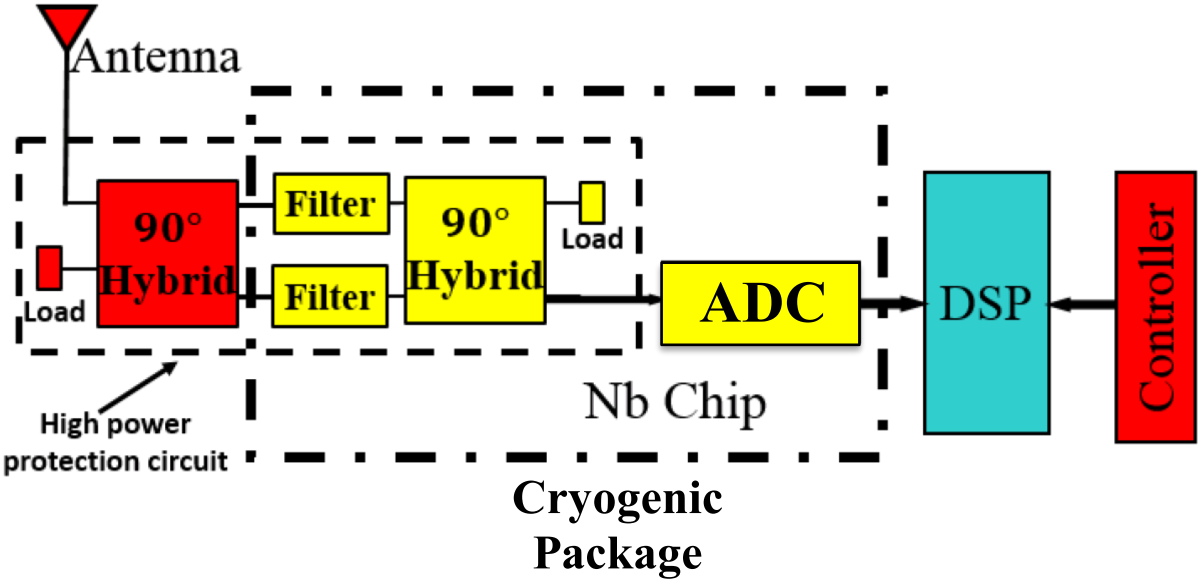

Figure 5.21. Superconductor-based receiver front-end and the proposed circuit for high power protection.

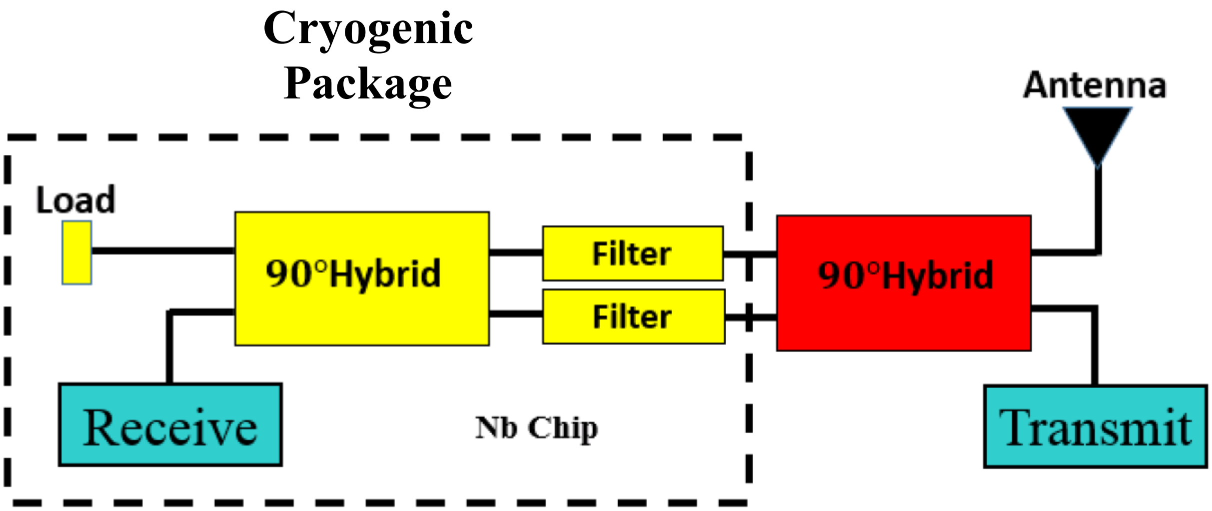

Figure 5.22. T/R circuit block diagram.

The second proposed application is in transmit/receive (T/R) switch applications that provides isolation between transmit and receive circuits. The block diagram of the proposed circuit is given in Figure 5.22. In case of low power while at cryogenic temperature, the filters act as band pass filters and the signal goes from antenna to receiver, exhibiting a very low insertion loss. However, in the case of transmit mode, the filters will effectively act as reflectors, causing the signal to be directed from the transmitter to the antenna. Once again, the hybrid at the transmit side does not need to be Nb-based; rather, it can be integrated with antenna and transmitter outside the cryogenic package.

In order to confirm the circuit's performance, lumped-element filters and hybrids are designed using the MIT-LL niobium multilayer process. The design of these elements is similar to designs employed in [53] using the HYPRES multilayer niobium process [54]. The lumped-element hybrid circuit model can be found in Figure 5. 23a, along with its layout at Figure 5. 23b. The simulation results of the hybrid are presented in Figure 5. 24. Note that all the dimensions in the figures are in µm.

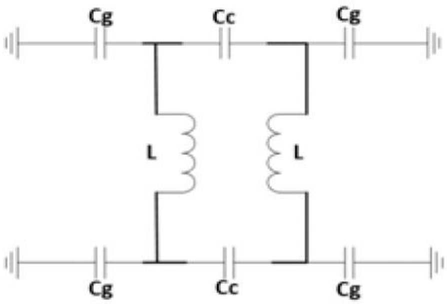

Fig 5.23a

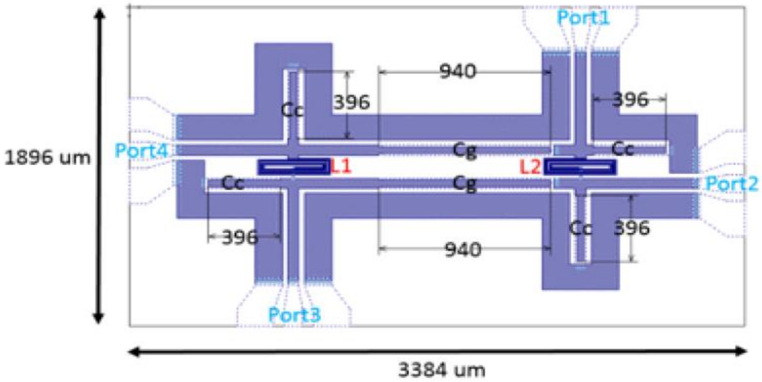

Fig 5.23b

Figure 5.23. a) Circuit model of hybrid design, b) Layout of the hybrid.

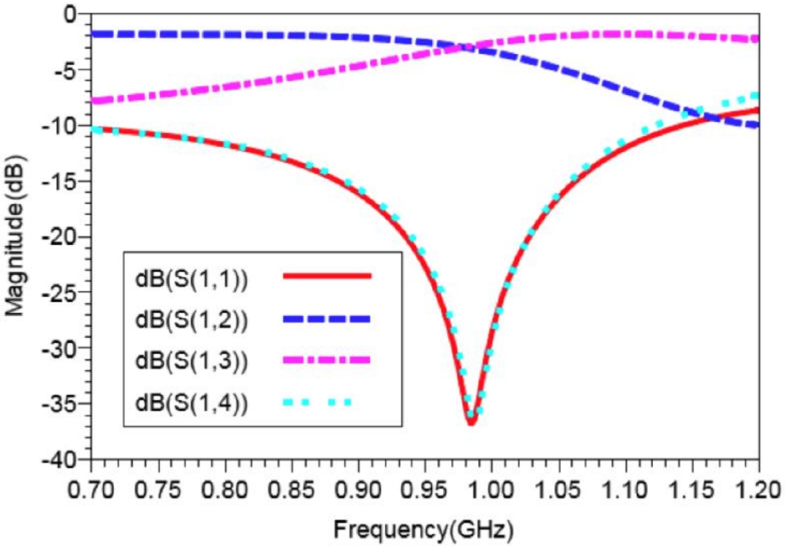

Figure 5.24. Simulation results of hybrid in Sonnet.

The center frequency of the hybrid is 0.985 GHz with a 10% bandwidth. As mentioned above, the layout of the designed hybrid is presented in Figure 5. 22b, where L1 is equal to L2 and 5.62nH, Cg is 3.18nH, and Cc is 1.31pF. In this type of design, large capacitances can be built using thin dielectric layers, which helps miniaturize the structures.

A 3-pole band pass filter was designed at 0.987 GHz with a 100 MHz bandwidth and using lumped elements. The circuit model of the filter is presented in Figure 5. 24a and the layout of the filter is shown in Figure 5. 24b. The 3-pole filter is fabricated and tested at cryogenic temperature while at low power (-5 dBm) and also at high power (+10 dBm), with measurement results of the filter being obtained at low power (-5 dBm) and at high power (+10 dBm).

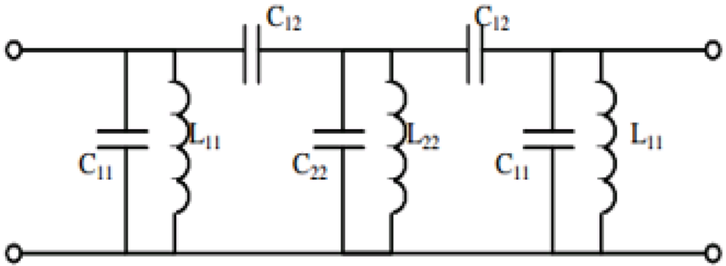

Fig 5.25a

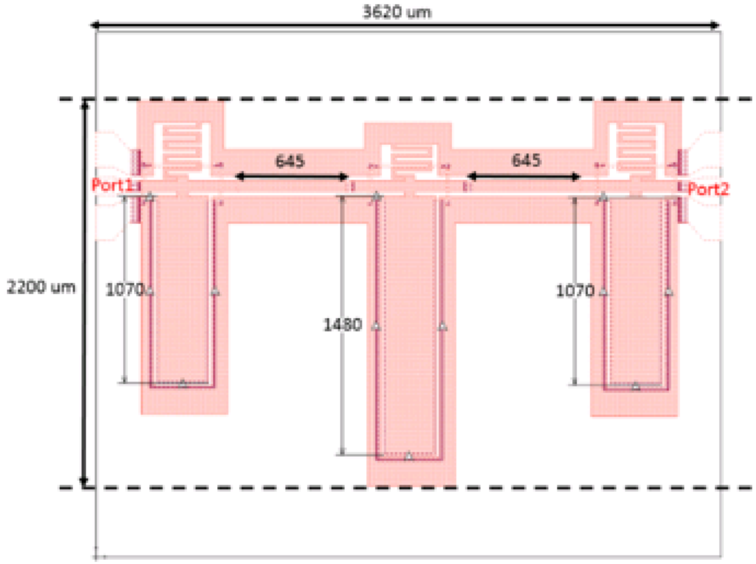

Fig 5.25b

Figure 5.25. a) Circuit model of 3-pole filter, b) Layout of the filter.

The circuit presented in Figure 5. 22 (T/R switch circuit) is modeled in ADS using EM simulation results of the hybrid and measurement results of the filter at cryogenic temperature, at both low and high power levels. The isolation between transmit and receive while the filters are at low power and high power is given in Figure 5. 27. It can be seen that, in the transmit mode, the circuit offers an isolation of more than 80 dB between the receiver and the transmitter.

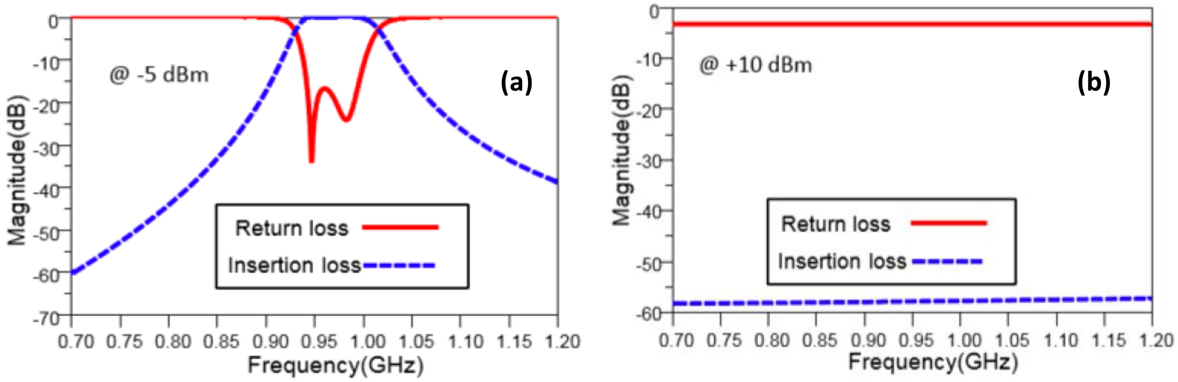

Figure 5.26. a) Measurement results of filter at low power; b) Measurement results of filter at high power.

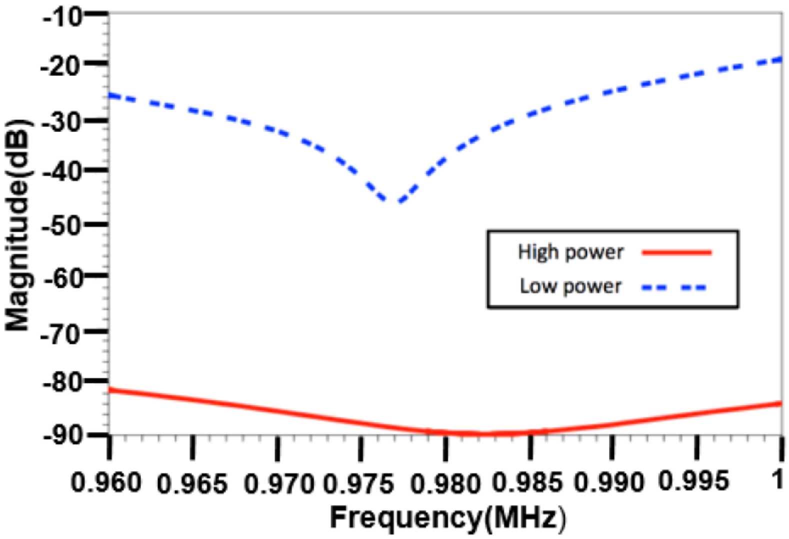

Figure 5.27. Isolation between transmit and receive at low power and high power.

6. Conclusion and Future work

6.1 Conclusion

A novel frequency-dependent power limiter (FDPL) has been presented employing RF MEMS switches and bandpass filters. The FDPL circuit can easily be extended to multiple branches for use in different frequency bands. Moreover, the frequency bands can be made tunable, allowing for the realization of a highly dynamic power limiter that is capable of changing both the limiting power level and the frequency band. Such limiters are suitable for applications where the power limiter needs to adapt to changes in interfering signal levels and frequency during operation. To the best of our knowledge, this is the first time an adaptive FDPL has been reported in the literature.

The limiting speed depends on the speed of the MEMS switch, which is typically in the microseconds range when the switch is actuated only by dc bias voltage. In the proposed concept, dc bias is used to bring the switch close to actuation and carry on the actuation by RF power. Thus, the gap between the electrodes prior to RF actuation is smaller than the gap with which the switch is built, so faster speeds are expected.

As with most design concepts, there are some challenges with this FDPL. First, the operating bandwidth of the limiter is determined by the bandwidth of the front element of the limiter circuit (hybrid, circulators), which is only around 10%. Multi-section hybrid designs need to be used to enlarge the operating bandwidth. Furthermore, the tunable filters must be designed to maintain bandwidth not only over the tuning range, but also when operating under high power, since some of the tuning elements, such as the semiconductor varactors, may change their performance when operating under high RF voltage levels inside the resonators.

A multiphysics analysis is presented to characterize the performance of thermally-actuated MEMS switches operating under high RF power levels for use in power limiter applications. A COMSOL FEM simulator was used to model the switch under both thermal and electrostatic actuations. The results are then compared with measurements for a thermally actuated MEMS switch, fabricated to verify the methodology used. In power limiter applications, the switch is assumed to be actuated with the aid of dc voltage applied to the thermal actuator and RF input power. This thesis shows how HFSS can be combined with both thermal and electrostatic analyses to yield a relationship between the self-actuation RF power and the actuation dc voltage applied to the thermal actuator. A close-to-linear relationship is found for the thermally-actuated switch, which helps to improve the design sensitivity when using these types of switches in power limiter applications.

Finally in this work, a novel use for low temperature superconductor Nb-based band pass lumped element filters was presented. In addition to serving as a front-end filter for protecting the receiver from out-of-band signals, it can act as a protection circuit for protecting the receiver from in-band high power levels. The filter also promises to be useful in T/R switch applications to provide isolation between the receive circuits and transmit circuits. It was found that the superconductor lumped element inductor employed in this filter switched from “inductor” when operating at a low power level to “capacitor” when operating at high power levels. This phenomenon was verified both theoretically and experimentally. To our knowledge, this is the first time such an interesting switching characteristic has been reported in the literature.

6.2 Future work

The idea of a circuit based tunable frequency dependent power limiter has been presented in this thesis using conventional MEMS switches and it’s shown that other types of switches such as thermally actuated switches are more suitable for the power limiter application since they provide a linear $\mathrm{V_{dc}} - \mathrm{P_{RF}}$ performance and result in more controllability. As a future work it is possible to use other type of switches such as mechanical relays or costume built mechanical cantilever switches in order to be able to use the limiter in different power levels. Another important issue to point out is that Metal MUMPS process which was used to fabricate the presented thermally actuated switch is no longer available so finding a process to replace Metal MUMPS is another desired future research. Using this method, new switches with different dimensions can be fabricated which can be used to limit different power levels.

In order to have a sharper selectivity in FDPL circuit, the bandpass Chebyshev filters used can be replaced with pre-distorted filters. The edges of the insertion loss in a pre-distorted filter will become sharp at the price of decreasing the return loss. In the FDPL application, having a decreased return loss is in fact needed to minimize the zigzag in the threshold power level. Moreover, having a highly lossy filter is not an issue for the operation of the FDPL, since we want the RF signal to be dissipated, anyway, either in the filter or in the load when the switch is in the ‘on’ state.

Moreover, since the novel low temperature superconductor-based limiter works based on the fact that the inductors used in the lumped element filter act as capacitors at high power temperature and as inductors at low power. The width of the inductor can indicate the power level in which the limiting happens. As a future work it is possible to fabricate inductors with different widths and test them in different power levels.

Another focus for the future work could be finding other types of power limiter applications and new methods of implementing the concept.

Bibliography

[1] D. Gupta, D. E. Kirichenko, V. V. Dotsenko, R. Miller, S. Sarwana, A. Talalaevskii, J. Delmas, R. J. Webber, S. Govorkov, A. F. Kirichenko, I. V. Vernik, and J. Tang, “Modular Multi-function Digital-RF Receiver Systems,” IEEE Trans. Appl. Supercond., vol. 21, No. 3, pp. 883-890, Jun. 2011.

[2] Sara Sharifian Attar, “Low Temperature Superconducting RF MEMS Devices, “PhD. thesis”, ECE. Dept., UW, Feb. 2014.

[3] A. Kirichenko, D. Gupta, and S. Sarwana, “RSFQ Asynchronous Switch Matrix,” IEEE Trans. Appl. Supercond., vol. 17, No. 2, pp. 505-508, Jun. 2007.

[4] D. J. Seymour, D. D. Heston and R. E. Lehmann, "X-band and ka-band monolithic GaAs PIN diode variable attenuation limiters," in *Microwave and Millimeter-Wave Monolithic Circuits Symposium, 1988. Digest of Papers., IEEE 1988,* 1988, pp. 147-150.

[5] D. G. Smith, D. D. Heston and D. L. Allen, "Designing high-power limiter circuits with GaAs PIN diodes," in *Microwave Symposium Digest, 1999 IEEE MTT-S International,* 1999, pp. 329-332 vol.1.

[6] Bera, S. C., Basak, K., Jain, V.K., Singh, R. V. and Garg, V. K. (2010), Schottky diode-based microwave limiter with adjustable threshold power level. Microw. Opt. Technol. Lett. 2010, vol. 52, pp.1671–1673.

[7] G. M. Rebeiz, RF MEMS: Theory, design and technology, Wiley, 2003.

[8] E. Gatard, R. Sommet, P. Bouysse, R. Quere, M. Stanislawiak and J. M. Bureau, "High power S band limiter simulation with a physics-based accurate nonlinear PIN diode model," *2007 European Microwave Integrated Circuit Conference,* Munich, 2007, pp. 72-75.

[9] J. D. Adam and S. N. Stitzer, "Frequency selective limiters for high dynamic range microwave receivers," in *Microwave Symposium Digest, 1993., IEEE MTT-S International,* 1993, pp. 477-478 vol.1.

[10] N. O. Fenzi, K. F. Raihn, G. V. Negrete, E. R. Soares and G. L. Matthaei, "An optically switched bank of HTS bandstop filters," in *Microwave Symposium Digest, 1994., IEEE MTT-S International,* 1994, pp. 195-198 vol.1.

[11] J. C. Booth, K. Leong and S. A. Schima, "A superconducting microwave power limiter for high-performance receiver protection," *2004 IEEE MTT-S International Microwave Symposium Digest (IEEE Cat. No.04CH37535)*, 2004, pp. 139-142, vol.1.

[12] J. C. Booth, D. A. Rudman, and R. H. Ono, “A self-attenuating superconducting transmission line for use as a microwave power limiter,” IEEE Trans. Applied Supercond., vol. 13, no. 2, pp. 305-310, June 2003.

[13] P. Phudpong and I. C. Hunter, "Non linear bandstop filters A new method of frequency selective limiting," in *Microwave Conference, 2006. 36th European,* 2006, pp. 204-207.

[14] J. D. Adam and S. N. Stitzer, "Frequency selective limiters for high dynamic range microwave receivers," in *Microwave Symposium Digest, 1993., IEEE MTT-S International,* 1993, pp. 477-478 vol.1.

[15] J. D. Adam, S. N. Stitzer and R. M. Young, "UHF frequency selective limiters," in *Microwave Symposium Digest, 2001 IEEE MTT-S International,* 2001, pp. 1173-1174 vol.2.

[16] S. D. Patel, L. Dubrowsky, S. E. Saddow, R. Kaul and R. V. Garver, "Microstrip plasma limiter," in *Microwave Symposium Digest, 1989., IEEE MTT-S International,* 1989, pp. 879-882 vol.3.

[17] P. Phudpong and I. C. Hunter, "Nonlinear Matched Reflection Mode Bandstop Filters for Frequency Selective Limiting Applications," *2007 IEEE/MTT-S International Microwave Symposium*, Honolulu, HI, 2007, pp. 1043-1046.

[18] P. Phudpong and I. C. Hunter, "Non linear bandstop filters A new method of frequency selective limiting," in *Microwave Conference, 2006. 36th European,* 2006, pp. 204-207.

[19] J A. C. Guyette, I. C. Hunter, R. D. Pollard and D. R. Jachowski, "Perfectly-matched bandstop filters using lossy resonators," in *Microwave Symposium Digest, 2005 IEEE MTT-S International,* 2005, pp. 4 pp.

[20] J J. Givernaud, A. Crunteanu, A. Pothier, C. Champeaux, A. Catherinot and P. Blondy, "CPW self-resetting power limiting devices based on microwave power induced semiconductor-metal transition in vanadium dioxide," in *Microwave Symposium Digest, 2009. MTT '09. IEEE MTT-S International,* 2009, pp. 109-112.

[21] S. Scott, C. D. Nordquist, M. J. Cich, T. S. Jordan and C. T. Rodenbeck, "A frequency selective surface with integrated limiter for receiver protection," in *Antennas and Propagation Society International Symposium (APSURSI), 2012 IEEE,* 2012, pp. 1-2.

[22] R. A. Bossard, Xiaotao Liang, Ling Li, Seokho Yun, D. H. Werner, B. Weiner, T. S. Mayer, P. F. Cristman, A. Diaz and I. C. Khoo, "Tunable Frequency Selective Surfaces and Negative-Zero-Positive Index Metamaterials Based on Liquid Crystals," *Antennas and Propagation, IEEE Transactions on,* vol. 56, pp. 1308-1320, 2008.

[23] R. Jonsson, C. Samuelsson, S. Reyaz, R. Malmqvist, D. Smith, M. Richard, P. Rantakari, T. Vähä-Heikkilä and R. Baggen, "An experimental study of standard packaged/unpackaged GaAs

MMIC based RF-MEMS limiter test circuits," in *Semiconductor Conference (CAS), 2011 International*, 2011, pp. 203-206.

[24] X. Rottenberg, K. Vaesen, S. Brebels, B. Nauwelaers, R. P. Mertens, W. De Raedt and H. A. C. Tilmans, "MEMS capacitive series switches: Optimal test vehicles for the RF self-biasing phenomenon," in *Micro Electro Mechanical Systems, 2005. MEMS 2005. 18th IEEE International Conference on*, 2005, pp. 147-150.

[25] J J. Gauvin, O. Vendier, J. -. Cazaux and P. Blondy, "Microwave power limiters based on RF-MEMS," in *Micro Electro Mechanical Systems (MEMS), 2013 IEEE 26th International Conference on*, 2013, pp. 769-772.

[26] X. Rottenberg, S. Brebels, B. Nauwelaers, R. P. Mertens, W. De Raedt and H. A. C. Tilmans, "Modelling of the RF self-actuation of electrostatic RF-MEMS devices," in *Micro Electro Mechanical Systems, 2004. 17th IEEE International Conference on. (MEMS),* 2004, pp. 245-248.

[27] D. Mercier, P. Blondy, D. Cros and P. Guillon, "An electromechanical model for MEMS switches," *2001 IEEE MTT-S International Microwave Sympsoium Digest (Cat. No.01CH37157)*, Phoenix, AZ, USA, 2001, pp. 2123-2126 vol.3.

[28] Available online at: www.components.omron.com

[29] Available online at: www.radantmems.com

[30] M. Daneshmand, W. D. Yan and R. R. Mansour, "Thermally Actuated Multiport RF MEMS Switches and Their Performance in a Vacuumed Environment," *Microwave Theory and Techniques, IEEE Transactions on,* vol. 55, pp. 1229-1236, 2007.

[31] http://www.jqlelectronics.com

[32] https://www.macom.com/products/diodes/varactor-tuning-diodes

[33] R. R. Mansour, F. Huang, S. Fouladi, W. D. Yan, and M. Nasr “High-Q tunable filters: challenges and potential”, *IEEE Microwave Magazine*, vol. 15, 00.70-82, July 2014.

[34] S. Fouladi, F. Huang, W. D. Yan and R. R. Mansour, "High-Q Narrowband Tunable Combline Bandpass Filters Using MEMS Capacitor Banks and Piezomotors," in *IEEE Transactions on Microwave Theory and Techniques*, vol. 61, no. 1, pp. 393-402, Jan. 2013.

[35] S. Vamegh, R. Dhaouadi and M. Bakri-Kassem, “Macromodeling of Thermally Driven V Shaped MEMS Actuators” Elsevier journal Mechatronics, vol. 46, pp.193–204, Oct. 2017.

[36] M. Bakri-Kassem, and R. Mansour “High Power Latching RF MEMS Switches” IEEE Transactions on Microwave Theory & Techniques, vol.63, no.1, pp. 222-232, Jan. 2015.

[37] M. Bakri-Kassem, R. R. Mansour and “A Novel Latching RF MEMS SPST Switch” IEEE Microwave Conference, 2012. 42th European, 28 Oct. -2 Nov. 2012, Amsterdam, Netherland.

[38] Available online at: robotice.eecs.berkeley.edu

[39] "COMSOL Multiphysics Reference Manual, version 5.3", COMSOL, Inc, www.comsol.com

[40] D. E. Kirichenko, T. V. Filippov, and D. Gupta, “Microwave receivers with direct digitization,” in Proc. IEEE MTT-S Int. Microw. Symp., Jun. 2009, pp. 1449–1452.

[41] O. Mukhanov, D. Gupta, A. Kadin, J. Rosa, V. Semenov, and T. Filippov, “Superconductor digital-RF transceiver components,” in Proc. of the SDR Technical Conference, San Diego, 2002, vol. I, pp. 227–232 [Online].

[42] Zou Xiongfei, Bu Shirong, Luo Zhengxiang, Ning Junsong and Zeng Cheng, "The power-dependent test of high temperature superconductor CPW transmission line," *IEEE 2011 10th International Conference on Electronic Measurement & Instruments*, Chengdu, 2011, pp. 188-191.

[43] E. Rocas, C. Collado, J. Mateu, N. Orloff and J. C. Booth, "Modeling of Self-Heating Mechanism in the Design of Superconducting Limiters," in *IEEE Transactions on Applied Superconductivity*, vol. 21, no. 3, pp. 547-550, June 2011.

[44] Available online at: http://www.skyworksinc.com/uploads/documents/200480C.pdf

[45] D. Wang, L. Gao, S. Zheng, F. Deng and D. Hou, "Investigation on the pulse characteristics of RF/microwave limiter based on multistage PIN diodes and Schottky diodes," *Proceedings of 2014 3rd Asia-Pacific Conference on Antennas and Propagation*, Harbin, 2014, pp. 1366-1369.

[46] Available online at: http://www.ll.mit.edu/

[47] Available online at: http://www.lakeshore.com/products/cryogenic- probe-stations/model-cpx-cryogenic-probe-station/Pages/Overview.aspx

[48] Available online at: http://www.sonnetsoftware.com/ M. Young, *The Techical Writers Handbook.* Mill Valley, CA: University Science, 1989.

[49] Yongle Wu, Meijun Qu and Yuanan Liu, “ A Generalized Lossy Transmission-Line Model for Tunable Graphene-Based Transmission Lines with Attenuation Phenomenon”, US National Library of Medicine National institutes if Health, Published online on August 2016.

[50] S.Setoodeh,"Superconducting Microwave Filters,"M.S.thesis,ECE. Dept., UW, Feb. 2011.

[51] P. D. Laforge, R. R. Mansour and M. Yu, "Diplexer Design Implementing Highly

Miniaturized Multilayer Superconducting Hybrids and Filters," in IEEE Transactions on Applied Superconductivity, vol. 19, no. 2, pp. 47-54, April 2009.ircuit devices (Patent style)," U.S. Patent 3 624 12, July 16, 1990.

[52] Richard J.Cameron, Raafat Mansour, Chandra M.Kudsia: Microwave Filters For Communication Systems: Fundamentals, Design and Applica-tions, Wiley, 2007.

[53] P. D. Laforge, "Tunable Superconducting Microwave Filters," P.h.D thesis, ECE. Dept., UW, 2010.

[54] Availabe online at: www.HYPRES.com.